5. FEM MICRO-MACRO MODELS WITHOUT YIELD LOCUS

5.1. Introduction

The FEM is currently used to simulate the behavior of the materials at the microscopic level. In such cases, a crystal is discretized by one finite element or more as presented in section 5.2. Such simulations aim to validate the microscopic models or to perform parametric studies, that are difficult to do experimentally.

Another use of the FEM coupled with microscopic models concerns accurate macroscopic simulations, where the anisotropic material behavior is taken into account at a microscopic level. In such micro-macro approaches, a lot of averaging methods to extract the macroscopic behavior from microscopic analysis are possible. Some examples are listed in sections 5.3. to 5.5. These examples concern approaches where no macroscopic yield locus is computed. Chapter 6 is dedicated to the macroscopic approximation of yield loci.

5.2. Microscopic FEM computations to model macroscopic behavior

Finite element simulations allow to treat a crystalline aggregate as a continuum, by simply requiring the equilibrium of the stress tensors and the continuity of the displacements across the grain boundaries. Hereafter, two examples (Acharya & Beaudoin 1999, Teodosiu *et al.* 1992) among others (Beaudoin *et al.* 1995, Anand & Kothari 1996, Bertram *et al.* 1997...) are summarized, the first one with specific modeling of grain boundaries and the second one without. These examples demonstrate the interest of such approaches to validate single crystal plasticity models and to investigate microscopic effects by means of a numerical sensitivity analysis. For instance, grain size effect on a macroscopic flow stress is numerically studied in Acharya & Beaudoin 1999.

5.2.1. Teodosiu *et al.* 1992

The 3D finite element mesh used to describe a tensile test on a polycrystalline specimen of pure copper is shown on Figure 5-1.

The applied constitutive law takes the elastic anisotropy into account and considers the plastic flow rule at the slip system level thanks to a rate-dependent equation such as (4-15). The hardening law of the CRSS is represented by a relation similar to (4-16), presented in section 4.3. Teodosiu uses neither an average polycrystal common

reference CRSS $\bar{\tau}_c$ nor a single crystal common reference CRSS τ_c but a CRSS defined for each slip system τ_c^s. This CRSS τ_c^s is related to the dislocation density on each slip system, which induces the internal variables choice.

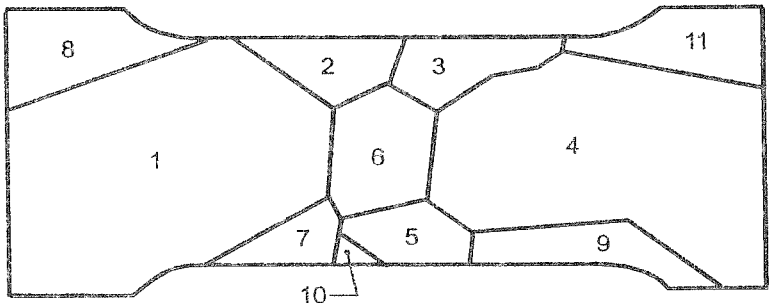

(a)

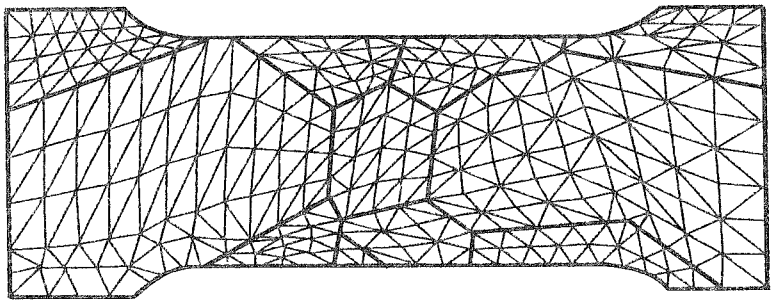

(b)

Figure 5-1 (a) Front face of the tensile specimen defined by 11 grains
(b) Front view of the single layer of pentahedral finite element mesh, (from Teodosiu *et al.* 1992).

The evolution law of these dislocation densities expresses the balance between work-hardening and recovery :

$$\dot{\rho}^s = \frac{1}{b}\left(\frac{1}{s^s} - 2y_c\,\rho^s\right)\left|\dot{\gamma}^s\right| \tag{5-1}$$

where ρ^s is the dislocation density related to the slip system s, b is the magnitude of Burgers' vector, s^s is the average free path of the dislocations in system s, y_c denotes a characteristic length associated with the annihilation process of dislocation dipoles. Clearly s^s depends on the density of point obstacles encountered in the gliding directions. Taking into account only the dislocation-dislocation interactions yields:

$$s^s = \frac{A}{\sqrt{\sum_{u \neq s} \rho^u}} \tag{5-2}$$

where A is a scalar material parameter. Replacing A by a matrix would translate the influence of different dislocation densities on the average free path in a given slip

system. The CRSS on system s can be related to the dislocation densities by the relation :

$$\tau_c^s = Gb\sqrt{\sum_u a^{su}\rho^u} \tag{5-3}$$

where a^{su} is a matrix which takes into account various types of dislocation interactions. Differentiating relation (5-3) with respect to time and considering equations (5-1) and (5-2) lead to the hardening law proposed in (4-16) where h^{su} is given by:

$$h^{su} = \frac{G}{2}\frac{a^{su}}{\sqrt{\sum_q a^{sq}\rho^q}}\left[\frac{1}{A}\sqrt{\sum_{q\neq u}\rho^q} - 2y_c\rho^u\right] \tag{5-4}$$

The matrix h^{su} depends in an explicit way on the current values of the dislocation densities.

Teodosiu's simulation results show in each crystal: slip line patterns, stress, strain, and dislocation density fields. The parameter of non-uniformity q of any scalar field allows to quantify its heterogeneity. It is defined as the ratio between the maximum and minimum absolute values of that field over the specimen.

Figure 5-3 shows the distribution of the stress component σ_{11} in the elastic range and for average engineering strains of 0.13%, 5.7% and 21%. The direction 1 is the tensile direction. One can check that the patterns differ. In the elastic case (Figure 5-3 a), the q parameter of non-uniformity reaches 2.3. The highest gradients occur in the regions where small grains have high misorientation across the grain boundaries. In plastic cases, the q factor decreases to about 1.4 at the beginning by plastic accommodation (Figure 5-3 b). Later, with progressive deformation, q increases again but finally remains stable at a value of 2.0.

The slip line pattern presented in Figure 5-2 results from the projection on the front face of the specimen of line segments oriented as the most active slip systems within each element. The length of each segment is taken proportional to the accumulated glide in the corresponding slip system or, in some cases, in all coplanar systems having the same trace. The agreement with a Scanning Electron Microscopy (SEM) study is reported to be quite satisfactory. The most striking feature of this correlation is that the simulation can really predict the grains partition into subdomains of different single or multislip activity.

The distribution of dislocation densities has been drawn as well. It is much closer to the stress distribution than to the strain distribution. This confirms the proportionality between the flow stress and the square root of the total dislocation density already reported in the literature and used to develop the crystal model relation (5-3).

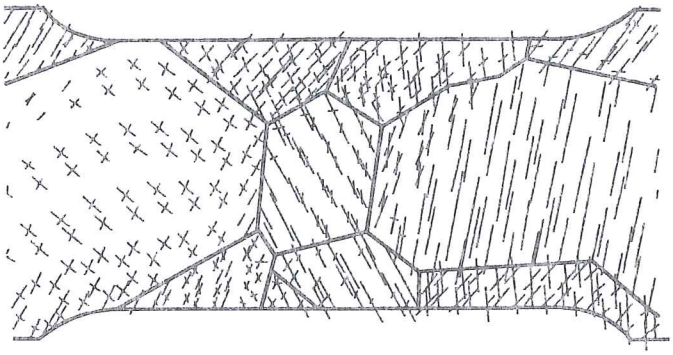

Figure 5-2 Computed slip line pattern at an average engineering strain of 0.13% (from Teodosiu *et al.* 1992).

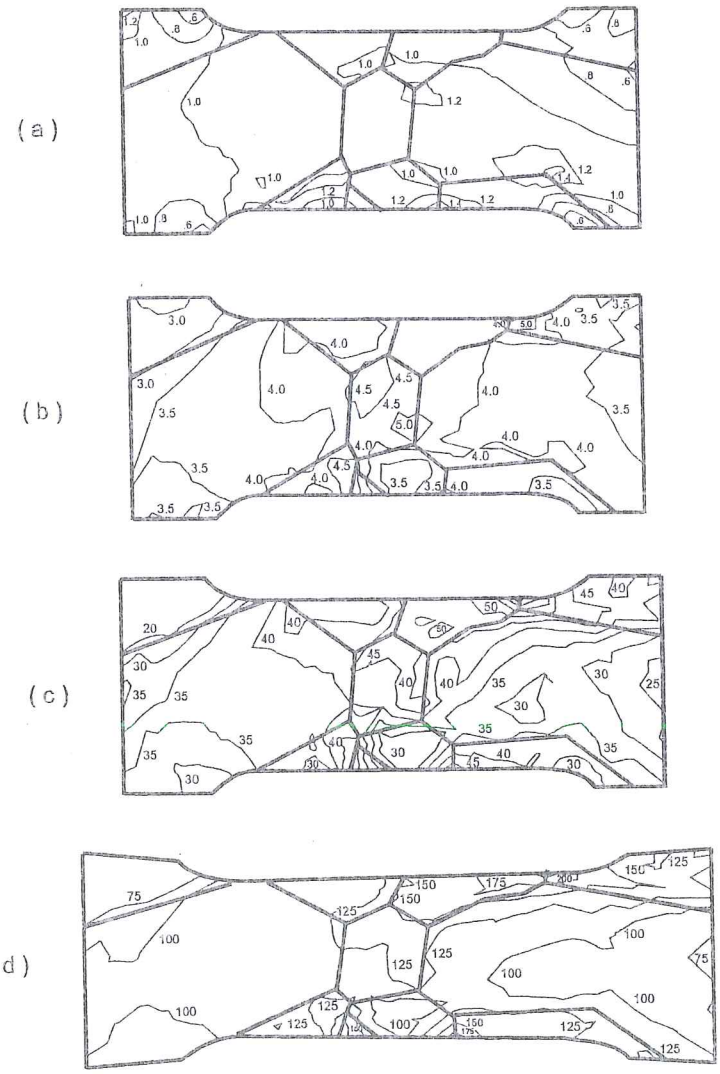

Figure 5-3 Tensile stress in Mpa computed by FEM in the elastic range (a) and for average engineering strains of 0.13% (b), 5.7% (c) and 21% (d) (from Teodosiu *et al.* 1992).

5.2.2. Acharya & Beaudoin's model

Concept

Acharya & Beaudoin 2000 presents a model that is summarized hereafter. Each single crystal undergoes a deformation gradient $\underline{F}$ which is submitted to a multiplicative decomposition:

$$\underline{F} = \underline{F}^* . \underline{F}^p \tag{5-5}$$

where $\underline{F}^*$ is the elastic deformation tensor and $\underline{F}^p$ is the plastic deformation tensor. This approach adopts the isoclinic configuration already introduced in Figure 4.2. As in Teodosiu's approach, a viscoplastic flow rule is applied at the level of each slip system. However a common CRSS for all the slip systems $\tau_c^s = \tau_c$ is used.

When certain types of defect distributions are present in the lattice, the distribution of "isoclinic" configurations cannot constitute a compatible deformation of the current configuration without additional deformation of the material. Consequently, it is reasonable to think of any measure that quantifies this incompatibility in $\underline{F}^{*-1}$ as a measure of certain types of lattice defect distributions.

From mathematical and physical considerations, it can be shown (Acharya & Bassani 2000) that a measure of lattice incompatibility is given by the 3rd order tensor $\underline{\Lambda}$, skew symmetric part of the gradient of $\underline{F}^{*-1}$:

$$\underline{\Lambda} = \left(F^{*-1}_{ij,k} - F^{*-1}_{ik,j} \right) \underline{e}_i \otimes \underline{e}_j \otimes \underline{e}_k \tag{5-6}$$

where ($\underline{e}_i$, $\underline{e}_j$, $\underline{e}_k$) is the basis of a rectangular Cartesian coordinate system parametrizing the current configuration. It can also be shown via Stokes' theorem that :

$$\underline{b}^c = \int_C \underline{F}^{*-1} . d\underline{x} = \int_A \underline{\Lambda} : \hat{\underline{N}} \, da \tag{5-7}$$

where C is a curve bounding a surface region A with unit normal vector $\underline{n}$ in the current configuration. $\hat{\underline{N}}$ is the unique skew symmetric tensor defined for any vector $\underline{a}$ by:

$$\hat{\underline{N}} . \underline{a} = \frac{1}{2} \underline{n} \wedge \underline{a} . \tag{5-8}$$

If we interpret the expression in the middle of (5-7) as a Burgers' circuit on the deformed lattice in the current configuration, then $\underline{b}^c$ can be thought of as the cumulative Burgers' vector of all dislocations threading the region A on the surface with normal $\underline{n}$. Consequently, $\underline{\Lambda}$ can be interpreted as a fictitious density of lattice incompatibility. When integrated over a surface A, limited by a closed curve in the current configuration, it yields the cumulative Burgers' vector difference between the

beginning and the end points of the image curve in the "intermediate isoclinic configuration". Since this difference is conceptually equated with the net Burgers' vector of all the dislocations threading the studied surface, then it is reasonable to interpret the continuous field $\left(\underline{\Lambda} : \underline{\hat{N}}\right)$ as *a cumulative Burgers' vector per unit area.* Therefore, $\left(\underline{\Lambda} : \underline{\hat{N}}\right)/b$, where b is the interatomic spacing for the lattice under consideration or the magnitude of the classical Burgers' vector, yields a continuous field of "*dislocation density*".

$\underline{\Lambda}$ alone cannot represent the total dislocation density in a phenomenological theory. Nevertheless, given its apparent interpretation as a macroscopic manifestation of certain types of dislocations or lattice defect distributions, it is reasonable to say that the evolution of the total dislocation density is affected by $\left(\underline{\Lambda} : \underline{\hat{N}}\right)/b$. A logical consequence is the use of this measure in an evolution equation for hardening.

This proposal is not comforted by a lot of experimental checks but it is worth mentioning, as it links a microscopic mechanical model to microscopic physics. Such a link could help both physical metallurgists and numerical engineers to develop accurate models.

Common CRSS evolution law

With ρ the total dislocation density, $\dot{\gamma}^k$ the slip system shearing rate on system k, $\underline{\dot{\varepsilon}}^{p\ micro}$ the strain rate and T the temperature, Acharya and Beaudoin consider an evolution equation for the dislocation density in a crystal of the form:

$$\dot{\rho} = \sum_{\kappa} \left\{ k_o \frac{\lambda^k}{b} + k_1 \sqrt{\rho} - k_2(\underline{\dot{\varepsilon}}^{p\ micro}, T)\rho \right\} \left| \dot{\gamma}^k \right| \tag{5-9}$$

where

$$\lambda^k = \sqrt{\left(\underline{\Lambda} : \underline{\hat{N}}^k\right)\left(\underline{\Lambda} : \underline{\hat{N}}^k\right)} \tag{5-10}$$

is the slip lattice incompatibility corresponding to system k with unit normal $\underline{n}^k$, k_o is a material constant, k_1 and k_2 are functions defined by relations (5-13) and (5-14).

The first term on the right side of evolution equation (5-9) represents a geometric storage term due to the lattice incompatibility which has been introduced in the previous section. The second term is associated with the dislocation storage through a statistical measure of forest dislocations. The third term is a dynamic recovery rate that renders dislocation segments inactive as they rearrange themselves.

Relation (3-13) defined at the macroscopic level can of course be expressed at the level of the common reference CRSS assumed in a crystal:

$$\tau_c = \tau_{c0} + \alpha G b \sqrt{\rho} \tag{5-11}$$

The time differential of this relation, coupled with relation (5-9), yields:

$$\dot{\tau}_c = \frac{k_o \alpha^2 G^2 b}{2(\tau_c - \tau_{co})} \sum_{\kappa} \lambda^k \left|\dot{\gamma}^k\right| + \left\{ \frac{\alpha G b}{2} k_1 - k_2 \frac{\tau_c - \tau_o}{2} \right\} \sum_{k} \left|\dot{\gamma}^k\right| \qquad (5\text{-}12)$$

Defining θ_o as the strain-hardening rate that prevails at initial yield and τ_{sat} as the saturation stress $\left(\dot{\tau}_c(\tau_{sat}) = 0\right)$ which depends on strain-rate and temperature, the following relations are obtained :

$$k_1 = \frac{2\theta_o}{\alpha G b} \qquad (5\text{-}13)$$

$$k_2(\underline{\dot{\varepsilon}}^{p\,micro}, T) = \frac{2\theta_o}{\tau_{sat}(\underline{\dot{\varepsilon}}^{p\,micro}, T) - \tau_{co}} \qquad (5\text{-}14)$$

Substituting relations (5-13) and (5-14) in (5-12), an isotropic, single crystal work hardening model is obtained :

$$\dot{\tau}_c = \frac{k_o \alpha^2 G^2 b}{2(\tau_c - \tau_{co})} \sum_{\kappa} \lambda^k \left|\dot{\gamma}^k\right| + \theta_o \left\{ \frac{\tau_{sat} - \tau_c}{\tau_c - \tau_{co}} \right\} \sum_{\kappa} \left|\dot{\gamma}^k\right| \qquad (5\text{-}15)$$

It can also be shown that λ^k is invariant under superposed rigid body motions (Acharya & Bassani, 2000); it thus satisfies the invariance requirement for a constitutive assumption.

Numerical applications to predict macroscopic stress-strain behavior

Acharya & Beaudoin use 3D FEM simulations to model aggregates of single crystals where velocity boundary conditions allow to represent uniaxial tensile or compression tests (Figure 5-4).

Simulations were performed with coarse and fine discretizations, the number of elements per grain was 12 and 96 for the 12x12x12 and 24x24x24 meshes respectively. Using the 12x12x12 mesh, simulations were carried out for grain diameters of 200 μm, 91 μm, 32 μm, 20 μm. Additional grain diameters of 50 μm and 25 μm were considered with the finer mesh. Each grain is characterized by its lattice orientation. The hybrid finite element formulation adopted by Beaudoin *et al.* 1995 is used. This model assumes that the plastic part of the velocity gradient is specified by the activation of multiple slip systems as already explained in Taylor's single crystal plasticity (see section 4.1). A viscoplastic flow rule (relation 4-15), coupled with the above CRSS evolution (5-15), links stress and plastic strain rate.

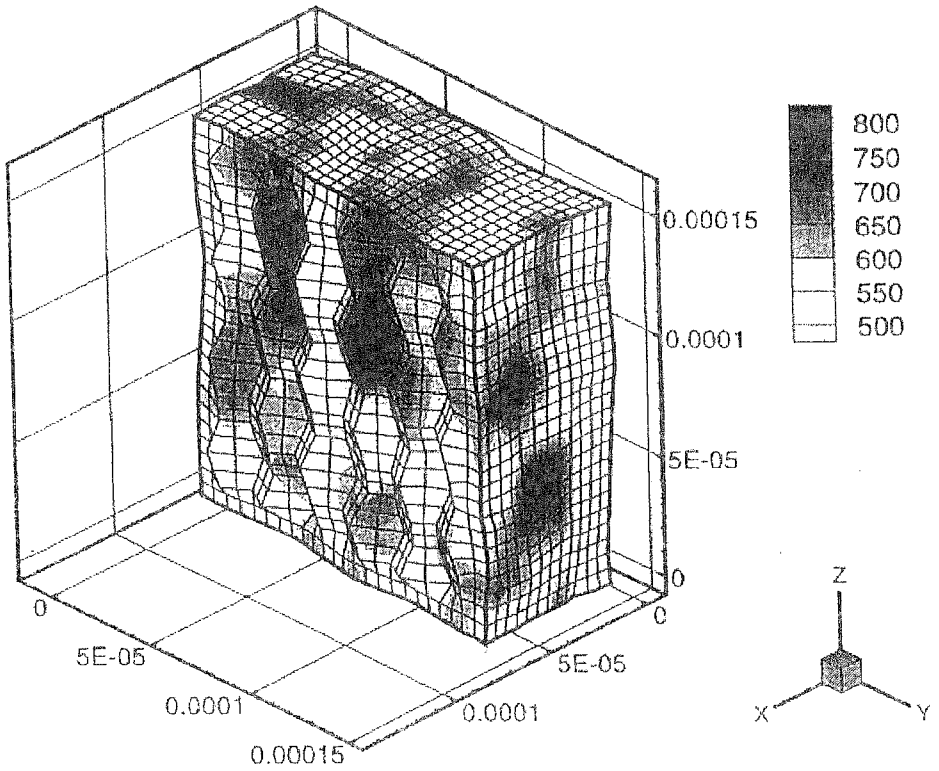

Figure 5-4 Polycrystal aggregate with initial grain diameter of 32μm submitted to a tensile strain of 20 %; von Mises equivalent stress is plotted in units of Mpa and dimensions are given in m (from Acharya & Beaudoin 2000).

The model requires the identification of 4 parameters: θ_0, τ_{sat}, τ_{c0}, k_0. Thanks to comparisons between experiments and simulation results, a data set can be determined. From computations applied to pure nickel, it appears that the contribution of term λ^k due to "lattice incompatibility", evaluated by relation (5-10), is relatively small for large grain size (200 μ m) but becomes more significant with decreasing grain size.

Whatever the mesh refinement, Figure 5-5 shows a clear relationship between macroscopic yield stress and grain size. Lines fitted to simulation results show a slight deviation from linearity with the inverse of the grain size, in fact $\sigma \div D^{-4/5}$ is found. Well known scientists, such as Ashby for instance, propose relations where the yield stress is proportional to $D^{-1/2}$, see the review presented in François *et al.* 1992. Acharya & Beaudoin do not comment this difference, as their results are quite close to the experimental ones.

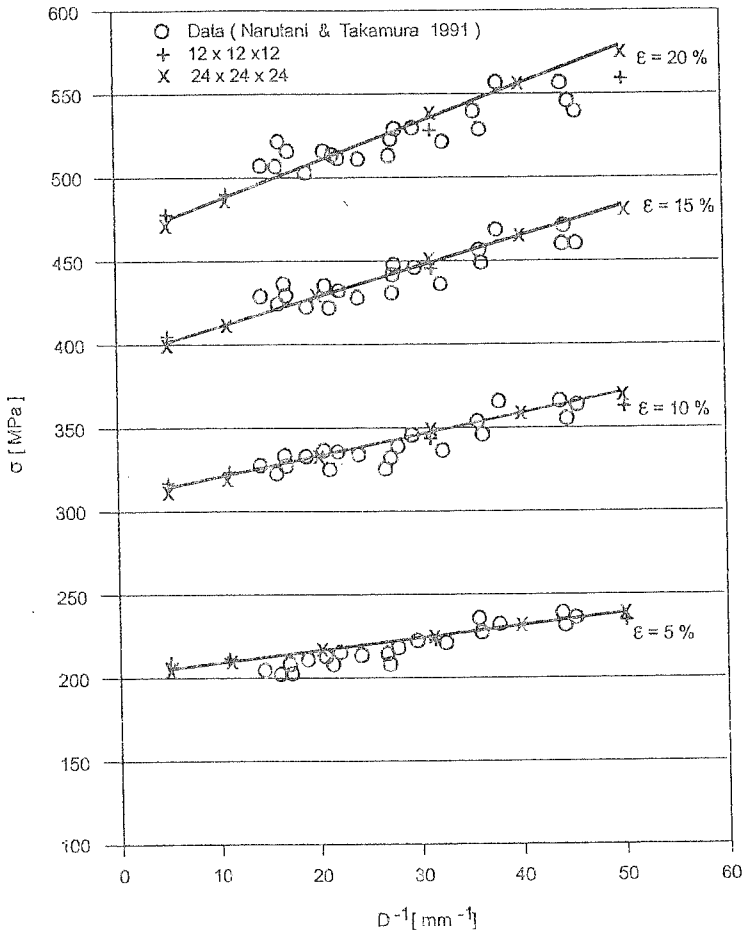

Figure 5-5 Effect of grain size D on volume-averaged stress response of nickel at 77 K° from Acharya & Beaudoin 2000.

5.3. Macroscopic FEM simulations relying on discrete set of crystals

In this type of simulations, the response of each integration point depends on the response of a multitude of single grains, representative of this material point. This can be done only thanks to massive parallel computations. Simulations like hydroforming process, performed by Dawson *et al.* 1992, show that, with powerful computers, this approach can be applied to real problems of limited size. Clearly, in addition to the usual choices in a FEM approach (lagrangian, eulerian formulation, explicit, implicit scheme, ...), the scientist must determine further assumptions:

Step 1 : **the micro-macro link** (Full Constraint, Relaxed Constraint Taylor's model or one of their variants, self-consistent model, homogenization technique).
It allows to go from a macroscopic velocity gradient to microscopic values and to provide, after computations at microscopic level, the macroscopic stress.

Step 2 : **the set of representative crystals.**
The number of crystals must be determined as well as their orientation, shape, size, slip system and associated CRSS. The initialization of these crystal data is essential for the accuracy of the results.

Step 3 : **the behavior model of each crystal.**
In this type of models, elasticity can be neglected or taken into account. The crystal plasticity model defines the link between the resolved shear stress and the slip system rate. The CRSS hardening rule is also a key function that induces differences between the models. As shown hereafter, two different proposals exist: viscoplasticity or rate independent plasticity. Finally, the microscopic stress related to the microscopic velocity gradient is computed.

Of course, all these options interact and have strong effects on the accuracy and computation time. Well-known scientists have proposed various models in order to describe polycrystal models. Some of these models are presented hereafter, together with their advantages and drawbacks.

5.3.1. Taylor's model + Polycrystal models

Such polycrystal models are described for instance in Asro & Needleman 1985, Mathur & Dawson 1989, Becker 1990, Neale 1993, Beaudoin *et al.* 1994, Kalidindi & Anand 1994, Anand *et al.* 1997. The above general choices are clearly identified hereafter.

Micro-Macro Link

Taylor's polycrystal model is used. This implies that the local deformation gradient in each grain is set homogeneous and identical with the macroscopic deformation gradient.

The elasticity is generally neglected in the work performed by Dawson's team (Mathur & Dawson 1989, Beaudoin *et al.* 1994):

$$\underline{F}^{macro} = \underline{F}^{micro} = \underline{R}^{*}\,\underline{F}^{P} \tag{5-16}$$

$\underline{R}^{*}$ being a rotation matrix. But elasticity is taken into consideration by scientists working with Anand (Kalidindi & Anand 1994, Anand *et al.* 1997):

$$\underline{F}^{macro} = \underline{F}^{micro} = \underline{F}^{*}\,\underline{F}^{P} \tag{5-17}$$

with $\underline{F}^{*}$ defined by Figure 4-2.

If the N representative grains or crystals have equal volume, a simple average is used to link micro and macro stress tensors (Kalidindi & Anand 1994).

$$\underline{\sigma}^{macro} = \frac{1}{N}\sum_{k=1}^{N} \underline{\sigma}^{micro(k)} \qquad (5\text{-}18)$$

Otherwise, a weighted average based on the volume fraction W_k of each crystal orientation is used (Beaudoin *et al.* 1994).

$$\underline{\sigma}^{macro} = \sum_{k=1}^{N} W^k \, \underline{\sigma}^{micro(k)} \qquad (5\text{-}19)$$

Clearly, the average used to reach the macroscopic stress tensor depends on the choice of the representative set of crystals.

Representative set of crystals

Number of crystals : N varies depending on simulations and authors. For instance, 180 or 200 crystals per integration point are used for compression tests (Kalidindi & Anand 1994), 32 for cup-drawing (Anand *et al.* 1997), 256 for hydroforming process (Beaudoin *et al.* 1994), 200 for titanium rolling (Dawson & Kumar, 1997)…

Orientation of crystals: experimental data from X-ray diffraction measurements of crystallographic texture give discrete intensities of diffracted energy as a function of goniometer position angles. This can be transformed into a "*Crystal Orientation Distribution Function*" ODF as explained in section 3.2 and can be used to generate a set of "weighted Euler angles".

According to "popLA package" (Kallend *et al.* 1991), two approaches are proposed to approximate a texture defined by a continuous density distribution through a set of discrete orientations. In the first approach, all orientations have the same *weight*. Since the crystals are assumed to have the same volume, they are located in the orientation space so that higher density regions are more densely populated. The second approach consists in randomly populating the orientation space with discrete orientations and assigning to each of them an initial weight that minimizes the effect of the density fluctuations arising from the discretization. The weight of each discrete orientation is then multiplied by the actual density in the associated volume of orientation space. This provides a weighted orientation approach generally used by Dawson and his co-workers (see relation (5-19)), while Anand's team generally uses the first approach with identical weights (see relation (5-18)).

This initial set of orientations is updated during the computations. Section 4.4 explains how the computation of the crystal lattice rotation $\underline{\Omega}^L$ for a single crystal is directly applicable, thanks to Taylor's assumption of identical deformations at microscopic and microscopic levels (see relations (5-16) and (5-17)).

Slip systems: the slip systems are well known for f.c.c materials like aluminum, copper or b.c.c materials like steel, tantalum, h.c.p. materials like zinc, zircalloy…

CRSS: as explained in section 4.3, the hardening of each CRSS associated to a slip system should be taken into account as well as its initial value. Very often, the values of the initial CRSS of all slip systems are assumed equal or close to each other (van Bael 1994, see relation (4-5)). In an annealed state for f.c.c or b.c.c materials, this seems reasonable. From numerous simulations of homogeneous deformations of f.c.c materials (Kalidindi *et al.* 1992), it has been observed that, after large deformations, the values of the CRSS for the various slip systems in an aggregate are quite close to each other. This common value is estimated from a macroscopic simple compression test.

Shape: this cannot be taken into account in a classical polycrystal Taylor's model.

Behavior model of each crystal

Mathur & Dawson 1989 and Beaudoin *et al.* 1994 neglect elasticity (5-16) and use a rate dependant plasticity model described for each slip system by relation (4-15), recalled here:

$$\dot{\gamma}^s = \dot{\gamma}_0 \left| \frac{\tau^s}{\tau_c^s} \right|^{1/n} sign\, \tau_s \qquad (4\text{-}15)$$

They also adopt a common average value for all CRSS in one crystal:

$$\tau_c^s = \tau_c \qquad (5\text{-}20)$$

and choose a simple evolution law of Voce's type, already referred to in Follansbee and Kock's model (section 3.5.2.) :

$$\dot{\tau}_c = H_0 \frac{\tau_{sat} - \tau_c}{\tau_{sat} - \tau_{c0}} \quad \text{and} \quad \tau_{sat} = f(\dot{\Gamma}) \qquad (5\text{-}21)$$

where Γ = total shear slip on all slip systems of the crystal;
τ_{sat} = saturation value of the common reference CRSS;
τ_{c0} = initial value of the common reference CRSS;
H_0 = material parameter.

In Beaudoin *et al.* 1994, a hydroforming process (Figure 5-6) is chosen to validate the numerical FEM model. This choice seems very well adapted to check the model of the blank behavior :

- applied pressure assures stability;
- contact and friction models do not introduce inaccuracy; punch and blank are in sticking conditions and blank-flange contact is assumed frictionless.

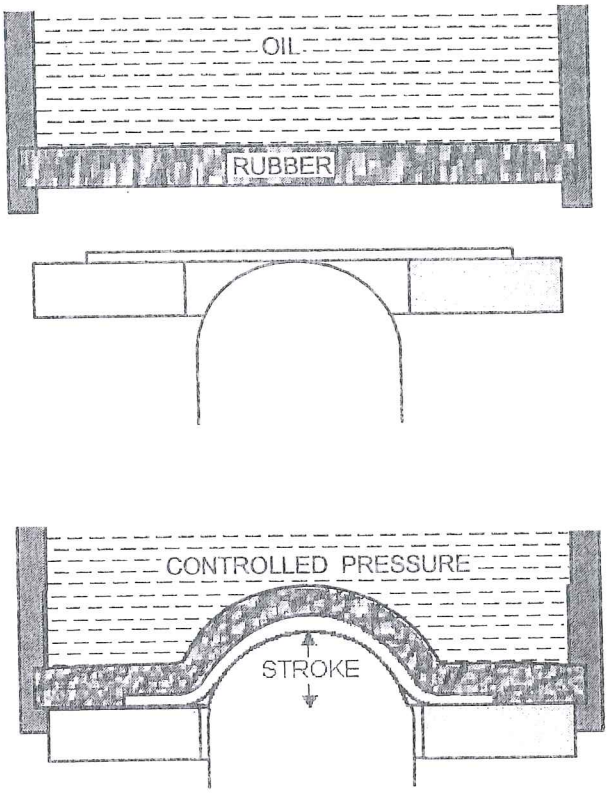

Figure 5-6 Axisymmetrical hydroforming process of an aluminum sheet (adapted from Beaudoin *et al.* 1994).

Consequently the final deformed shape depends on the material anisotropy and is measured by the percentage of earing. As shown in Figure 5-7, numerical results are close to experimental measurements :

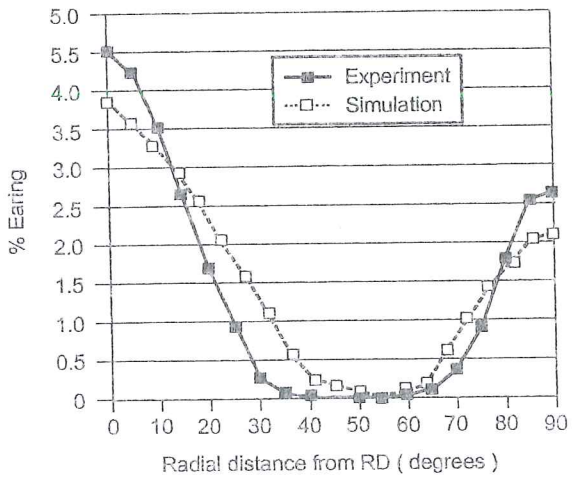

Figure 5-7 Earing measurement and prediction at the final stage of a hydroforming process (from Beaudoin *et al.* 1994).

For this case, it was checked that the texture evolution during the process and its effect on the shape of the yield locus are minimal.

In **Anand & Kothari 1996**, a viscoplastic flow rule (relation (4-15)) is compared with a rate-independent crystal plasticity model. A robust calculation scheme determines a unique set of active slip systems and the corresponding shear increments in the rate-independent theory. In both models, an evolution rule for the CRSS associated to each slip system τ_c^s is applied. The general form, already presented in section 4.3, is applied :

$$\dot{\tau}_c^s = \sum_u h^{su}\, \dot{\gamma}^u \tag{4-16}$$

This relation comes from Asro & Needleman 1985 and the chosen hardening matrix h^{su} for the 12 slip systems of f.c.c crystals is:

$$h^{su} = h^u \begin{Bmatrix} A & qA & qA & qA \\ qA & A & qA & qA \\ qA & qA & A & qA \\ qA & qA & qA & A \end{Bmatrix} \quad \text{with } A = \begin{Bmatrix} 1 & 1 & 1 \\ 1 & 1 & 1 \\ 1 & 1 & 1 \end{Bmatrix} \tag{5-22}$$

where systems 1, 2, 3 are coplanar, as systems 4, 5, 6 and 7, 8, 9 and 10, 11, 12 are. For coplanar systems, the ratio of the latent hardening rate to the self hardening rate is equal to unity. For non coplanar systems, it is evaluated by means of factor q=1.4. The function h^u is defined by :

$$h^u = h_0 \left(1 - \frac{\tau_c^u}{\tau_{sat}} \right)^a \tag{5-23}$$

where h_0, a and τ_{sat} are slip system hardening parameters which are taken identical for all slip systems. In fact, τ_{sat} should be an increasing function of strain rate but this can be neglected at low temperature. These parameters are reached by curve-fitting between the results of simple compression tests and numerical simulations using "Taylor's model". By "Taylor's model", one must understand: the TBH model applied at the crystal level with Taylor's assumption of equality between microscopic and macroscopic strain rates. This model uses (4-16) and (5-23) to follow the evolution of the CRSS of each slip system in each crystal. One can check that the initial value of CRSS τ_{c0} influences the initial yield, τ_{sat} the final saturated value of stress, h_0 affects the initial hardening rate and a modifies the shape of the polycrystal stress-strain curve between the initial yield and saturation.

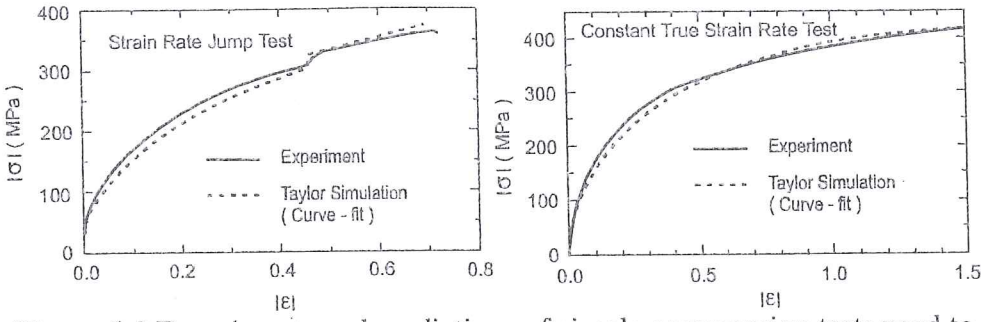

Figure 5-8 Experiments and predictions of simple compression tests used to determine the viscoplastic material parameters in Taylor's model.
a- Strain rate jump test b- Constant true strain rate test
(from Kalidindi & Anand 1994).

If the TBH model is replaced by a rate dependent visco-plastic law (relation 4-15), it has two additional parameters: $\dot{\gamma}_0, n$. For copper, according to Kalidindi & Anand 1994, $\dot{\gamma}_0$ is assumed to have a constant value of 0.012 and n is chosen equal to the corresponding macroscopic parameter. This latter is identified thanks to a strain rate jump experiment on a polycrystalline specimen in compression state at room temperature.

The first "micro-macro model" used here is simply Taylor's assumption of $\underline{\dot{\varepsilon}}^{micro} = \underline{\dot{\varepsilon}}^{macro}$, linked with a TBH model or a visco-plastic approach (4-15). It has no coupling with FEM and allows the identification of τ_{co}, τ_{sat}, h_o, a and $\dot{\gamma}_o$, n. All these parameters are necessary to describe the single crystal behavior.

Finally, Figure 5-8 shows the comparison between "Taylor's model" and experiments for a copper with isotropic texture represented by 200 crystals.

Then, Anand and co-workers (Kalidindi & Anand 1994, Anand & Kothari 1996, Anand *et al.*1997) apply the micro-macro model described above at each interpolation point of a finite element mesh. The behavior of copper and aluminium is simulated by means of Taylor's model. In particular, compression tests of cylindrical specimens, plane strain compression experiments, forging experiments (Figure 5-9), cup drawing experiments (see Figure 1.3) are performed. Experimental and numerical loads, geometric shapes and texture evolutions (Figure 5-10 and Figure 5-11) are compared as well.

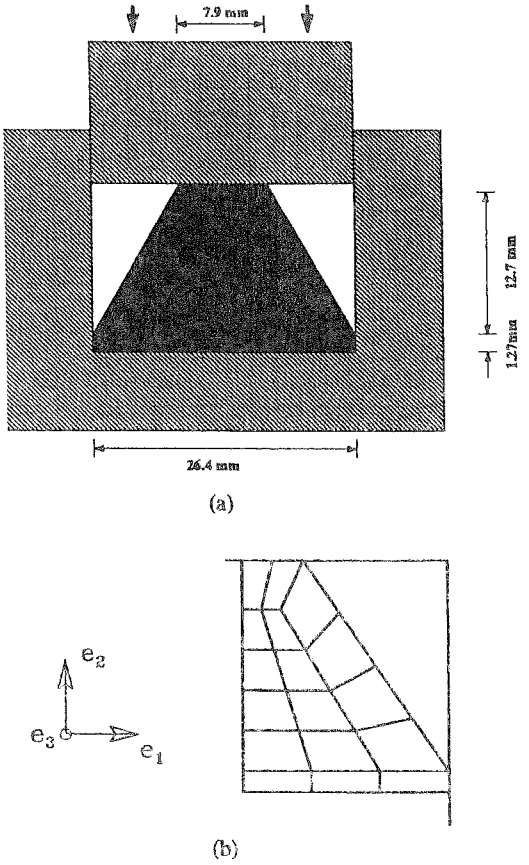

Figure 5-9 (a) Scheme of a plane strain forging experiment performed on an initially isotropic copper, (b) Coarse mesh used in Abaqus finite element simulation with 180 single crystals per integration point (from Kalidindi & Anand 1994).

The conclusion is that the model gives reasonable accuracy for engineering purpose. Such a model has been successfully applied to high deformation rate of tantalum (Anand *et al.*1997).

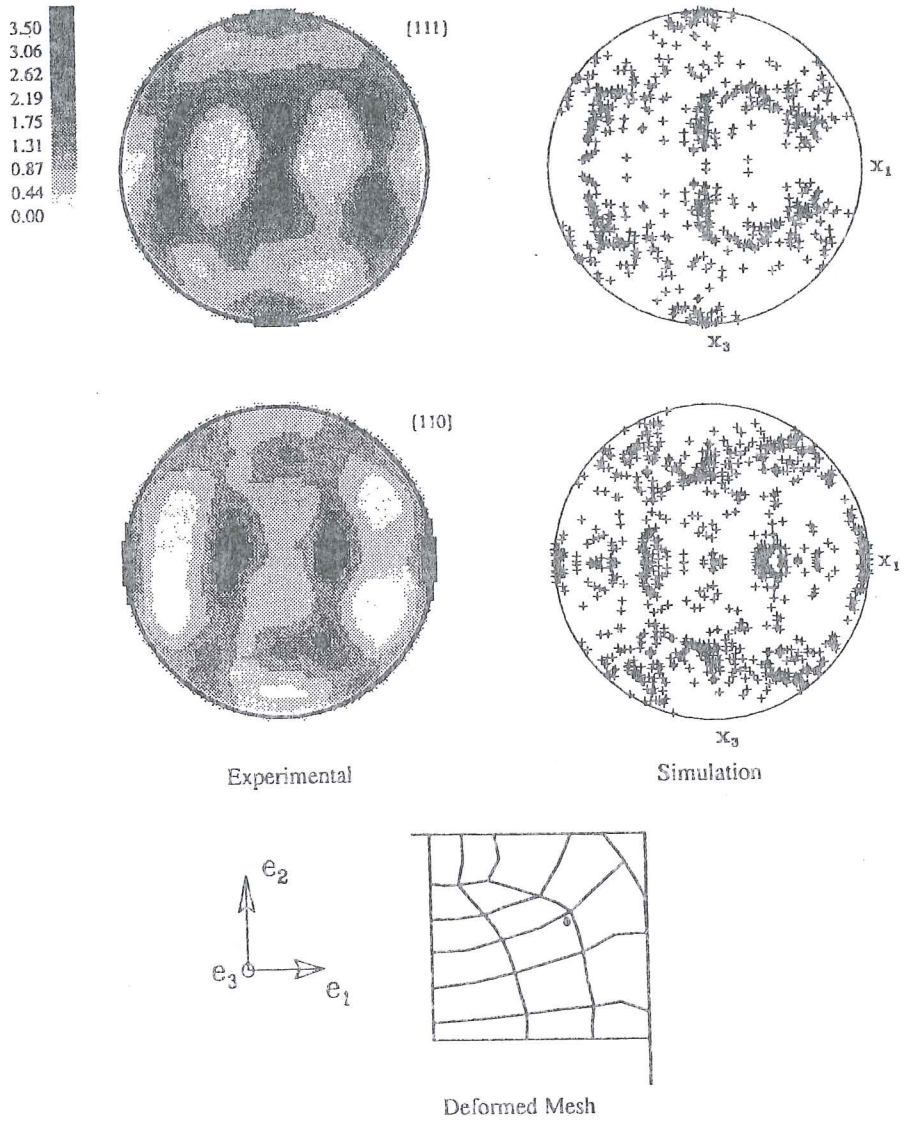

Figure 5-10 Measurement in forging experiment and prediction by FEM simulation of the {111} and {110} pole figures in the deformed specimen at the point indicated in the deformed mesh (from Kalidindi & Anand 1994).

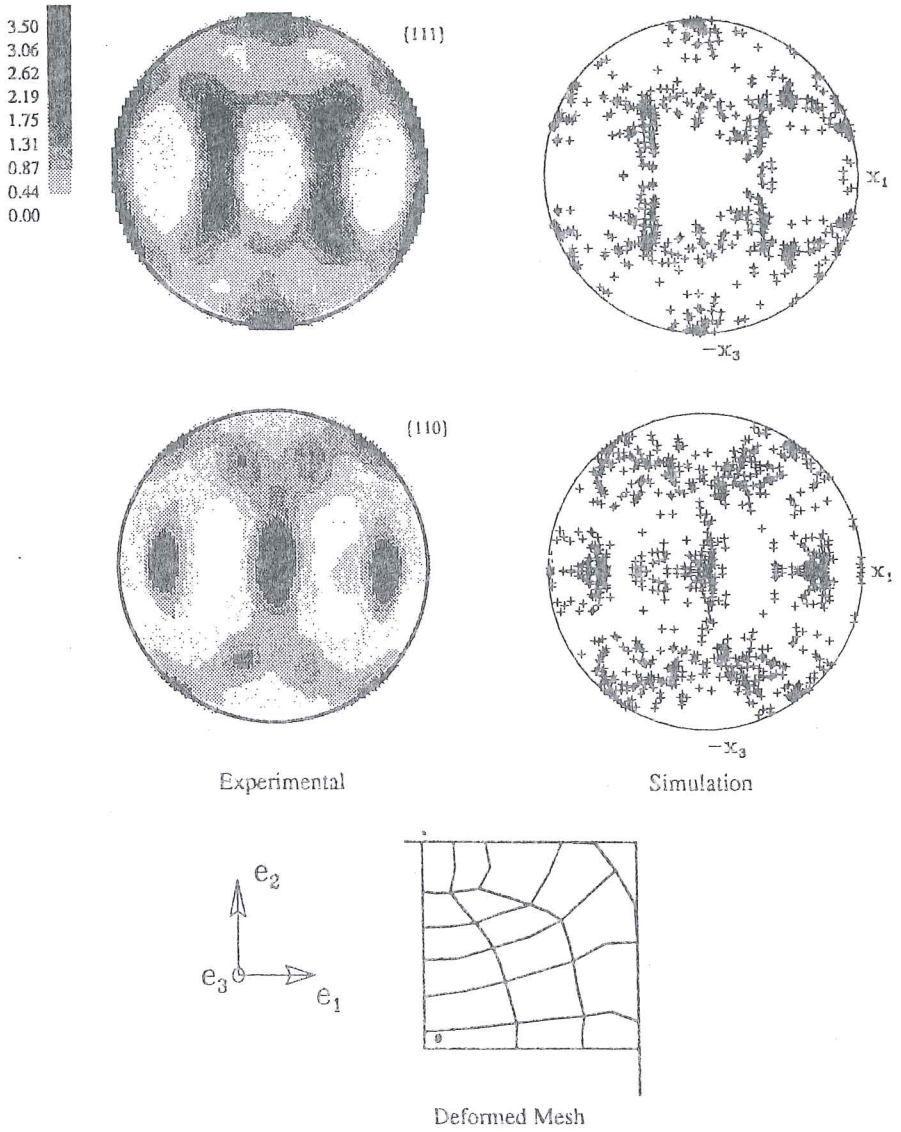

Figure 5-11 Measurement in forging experiment and prediction by FEM simulation of the {111} and {110} pole figures in the deformed specimen at the point indicated in the deformed mesh (from Kalidindi & Anand 1994).

Conclusion

In short, the previous examples using Taylor's model, coupled with finite elements, show that such approach is feasible and has been validated for b.c.c and f.c.c materials. If a high number of representative crystals at the microscopic level is used, this can provide accurate predictions of texture, geometry and stress history during any cold forming process. The texture evolution is directly implemented in this approach. This means that the "geometrical hardening", responsible for the shape modification of the yield locus is directly taken into account. This characteristic constitutes an advantage of this type of models with respect to others, such as the phenomenological yield loci coupled with kinematic and isotropic hardening. These

cannot easily represent texture evolution effect. As explained above, this method does not use a global yield locus but an average answer computed from the plastic behavior of a set of representative crystals.
Taylor's model coupled with finite elements requires a high CPU time and memory storage, directly proportional to the number N of crystals associated to one integration point. It is quite surprising that this number N has not been more investigated. Very often, measured pole figures are qualitatively compared to the ones computed from the discrete set of orientations (Anand & Kothary 1996). No further study from a mechanical point of view, such as stress response computed for the same strain and different N values, is performed. For each of the N representative crystals associated with one integration point, one must store:

- the crystal orientation, typically defined by 3 variables;
- hardening variable(s): either one reference CRSS τ_c, as in relation (5-21), if a common reference value for all slip systems is adopted, or one CRSS τ_c^s for each slip systems s as in equation (5-23).

5.3.2. Self-consistent approach + Polycrystal models

As explained in section 4.5, the self-consistent approach respects, on the average, both compatibility and equilibrium between grains. It is intensively used by scientists aiming to understand and predict the macroscopic material behavior thanks to micro-macro models (Canova & Lebensohn 1995, Molinari 1997, Nikolov & Doghri 2000). However, this great advantage is shaded by the increase of computation time. This fact explains why it is seldom used for coupling with FEM models. It is not surprising that self-consistent approach applications appear for hexagonal materials like Zircalloy (Chastel *et al.* 1998) because the low number of deformation modes in such crystals yields inaccurate predictions with Taylor's model.

Chastel *et al.* 1998 present a viscoplastic self-consistent polycrystalline model (Lebensohn & Tomé 1993) coupled to a 3D Eulerian finite element code LAM3 (Hacquin *et al.* 1995), applied to the hot extrusion of Zircalloy. In practice, the finite element calculation starts with an isotropic rheology, which provides a first deformation gradient at each interpolation point. Then, the polycrystalline model is locally activated and provides an anisotropic response of the material which induces subsequent calculation in LAM3. For this case, the final flow patterns reached by the macroscopic approach and by the micro-macro computation are very close to each other as they are mainly fixed by the kinematic boundary computations. Discrepancies between predicted and measured texture evolutions are attributed to the occurrence of recrystallization and/or recovery phenomena, which are not taken into account in the model.

To summarize, such a method allows to consider directly "textural hardening" as Taylor's model coupled with finite elements does. It is more satisfactory from a scientific point of view since, at the microscopic level, both compatibility and equilibrium are approached. The grain shape can be taken into account at the

microscopic level. The case of crystals with a low number of deformation modes seems to require this type of model for accurate predictions. The cost in memory is identical with Taylor's approach. However, the CPU time, which is already a problem with Taylor's model, is even worse here, as an iterative process is needed to find the heterogeneous strain repartition between crystals. This explains why so few macroscopic FEM models are linked to self-consistent microscopic models. Progresses in this direction are on their way. It must be pointed out that with "object programming", it is not a real problem to replace a Taylor's model by a self-consistent one.

5.3.3. Homogenization approach + Polycrystal models

Micro-Macro Link

Proposals by Smit *et al.* 1998, Miehe *et al.* 1999, Geers *et al.* 2000 or Feyel & Chaboche 2000 are directly based on mathematical procedures already applied in composite materials. Two levels of finite element models are used: at every interpolation point of the macroscopic FEM mesh, another microscopic FEM model, simulating a Representative Volume Element (RVE), is called to provide the stress-strain behavior of the material.
In other words, the constitutive law at a macroscopic point results from the global response given by a FEM analysis of a set of representative crystals (RVE) described by a microscopic behavior model. These 2 levels of computation are represented in Figure 5-12.

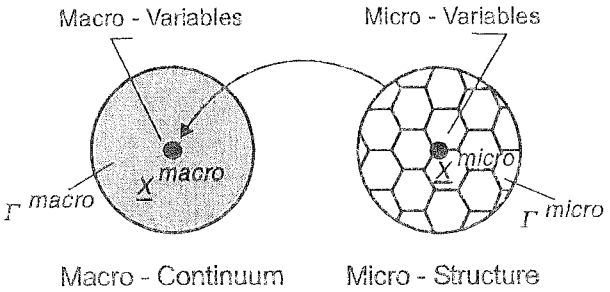

Figure 5-12 Presentation of the macroscopic and microscopic levels (adapted from Miehe *et al.* 1999).

The homogenization approach provides the mathematical background to go from the microscopic level to the macroscopic level. Figure 5-13 presents the mathematical description of the same deformation at macroscopic and microscopic levels.

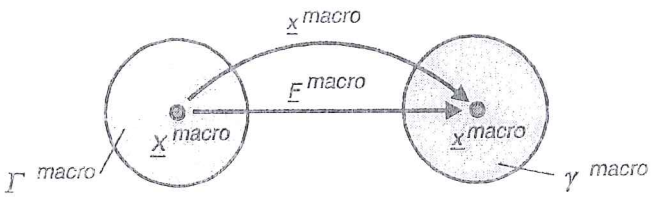

a. Deformation of Macro - Continuum

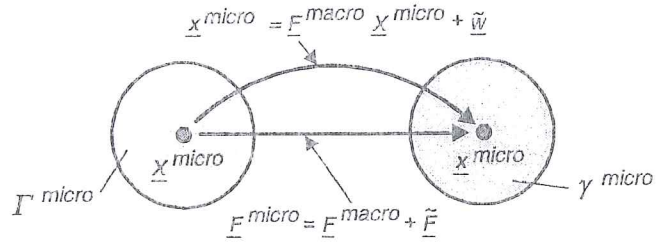

b. Deformation of Micro - Structure

Figure 5-13 Schematic diagram of the deformation at the macroscopic and microscopic levels (adapted from Miehe *et al.* 1999).

In Figure 5-12, Figure 5-13 and Figure 5-14, the superscript *macro* relates to the macroscopic mesh and the superscript *micro* identifies variables attached to the RVE considered at the microscopic simulation level. The following notations are introduced:

$\Gamma^{macro\ or\ micro}$	initial configuration,
$\gamma^{macro\ or\ micro}$	deformed configuration associated to the initial one,
$\underline{X}^{macro\ or\ micro}$	coordinate tensor in the initial configuration,
$\underline{x}^{macro\ or\ micro}$	coordinate tensor in the deformed configuration,
$\underline{F}^{macro} = \frac{\partial \underline{x}^{macro}}{\partial \underline{X}^{macro}}$	macroscopic deformation gradient tensor ,
$\underline{F}^{micro} = \frac{\partial \underline{x}^{micro}}{\partial X^{macro}}$	microscopic deformation gradient tensor,
$\underline{n}^{\Gamma}$	outward normal of the initial configuration of the RVE,
$\underline{n}^{\gamma}$	outward normal of the deformed configuration of the RVE.

The following averaging relations define the macroscopic gradient tensor and the macroscopic first Piola Kirchhoff stress $\underline{\tau}^{macro}$ from their values at a microscopic scale :

$$\underline{F}^{macro} = \frac{1}{V}\int_{\Gamma^{micro}} \underline{F}^{micro}\, dV \qquad (5\text{-}24)$$

$$\underline{\tau}^{macro} = \frac{1}{V}\int_{\Gamma^{micro}} \underline{\tau}^{micro}\, dV \tag{5-25}$$

The application of Gauss' theorem leads to:

$$\underline{F}^{macro} = \frac{1}{V}\int_{\Gamma^{micro}} \underline{F}^{micro}\, dV = \frac{1}{V}\int_{\partial\Gamma^{micro}} \underline{x}^{micro} \otimes \underline{N}^{\Gamma}\, dA \tag{5-26}$$

$$\underline{\tau}^{macro} = \frac{1}{V}\int_{\Gamma^{micro}} \underline{\tau}^{micro}\, dV = \frac{1}{V}\int_{\partial\Gamma^{micro}} \underline{t}^{micro} \otimes \underline{X}^{micro}\, dA \tag{5-27}$$

where the tension on the boundary $\partial\Gamma^{micro}$ is defined by :

$$\underline{t}^{micro} = \underline{\tau}^{micro}\,\underline{n}^{\Gamma} \tag{5-28}$$

Figure 5-14 a. illustrates the above theoretical considerations. Figure 5-14 b., c., d. present different microscopic finite element meshes: one element per crystal grain (b.), regular square elements mesh (c), mesh of triangles applied on the crystals (d).

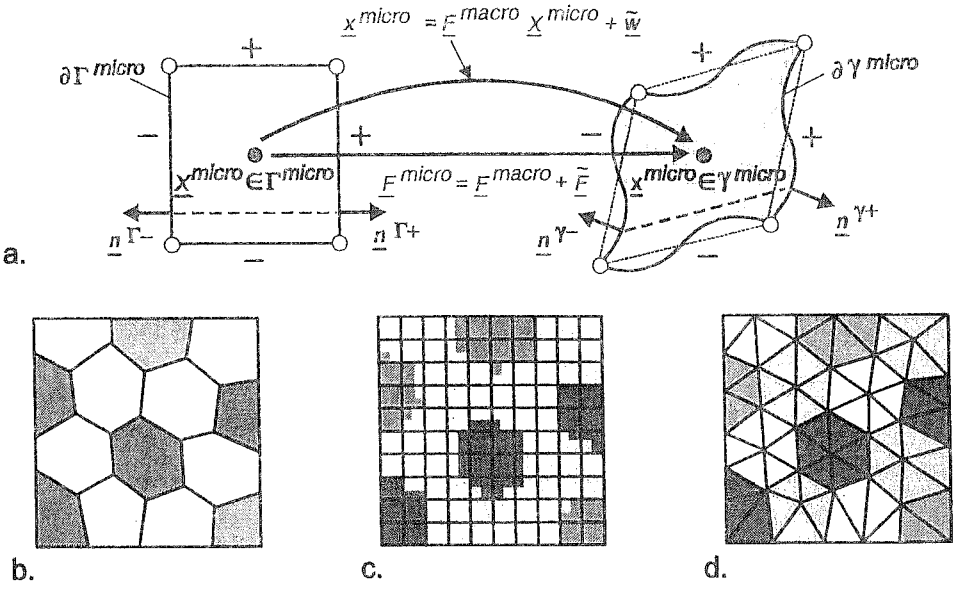

Figure 5-14 a. Deformation of the microstructure level
b., c. , d. Finite element meshes applied to the initial shape of the RVE, where crystals are identified by different grey colors
(adapted from Miehe *et al.* 1999).

The deformation assumption in the RVE is related to macroscopic values by:

$$\underline{x}^{micro} = \underline{F}^{macro}.\,\underline{X}^{macro} + \tilde{w} \tag{5-29}$$

$$\underline{F}^{micro} = \underline{F}^{macro} + \tilde{\underline{F}} \tag{5-30}$$

The assumption (5-30) coupled with the previous average equation (5-26) leads to:

$$\frac{1}{V}\int_{\Gamma^{micro}} \tilde{\underline{F}} dV = \frac{1}{V}\int_{\partial\Gamma^{micro-}} \tilde{\underline{w}} \otimes \underline{n}^{\Gamma^-} dA + \frac{1}{V}\int_{\partial\Gamma^{micro+}} \tilde{\underline{w}} \otimes \underline{n}^{\Gamma^+} dA = 0 \qquad (5\text{-}31)$$

with $\underline{N}^{\Gamma^+} = -\underline{N}^{\Gamma^-}$ at 2 associated points of the contour (Figure 5-14 a.).

This general mathematical frame shows that 3 alternative possibilities directly satisfy relation (5-31) :

- $\tilde{\underline{w}} = 0$ everywhere in Γ^{micro} : Taylor's assumption $\underline{F}^{micro} = \underline{F}^{macro}$ is recovered, no superimposed deformation field at the microscale;
- $\tilde{\underline{w}} = 0$ on the contour $\partial\Gamma^{micro}$: zero fluctuation of the superimposed deformation field $\tilde{\underline{w}}$ on the boundary but non zero fluctuation inside the RVE;
- $\tilde{\underline{w}}^+ = \tilde{\underline{w}}^-$ on the contour $\partial\Gamma^{micro}$: periodic fluctuation of the superimposed deformation field $\tilde{\underline{w}}$ on the boundary.

Set of representative crystals

All the examples presented in Miehe *et al.* 1999 start from an isotropic texture easily represented by random crystal orientations. According to the size of the macroscopic mesh, the number of finite elements in the RVE varies.

For instance, in a validation test simulating a simple shear loading, one macroscopic element is used, coupled with 100 finite elements in the RVE. Each of them has one integration point associated with one crystal orientation. The texture predictions resulting from the 3 alternative choices for the $\tilde{\underline{w}}$ field are quite close to each other.

Another example of punch indentation was computed using 100 macroscopic finite elements, each of them linked with 400 crystal grains in the RVE.

Behavior model of each crystal

Miehe *et al.* 1999 provides one of the most complete micro-macro models: it considers the anisotropic elasticity in each crystal coupled with a plastic or viscoplastic anisotropic behavior. This model takes into account thermomechanical behavior as well. The rate dependent plastic behavior is quite classical and the rate independent plastic approach proposes an extension of the work of Kothari & Anand 1996.

Conclusion

The advantages of this approach are that texture and grain shape or size effects are directly taken into consideration. Like in the self-consistent approach, both equilibrium and compatibility between crystals are reached in the RVE. The effects of 3 different assumptions at the microscopic scale (Taylor's, no fluctuation or periodic fluctuation on the boundary) are easily considered. One significant drawback is the amount of computations and memory requirements, which are even

worse than with self-consistent and Taylor's models coupled with macroscopic FEM simulations. For instance, the variables describing the microscopic FEM simulation (nodal positions, state variables at every microscopic integration point: crystal orientation, reference CRSS or CRSS for each slip systems...) associated to every macroscopic integration point must be stored. So far, no industrial examples were simulated with this approach.

5.4. Macroscopic FEM simulations with microscopic models

Micro-Macro Link

Nakamachi & Dong 1997, Nakamachi *et al.* 1999a, Nakamachi *et al.* 1999b, propose a very nice simplification of the simulations presented in section 5.3.1. A macroscopic mesh is defined to model the investigated process (Limiting Dome Height test, see Figure 1-1, cup deep drawing, see Figure 1-2). For instance in Nakamachi & Dong 1997, the quarter of the 180 x 100 mm blank used in the NUMISHEET'96 LDH benchmark test (Lee *et al.* 1996) is simulated by 1125 eight-node SRI (Selected Reduced Integration) solid elements. At every macroscopic interpolation point, the behavior law of a single crystal characterized by its orientation and the hardening state of each of its slip system is adopted. This approach is in fact a macroscopic extension of the microscopic FEM computation described in section 5.2. It can be considered as an inhomogeneous material modeling and it appears as the limit ($N=1$) of the models presented in section 5.3. In the macroscopic examples (LDH test, cup deep drawing) described in Nakamachi & Dong 1997, Nakamachi *et al.* 1999, Nakamachi *et al.* 1999b, no grain size effect is considered. However, the same approach applied on small scale simulations (rectangular sheet of 0.1mm x 0.3 mm in Nakamachi *et al.* 1999) allows to study grain size effect like in section 5.2.2.

A dynamic explicit finite element code is used with an elastic/crystalline viscoplastic constitutive law. Details on the crystalline viscoplasticity model are given hereafter. No special assumption as Taylor's, self-consistent or homogenization is needed as one single crystal orientation is given per macroscopic integration point. The strain heterogeneity between interpolation points directly follows from the nodal displacements. The equilibrium is assumed but not checked since an explicit finite element scheme is used.

Representative crystals orientation

The initial crystal orientation assigned to each interpolation point is randomly selected from a crystal population chosen to be representative of the measured ODF (Nakamachi & Dong 1997).

Behavior model of each crystal

The elastic/crystalline viscoplastic constitutive law is detailed in Nakamachi *et al.* 1999. Here, only the evolution of the CRSS associated with the slip system s is presented. Relation (5-32) takes into account the hardening process between slip systems as already done by relation (4-16) but it adds a softening aspect:

$$\dot{\tau}^s = \sum_{u=1}^{N} (h^{su} - s^{su}) \left| \dot{\gamma}^u \right| \tag{5-32}$$

The hardening coefficient matrix h^{su} is related to the grain size, to the increase of dislocation density, to the shear slip and to the interaction matrix between self and latent hardening:

$$h^{su} = \left\{ h_1 - h_2 \ tanh(\frac{D}{h_3}) \right\} n \left\{ C(\gamma_0 + \gamma) \right\}^{n-1} q^{su} \tag{5-33}$$

where
- h_1, h_2, h_3 parameters related to the grain size D,
- n, C parameters related to the increase of dislocation density,
- γ_0 initial shear slip,
- q^{su} interaction matrix of self and latent hardening.

The softening coefficient matrix s^{su} is related to the grain size, to the decrease of dislocation density, to the shear slip, to the CRSS level and to the cross slip:

$$s^{su} = \left\{ s_1 + s_2 \ tanh\left(\frac{D}{s_3} \right) \right\} \left(\frac{1}{1 + r / r_0} \right) s_0 \tau_c^s \tau^u \ p^{su} \tag{5-34}$$

with
- $s_1\ s_2\ s_3$ parameters related to the grain size D,
- r actual distance between the adjacent slip systems,
- r_o initial distance between the adjacent slip systems,
- s_0 parameters related to the decrease of dislocation density due to glide work, and thermomechanical effect,
- p^{su} parameter of dynamic recovery due to cross slip.

Conclusion

From Nakamachi's oral presentation at NUMISHEET 1999, it is known that his model has been applied with success to the simulations of cup deep drawing. However, in the written version, Nakamachi *et al.* 1999 only present the theory but not yet the Numisheet 99 benchmark applications.

The interest of such an approach is the decrease in computation time and variables storage as a set of representative crystals per integration point is replaced by a single crystal. Each integration point behaves like a single crystal characterized by a

different orientation; the material response must therefore be quite heterogeneous and it is not sure that an implicit FEM approach would converge. However, this approach gives a possible direct application of the micro-macro approach.

5.5. FEM analysis applied on both ODF evolution and macroscopic process

The discrete set of representative crystals used in FEM simulations as described in section 5.2 suffers from shortcomings because the characterization comes with few analytical tools. No direct means are available, for instance, to develop quantitative measures to differentiate between textures associated with distinct discrete aggregates. As a result, considerations on differences between textures are often qualitative, or obtained through projections onto alternate representations. In dealing with spatially inhomogeneous textures, there is often a need to interpolate or to project across textures. This requirement appears when initializing from experiment, or computing spatial gradients of texture as measures of the inhomogeneity degree. Such measures are important when the considered material is initially inhomogeneous and when substantial inhomogeneities develop over the course of the process. In rolling, for instance, highly localized regions of inhomogeneity develop through the thickness of the sheet due to roll induced shearing.

Kumar & Dawson 1995a, 1995b and 1996 and Dawson & Kumar 1997 propose a quite complex approach that uses directly the ODF without relying on discrete sets of representative crystals. This approach offers the advantage of an easier and more accurate possibility to compare and interpolate textures. 2 FEM simulations applied in different spaces are connected to each other :

- **in the crystal orientation space**, a finite element mesh describes the ODF representing the material; a microscopic finite element analysis is used to solve the ODF conservation equation presented in section 5.5.3;
- **in the classical geometrical space**, a spatial steady state simulation using Eulerian finite elements is applied to an industrial process such as rolling for instance.

It is fundamentally different from the approach proposed in section 5.3.3 which consists of 2 coupled FEM simulations in the classical geometrical space but performed on different scales: microscopic and macroscopic.

Of course, in Kumar and Dawson's work, both FEM simulations are coupled:

- the microscopic FEM requires the strain evolution to compute texture evolution;
- the macroscopic FEM uses the up-dated texture as well as crystal plasticity with Taylor's or Sachs' assumption to get the macroscopic constitutive behavior.

5.5.1. Crystal orientation representation

The crystal orientation is defined as the rotation $\underline{R}$ required to align the crystal lattice frame with a fixed sample reference frame. Three independent parameters are sufficient to describe such a rotation. Euler's angles are a frequent choice (see section 3.2, Figure 3-4). An alternative class of representation uses an axis of rotation $\underline{n}$ and an angle of rotation ϕ. In this case :

$$\underline{R}(\underline{n},\phi)=\underline{n}\otimes\underline{n}+(\underline{I}-\underline{n}\otimes\underline{n})\cos\phi+\underline{I}\wedge\underline{n}\sin\phi \qquad (5\text{-}35)$$

where $\underline{I}$ is the second order unit tensor. A particular representation of the crystal orientation is defined by Rodrigues' parameters which are the components r^1, r^2, r^3 of vector $\underline{r}$:

$$\underline{r}=\underline{n}\,tg\phi \qquad (5\text{-}36)$$

The parameters r^1, r^2, r^3 define the so-called Rodrigues' space.

The advantages of this choice are the following ones :

- A simple *fundamental region* can be computed in the orientation parameters space. Rodrigues' proposal defines all the possible crystal orientations without redundancy due to crystal symmetry. For instance, the case of f.c.c crystal leads to the fundamental region represented on Figure 5-15.

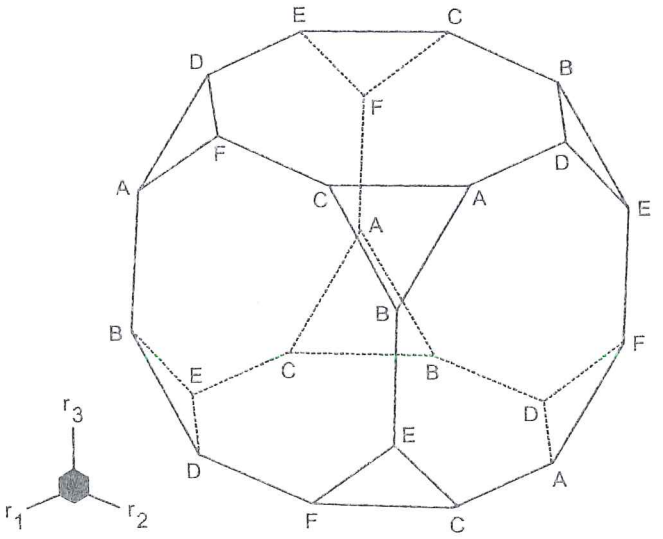

Figure 5-15 f.c.c fundamental region for Rodrigues'space (from Kumar & Dawson 1995).

- The space distortion is limited and there is no singularity in this space. This can be deduced from the form of the invariant volume element:

$$dv=\cos^2\left(\frac{\phi}{4}\right)dr^1dr^2dr^3 \qquad (5\text{-}37)$$

The quantity $cos^2 \frac{\phi}{4}$ is plotted in Figure 5-16 versus the angle ϕ, the range of which increases as the crystal degree of symmetry decreases from cubic to orthorhombic lattice.

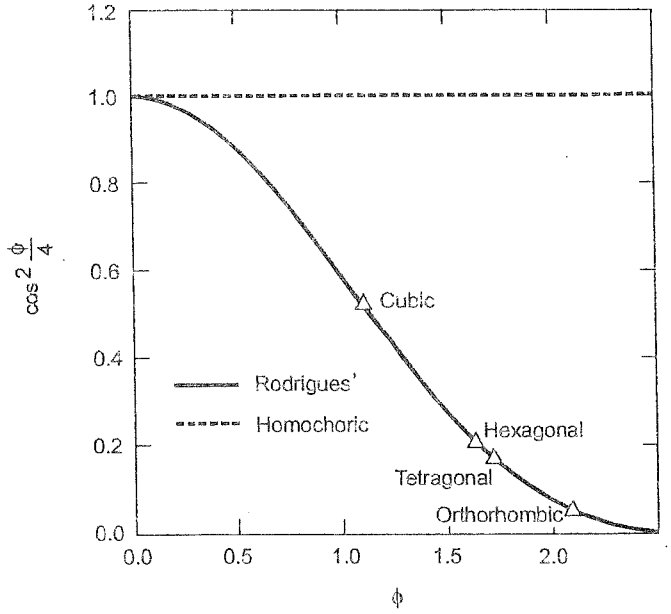

Figure 5-16 Volumetric scaling factor for Rodrigues' parameters (from Kumar & Dawson 1995).

With this parametrization, the *Orientation Distribution Function (ODF)* is defined by the *probability density* $f(\underline{r})$. The volume fraction V^* of crystals whose orientations belong to a subset Ω^* of the orientation space is given by:

$$V^* = \int_{\Omega^*} f(\underline{r})\, d\Omega \tag{5-38}$$

The whole domain Ω of orientation space depends on symmetries exhibited by the crystal. $f(\underline{r})$ is scaled in such a way that:

$$1 = \int_{\Omega} f(\underline{r})\, d\Omega \tag{5-39}$$

5.5.2. Micro-macro links

The macroscopic behavior is the average of the behavior of the individual crystallites of the aggregate. If x^{micro} is an arbitrary crystal quantity, its macroscopic value x^{macro} is given by:

$$x^{macro} = \int_{\Omega} x^{micro}(\underline{r})\, f(\underline{r})\, d\Omega \tag{5-40}$$

Here is a difference with respect to approaches using a discrete sample of orientations and simply computing a weighted average of the crystal quantities (see relations (5-18) and (5-19)). Dawson and Kumar apply a visco-plastic constitutive law at the crystal level as proposed in section 4.2., with identical rate sensitivity and CRSS for all slip systems and for all the crystallites related to one interpolation point. Coupling this crystal behavior law with the crystal velocity gradient (4-2) and the definition of the resolved shear stress (3-2), an invertible relationship between the crystal deformation rate and the deviatoric stress in this crystallite is obtained:

$$\hat{\underline{\sigma}}^{micro} = \underline{\underline{D}}^{micro} : \underline{\dot{\varepsilon}}^{micro} \tag{5-41}$$

where $\underline{\underline{D}}^{micro}$ is the microscopic stiffness. Then, either Taylor's assumption of equality between micro and macro plastic strain rates or the assumption of micro and macro stress equality (Prantil *et al.* 1995) is applied. Both assumptions allow to reach $\underline{\underline{D}}^{micro}$ and its average value, computed by (5-40). This gives upper and lower bounds to macroscopic stiffness.

5.5.3. Evolution rule of the Orientation Distribution Function

Restricting his attention to the lattice reorientation caused by crystallographic slips, Clement 1982 proposes to model texture evolution by integrating an equation for the rate of change of the probability density $f(\underline{r},t)$. This equation results from requiring that the material derivative of relation (5-39) vanishes.

$$\frac{\partial f}{\partial t} + \underline{v}.grad\ f + f\ div\ \underline{v} = 0 \tag{5-42}$$

where $\underline{v}$ is the reorientation velocity. Note that Arminjon 1988 provides a demonstration of this type of equation using physical hypotheses. The above formulation is an Eulerian representation in which f is associated to particular locations in the orientation space, rather than to particular crystals whose orientations change. Alternatively, a reference texture f_0 can be specified, for instance f at time t_0. Then, this reference position remains fixed for all times and is used to define initial Lagrangian coordinates for crystals. Relation (5-42) can be written either with respect to current Eulerian coordinates $f(\underline{r},t)$ or with respect to the Lagrangian coordinates $\hat{f}(\underline{r}_0,t)$. The two representations are related through the mapping of coordinates from reference to current configurations:

$$f(\underline{r},t) = \hat{f}(\underline{r}_0,t) \tag{5-43}$$

and

$$\hat{f}(\underline{r}_0,t)\ J(\underline{r}_0,t) = f_0(\underline{r}_0) \tag{5-44}$$

where $J(\underline{r}_0,t)$ is the determinant of the mapping, which corresponds to the trajectories of crystals in the orientation space due to plastic deformation:

$$\underline{r}(t) = \hat{\underline{r}}(\underline{r}_0, t) \tag{5-45}$$

In Lagrangian representation, relation (5-42) becomes:

$$\frac{\partial f}{\partial t} + \hat{f}\ div\, \hat{\underline{v}} = 0 \quad \text{where } \hat{\underline{v}}(\underline{r}_0, t) = \underline{v}(\underline{r}, t) \tag{5-46}$$

Euler's choice (5-42) leads to difficulties in the FEM formulation because of the convective contribution associated with the term $\underline{v}.grad\ f$. This still remains a problem, even if some solutions are proposed in computational fluid mechanics. The alternative is to use the Lagrangian representation (5-46). However, this adds the cost of an explicit computation of crystal trajectories in the orientation space. Both approaches are described in Kumar & Dawson 1996.

Another difficulty is the extreme behavior of the ODF. The ODF can evolve exponentially, sometimes tending asymptotically to Dirac's function. Clearly, inaccuracies are inevitable as the finite element size cannot tend to 0. An effective strategy applied by Kumar and Dawson is to moderate the evolution of the ODF by the following transformation :

$$p = ln\, f \tag{5-47}$$

5.5.4. Computation of the reorientation velocity field

Relations (5-42) and (5-46) to compute the new ODF make use of the reorientation velocity field $\underline{v}$, which is linked to crystal plasticity and to the relationship between the crystal velocity gradient and its macroscopic counterpart. As explained in section 4.1.1 related to single crystal plasticity, the rate of crystal lattice rotation $\underline{\Omega}^L$ can be expressed by (4-12):

$$\underline{\Omega}^L = \underline{\Omega}^{micro} - \sum_s \underline{Z}^s \dot{\gamma}^s \tag{5-48}$$

where the first term on the right side of (5-48) is directly given by the macroscopic spin if Taylor's assumption is chosen. The second term is the spin due to the slip rates on the different slip systems.

The relationship between $\underline{\Omega}^L$ and $\underline{v}$ depends on the specific parametrization employed for rotations. For Rodrigues' parameters, Kumar & Dawson 1995a or Dawson & Kumar 1997 establish:

$$\underline{v} = \frac{1}{2}(\underline{\Omega}^{Lv} + (\underline{\Omega}^{Lv}.\underline{r})\underline{r} + \underline{\Omega}^{Lv} \wedge \underline{r}) \tag{5-49}$$

where $\underline{\Omega}^{Lv}$ is a vector form of the rate of crystal lattice rotation $\underline{\Omega}^L$.

5.5.5. Texture prediction under monotonic deformations

The following example shows a FEM analysis applied to solve the texture conservation relation under the assumption of plane strain compression of f.c.c polycrystals. In Figure 5-17, the 3D FEM mesh of 28672 - 4 nodes tetrahedral elements is showed.

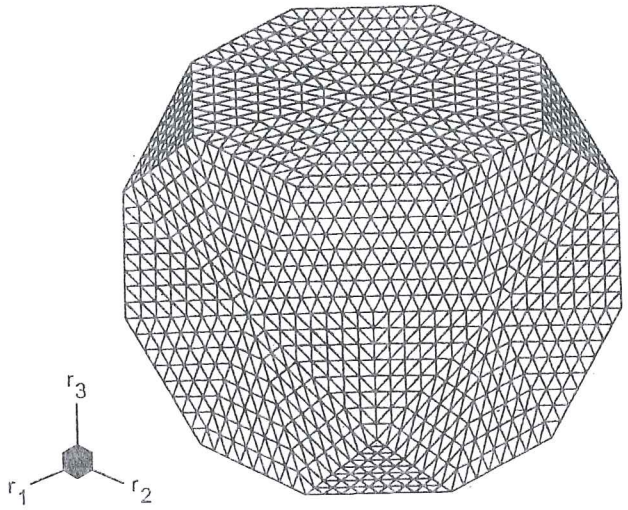

Figure 5-17 FEM mesh used for f.c.c fundamental region (from Kumar & Dawson 1995b).

As Taylor's hypothesis is applied, the reorientation velocity, developed under a monotonic deformation, is invariant with strain. So crystal computations are done only once. The developed texture is adequately represented by the ODF on the boundaries of the fundamental region; consequently only outside views of the ODF are represented. The ideal components of f.c.c plane strain compression texture are compared with the computed results on Figure 5-18.

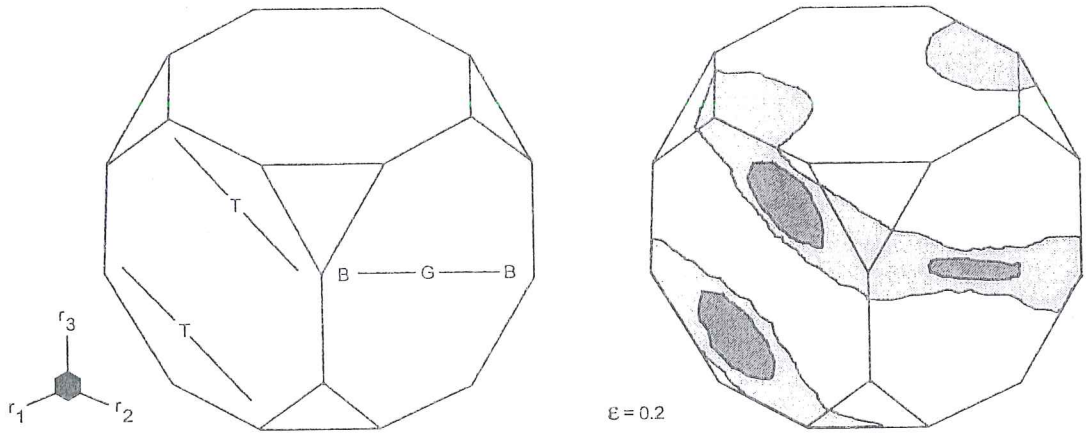

Figure 5-18 Ideal (a) and computed (b) components of plane strain compression texture of an f.c.c polycrystal (from Kumar & Dawson 1995b).

Texture development is dominated by two fibers:
- an α fiber connecting the ideal Goss and Brass' orientations;
- the β fiber connecting Brass and Taylor's orientations.

5.5.6. Application to aluminum rolling

The flat rolling of a 1100 aluminum (Figure 5-19) being a steady state process, a macroscopic Eulerian FEM approach is applied to model the macroscopic mechanical problem (Figure 5-20).

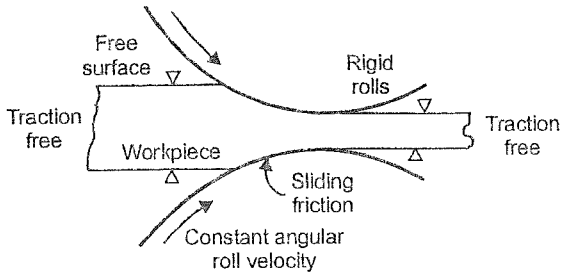

Figure 5-19 Schematic diagram of flat rolling (from Dawson & Kumar 1997).

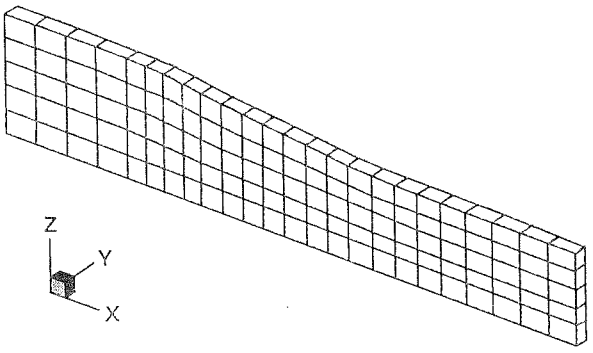

Figure 5-20 Finite element discretization of the workpiece (from Dawson & Kumar 1997).

In fact, the FEM analysis of texture evolution is coupled with the macroscopic FEM computation. Two FEM scales are present and the details on their parallel implementation can be found in Kumar & Dawson 1995b. Figure 5-21 shows the equivalent plastic deformation rate, the reference CRSS and the scalar measure of the spatial gradients of the ODF defined by :

$$\nabla A = \int_{\Omega} \left| grad\ f(\underline{r},\underline{x}) \right| d\Omega \qquad (5\text{-}50)$$

where $\underline{x}$ identifies a material point of the workpiece.

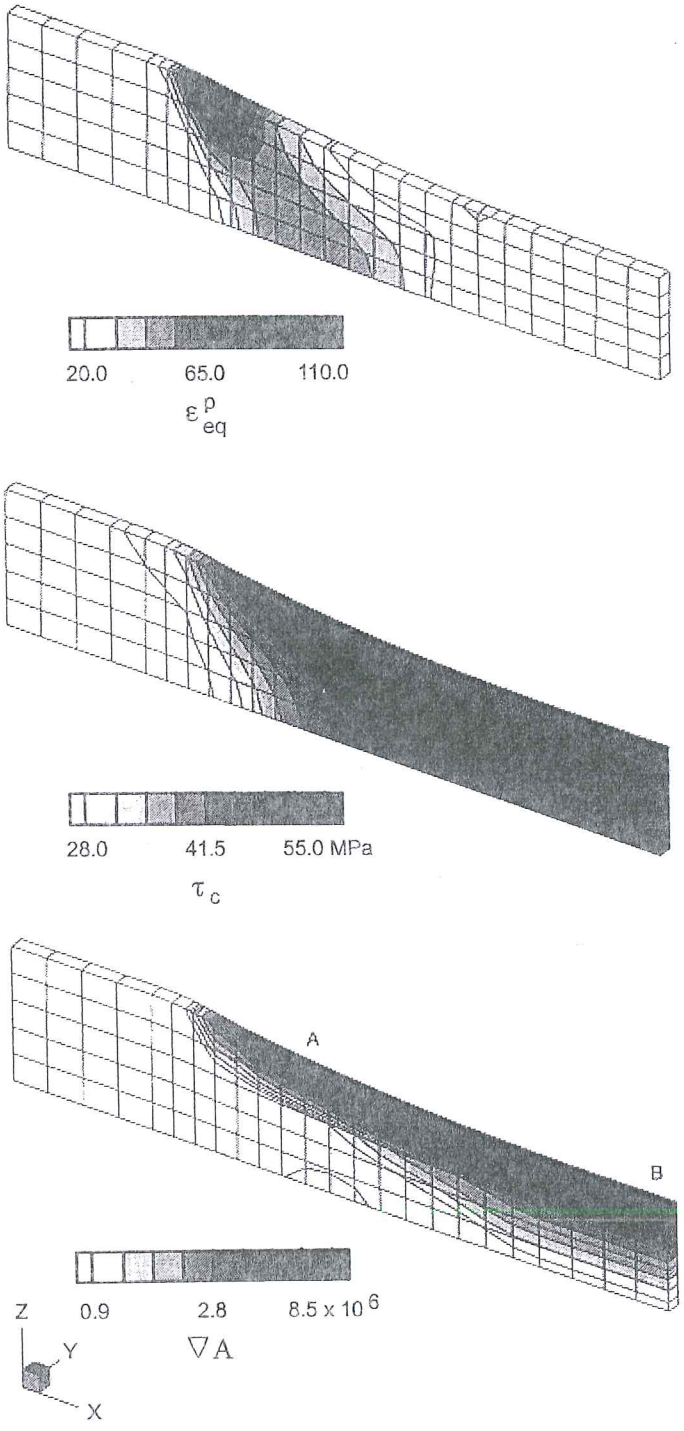

Figure 5-21 Contour plots of the equivalent plastic deformation rate ε^{p}_{eq},
the reference CRSS τ_c,
a scalar measure of the spatial gradients of the ODF ΔA,
(from Kumar & Dawson 1995).

As expected, the microstructure hardens primarily within the deformation zone under the roll. Hardening and texture gradients appear through the workpiece thickness. It is observed that the texture gradients are rather important.

5.5.7. Conclusion

This approach developed by Kumar and Dawson is interesting from a scientific point of view. It shows another proposal for the micro-macro coupling, not limited to the mechanical point of view. Here the FEM formulation is directly applied for texture prediction and, hence, provides metallurgical information. However, the amount of computations seems to be even greater than in section 5.2 since the mesh discretization of the texture problem is already of large size.

5.6. Conclusion

Section 5.1 demonstrates the interest of FEM microscopic simulations to check the microscopic models and to investigate the effect of microscopic parameters such as the influence of grain sizes on the macroscopic mechanical behavior.

Clearly, with parallel computers, the above selection of scientific works (sections 5.3., 5.4. and 5.5) shows that micro-macro approaches attract a great interest and become closer to practical problems. However, for each type of applications, it appears that more efforts should be devoted estimating the size of the set of representative crystals or the RVE or the texture discretization. This is directly linked to the accuracy of the results and to the CPU time.

From this review, it appears that a visco-plastic formulation is very often used at the crystal level with the advantage of avoiding the choice between the multiple solutions of Taylor's model. However, at room temperature, the strain rate sensitivity coefficient is very low, which leads to numerical difficulties and explains the further research dedicated to the strain rate independent approach (Anand & Kothari 1996, Miehe *et al.* 1999). Finally both models can be chosen according to their availability.

The use of a common CRSS evolution rule (5-20) for all the slip systems in a crystal or even for all crystallites in a polycrystal at an integration point, seems a logical simplification to limit the number of state variables. However, a clear information on the accuracy benefit of choosing a distinct CRSS for each slip system seems unavailable.

The effect of the micro-macro links which have been used (FC or RC or modified Taylor's model, self-consistent model, homogenization method) has been the most studied problem. The choice clearly depends on the number of available slip systems, the desired accuracy and the CPU requirements. For b.c.c or f.c.c materials, Taylor's model already seems to give interesting results from a mechanical point of view

(stress, strain) but it also gives qualitative texture prediction with the lowest CPU time.

The simple approach proposed by Nakamachi 1999b offers a solution to reduce the CPU time of micro-macro approaches. However further results comparison with an implicit micro-macro FEM approach should be performed.

References

Acharya, A., Bassani, J.L. (2000) Lattice incompatibility and a gradient theory of crystal plasticity, *J. Mech. Phys. Solids*, **48/8**, 1565-1595.

Acharya, A., Beaudoin, A.J. (2000) Grain-size effect in viscoplastic polycrystals at moderate strains, *J. Mech. Phys. Solids*, **48/10**, 2213-2229.

Anand, L., Kothari, M. (1996) A Computational Procedure for Rate-Independent crystal plasticity, *J. Mech. Phys. Solids*, **44/4**, 525-558.

Anand, L., Balasubramanian S., Kothari, M. (1997) Constitutive Modeling of Polycrystalline Metals at Large Strains : Application to Deformation Processing, *Large plastic deformation of crystalline aggregates*, International Centre for Mechanical Sciences, Courses and Lectures n° 376, Springer Ed, 109-172.

Arminjon, M. (1988) Lois de comportement homogénéisées pour la plasticité des polycristaux, Mém. d'habilitation, Univ. Paris-Nord, Villetaneuse.

Asaro, R.J., Needleman, A. (1985) Texture development and strain hardening in rate dependent polycrystals, *Acta Metallurgica*, **33**, 923-953.

Beaudoin, A.J., Dawson, P.R., Mathur, K.K., Kocks, U.F., Korzekwa, D.A. (1994) Application of polycrystal plasticity to sheet forming, *Comp. Methods Appl. Mech. Eng.*, **117**, 49-70.

Beaudoin, A.J., Dawson, P.R., Mathur, K.K., Kocks, U.F. (1995) A hybrid finite element formulation for polycrystal plasticity with consideration of macrostructural and microstructural linking, *Int. J. Plasticity*, **11/5**, 501-521.

Becker (1990) An analysis of shear localization during bending of a polycrystalline sheet, *Microstructural Evolution in Metal Processing*, **46**.

Bertram, A., Böhlke, T., Kraska, M. (1997) Numerical simulation of texture development of polycrystals undergoing large plastic deformations, *Computational Plasticity*, Fundamentals and Applications, Owen D.R.J., Onate, E., Hinton E. Eds.

Canova, G.R., Lebensohn, R. (1995) Micro-macro modelling, *Computer Simulation in Materials Science, NATO ASI,* Ile d'Oleron, France, June 6-16.

Chastel, Y., Loge, R., Perrin, M., Lamy, V. & Zaefferer, S. (1998) Microscopic and macroscopic length scales in hot extrusion of Zircaloy 4, *First ESAFORM Conference on Material Forming,* Sophia-Antipolis, France.

Clément, A. (1982) Prediction of Deformation Texture Using a Physical Principle of Conservation. *Mater. Sci.&Eng.*, **55**, 203-210.

Dawson, P.R., Beaudoin, A.J., Mathur, K.K. (1992) Simulating deformation-induced texture in metal forming, *Num. Meth. in Ind. Form. Proc.*

Dawson, P.R. & Kumar, A. (1997) Deformation Process Simulations Using Polycrystal Plasticity, *Large plastic deformation of crystalline aggregates*, International Centre for Mechanical Sciences, Courses and Lectures n° 376, Springer Ed, 247.

Feyel; F., Chaboche, J.L. (2000) Mutiscale non linear FE analysis of composite structures : damage and fiber size effets, *Euromech 417*, 2-4 October 2000, University of Technology of Troyes, France.

François, D., Oineau, A. Zaoui, A (1992) Elasticité et Plasticité, Hermes, Paris.

Geers, M.G.D., Kouznetsova, V., Brekelmans, W.A.M. (2000) Constitutive approaches for the multi-level analysis of the mechanics of microstructures, 5th National Congress on Theoretical and Applied Mechanics, Louvain-La-Neuve, May 23-24, 2000.

Hacquin A., Montmitonnet, P., Guillerault J.P. (1995) Coupling of roll and strip deformation in three-dimensional simulation of hot rolling, *Simulation of Materials Processing : Theory, Methods and Applications*, 921.

Kalidindi, S.R., Bronkhorst, C.A., Anand, L. (1992) Crystallographic texture evolution during bulk deformation processing of FCC metals, *J. Mech. Phys. Solids*, **40**, 537-579.

Kalidindi, S.R., Anand, L. (1994) Macroscopic shape change and evolution of crystallographic texture in pre-textured FCC metals, *J. Mech. Phys. Solids*, **42/3**, 459-490.

Kallend, J.S., Kocks, U.F., Rollett, A.D., Wenk, H.R. (1991) popLA – an integrated software system for texture analysis. *Text. microstruct.*, **14-18**, 1203-1208.

Kumar, A., Dawson, P.R. (1995a) The simulation of texture evolution during bulk deformation processes using finite elements over orientation space, *Simulation of Materials Processing : Theory, Methods and Applications*, Shen & Dawson Eds., Balkema.

Kumar, A., Dawson, P.R. (1995b) Polycrystal plasticity modeling of bulk forming with finite elements over orientation space, *Comp. Mech.*, **17**, 10-25.

Kumar, A., Dawson, P.R. (1996) The simulation of texture evolution with finite elements over orientation space, I. Development, II. Application to planar crystals, *Comp. Methods Appl. Mech. Eng.*, **130**, 227-261.

Lebensohn, R.A., Tome, C.N. (1993) A self-consistant anisotropic approach for the simulation of plastic deformation and texture development of polycrystals : application to Zirconium alloys, *Acta Metall. Mater.*, **41**, 2611-2624.

Lee, J.K., Kinzel, G.L., Wagoner, R.H. (1996) Numerical Simulation of 3-D Sheet Metal Forming Processes - Verification of Simulations with Experiments, *Proceedings of the 3rd International Conference NUMISHEET'96*, Dearborn, USA, September 29-October 3, 1996.

Mathur, K.K., Dawson, P.R. (1989) On modeling the development crystallographic texture in bulk forming processes, *Int. J. Plasticity*, **5**, 67-94.

Miehe C., Schröder J., Schotte J. (1999) Computational homogenization analysis in finite plasticity, simulation of texture development in polycrystalline materials, *Computer methods in applied mechanics and engineering*, **171**, 387-418.

Molinari, A. (1997) Deformation Process Simulations Using Polycrystal Plasticity, *Large plastic deformation of crystalline aggregates*, International Centre for Mechanical Sciences, Courses and Lectures n° 376, Springer Ed, 173-246.

Nakamachi, E., Dong, X.H. (1997) Study of Texture Effect on Sheet Failure in a Limit Dome Height Test by Using Elastic/Crystalline Viscoplastic Finite Element Analysis, *J. Appl. Mech. Trans. ASME(E)*, **64**, 519-524.

Nakamachi, E., Onate, E., Bergan, P., Boduroglu, M.H., Kaykayoglu, C.R. (1999a) The study of crystalline morphology effects on sheet metal forming, IACM Expressions, **7**, Spring-Summer 1999.

Nakamachi, E., Xie C.L., Hiraiwa, K., Harimoto, M. (1999b) Development of elastic/crystalline viscoplastic finite element analysis code based on the meso-phenomenological material modeling, Numisheet'99, 13-17 September 1999, vol. 1, Besançon, France, 79-84.

Nikolov, S., Doghri, I. (2000) A micro-macro constitutive model for the small deformation behavior of polyethylene, *Polymer*, **41**, 1883-1891.

Neale, K.W. (1993) Use of Crystal Plasticity in Metal Forming Simulations, *Int. J. Mech. Sci.*, **35/12**, 1053-1063.

Prantil, V., Dawson, P., Chastel, Y. (1995) Comparison of equilibrium based plasticity models and a Taylor like hybrid formulation for deformations of constrained crystal systems, *Modeling Simul. Mater. Sci. Eng.* **3**, 215-234.

Smit, R.J.M., Brekelmans, W.A.M., Meijer, H.E.H. (1998) Prediction of the mechanical behavior of nonlinear heterogeneous systems by multi-level finite element modeling, *Comp. Meth. Appl. Mech. Eng.*, **155**, 181-192.

Teodosiu, C., Raphanel, J.L., Tabourot, L. (1992) Finite Element Simulation of the Large Elastoplastic Deformation of Multicrystals, *Large Plastic Deformations. Fundamentals and Applications to Metal Forming (Proc. MECAMAT'91)*, Teodosiu C., Sidoroff F., Raphanel, J.L. Eds, Balkema, Rotterdam, 153-168.

6. FEM MICRO-MACRO MODELS WITH YIELD LOCUS

6.1. Introduction

In the preceding chapter, the drawback of high CPU time to compute the state of representative crystals, then to reach, by an averaging operation, the macroscopic behavior has often been mentioned. Scientists have investigated other micro-macro approaches that are less greedy from a CPU time point of view.

A first option is to develop new macroscopic elasto-plastic or elasto-visco-plastic models with general features imbued from plasticity models in single crystals. Such approaches are described in section 6.2.

Another option is presented in section 6.3. In this case, outside any FEM code, models at crystal level and micro-macro links are applied to estimate an accurate expression of the yield locus in polycrystal materials. Then, this accurate yield locus function is used during macroscopic FEM computations. The evolution of the size and position of this yield locus during the process is defined by macroscopic isotropic and kinematic hardening rules. As explained in chapter 3, such hardening models can be macroscopic but with strong links to microscopic phenomena. Even if their accuracy can be quite high (see Teodosiu & Hu 1998 and Miller & Mc Dowel 1996), such models generally neglect the "texture hardening", i.e. the fact that due to texture evolution, the yield locus shape should be updated. In some cases, this phenomenon is really negligible and using an accurate description of the initial yield locus conjugated with elaborate hardening models yields a very good accuracy at low CPU cost. The time reduction of such approaches as compared to FEM codes directly coupled with microscopic calculations (see section 5.3) is difficult to estimate. However we do not speak of a ratio of 2 or 3 but rather 10, 100 and even greater, if no parallel computation is applied.

About the memory requirement, such approaches spare all the variables needed at every interpolation point to store the orientation and the average CRSS (or even the CRSS associated to each slip system) of each crystal of the representative set. This explains why, even if some yield locus description and their hardening behavior need 100 or more constants and 50 internal variables, they are still much more economical than the micro-macro approaches presented in chapter 5.

Of course these FEM models predict only the mechanical behavior. If the texture evolution is an interesting result, the strain history during the process must be stored and used in post-processor modules to predict the final texture. Such an approach is proposed by Winters 1996, who simulates a cup drawing with the LAGAMINE code using the yield locus described in section 6.3.4. Then he uses the strain history to

predict the texture evolution and compares it to texture measurements. His simulation results are quite accurate. Another example is the work by Schoenfeld & Asaro 1996. They study the texture gradients through thickness in rolled polycrystalline alloys by means of FEM rolling simulations using a phenomenological constitutive law. Once the displacement time history of the roll gap has been calculated, Taylor's model is applied at locations of interest through the thickness of the workpiece to predict the final texture and material anisotropy.

Finally, section 6.4 describes the model developed by MSM department. It stands between the models of section 5.3 and the accurate yield locus functions deduced from texture (section 6.3). As the aim is to model the effect of texture updating on the shape of the yield locus, a function accurately describing the whole yield locus and adjusted from computations on a set of representative crystals would be too expensive to fit each time the texture needs to be updated. A function limited to a "small local zone" of the yield locus has been chosen and the position of this zone is adapted according to the stress or strain rate state of each integration point. The identification of this function requires a limited number of calls to Taylor's model applied on a set of representative crystals. As for memory storage, this approach is equivalent to FEM models coupled with microscopic computations, described in section 5.3. However, concerning the constitutive law, generally no call to microscopic computations is needed. Some calls exist if it appears that the local zone of the yield locus does not fit with the new material state. After a few increments or time steps, texture updating is taken into account by using a Taylor's model to compute the new orientations of the set of representative crystals and to update the local zone of the yield locus. Details and examples are given in sections 6.4. and 6.5.

Such analysis where some microscopic computations still appear in the FEM code, is slower than the totally decoupled approaches described in section 6.3. Its interest is to take into account the texture updating effect on the yield locus, without the microscopic computations necessary to compute a complete updated yield locus.

6.2. Macroscopic models imbued from single crystal plasticity

6.2.1. *3G* Model

The "Centre de Recherches Métallurgiques" of Liège has developed the so-called "*3G* model" (Monfort *et al.* 1991, Montfort & Defourny 1993, Montfort & Defourny 1994). It is a non-associated visco-plastic model. The planar isotropic version has been studied and validated in the Ph.D. by Hage Chehade 1990, before the proposal of an orthotropic version by Montfort & Defourny 1993.

To understand this approach, first consider the plane stress state in a planar isotropic material as described on Figure 6-1.

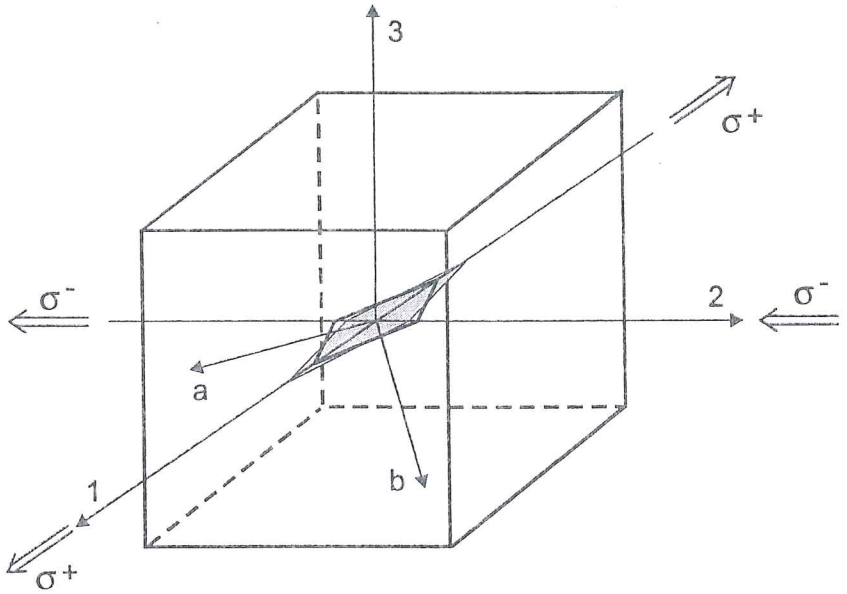

Figure 6-1 Plane stress state resulting in a pure shear state in axes *a, b*, rotated by 45° from the principal stress axes 1,2 (adapted from Hage Chehade 1990).

The strain tensor associated to this loading state is defined by (6-1) where G_{12} is associated to the shear stress τ_{12} applied on the planes oriented at 45° from directions 1 and 2.

$$\underline{\varepsilon}^p = \begin{pmatrix} G_{12} & 0 & 0 \\ 0 & -G_{12} & 0 \\ 0 & 0 & 0 \end{pmatrix}_{ref\ axes\ 1,2,3} \qquad \underline{\varepsilon}^p = \begin{pmatrix} 0 & G_{12} & 0 \\ G_{12} & 0 & 0 \\ 0 & 0 & 0 \end{pmatrix}_{ref\ axes\ a,b,3} \tag{6-1}$$

The extension of this simple state to general cases assumes that plastic strains happen by plastic slips on planes oriented at 45° from principal axes and along directions where shear stresses are maximal. As in b.c.c metals, 24 families of slip planes exist, one can assume that there is always a crystallographic plane oriented nearly along a direction of maximum shear stress. This generalisation is represented by Figure 6-2 and by relation (6-2) where axes λ, μ, ν are not orthogonal axes.

The plastic strain tensor is expressed by:

$$\underline{\varepsilon}^p = \begin{pmatrix} 0 & G_{12} & G_{13} \\ G_{12} & 0 & G_{32} \\ G_{13} & G_{32} & 0 \end{pmatrix}_{ref\ axes\ \lambda,\mu,\nu} \tag{6-2}$$

where the 3 G shear strains, responsible for the model name, appear.

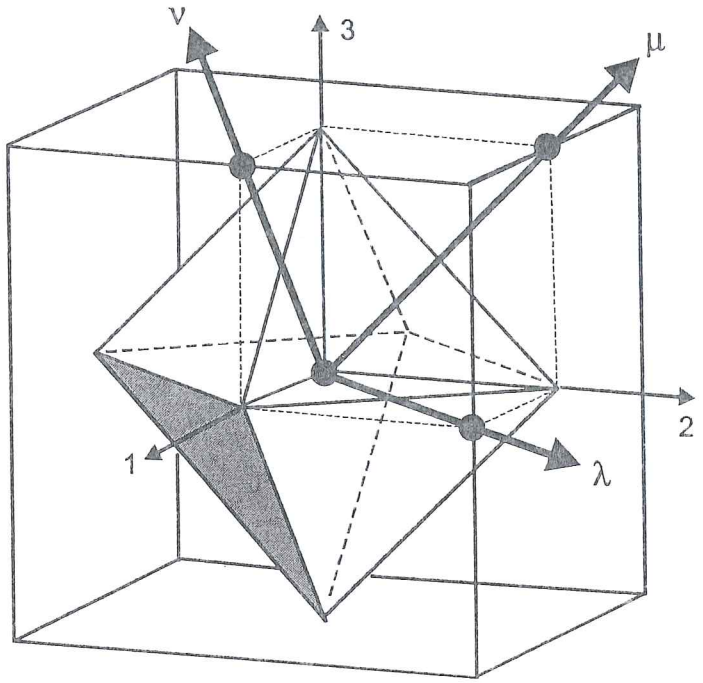

Figure 6-2 General view of assumed slip planes in general cases (adapted from Hage Chehade 1990).

For simplicity, relation (6-2) is written in principal axes *1,2,3*:

$$\underline{\varepsilon}^{p} = \begin{pmatrix} \varepsilon_{11} & 0 & 0 \\ 0 & \varepsilon_{22} & 0 \\ 0 & 0 & \varepsilon_{33} \end{pmatrix} = \begin{pmatrix} G_{12}-G_{13} & 0 & 0 \\ 0 & G_{23}-G_{12} & 0 \\ 0 & 0 & G_{31}-G_{23} \end{pmatrix}_{ref\ axes\ 1,\ 2,\ 3} \tag{6-3}$$

Shear stresses acting on octahedral planes are associated to the 3 G shear strains:

$$\tau_{12} \rightarrow G_{12},\ \tau_{23} \rightarrow G_{23},\ \tau_{13} \rightarrow G_{13} \tag{6-4}$$

With the previous concepts in mind, the isotropic planar version of the *3G* model applies to a thin sheet where the principal stress σ_3 in the thickness direction is low. It assumes that any plastic strain results from the superposition of plastic shears oriented at 45° from principal stresses directions as represented on Figure 6-3.

If the material presents a planar anisotropy, more crystals are oriented in specific directions for which a macroscopic deformation is easier or more difficult. In other words, the resistance to deformation varies with the direction in the sheet plane. Extending the isotropic planar approach, macroscopic strain occurs in families of planes presenting the most favourable ratio between the applied shear stress and the intrinsic resistance to deformation. In general, such planes are deviated from the 45°directions to principal stresses. The shift angle strongly depends on the Lankford coefficient. It can be mathematically determined as well as its incidence on the total deformation.

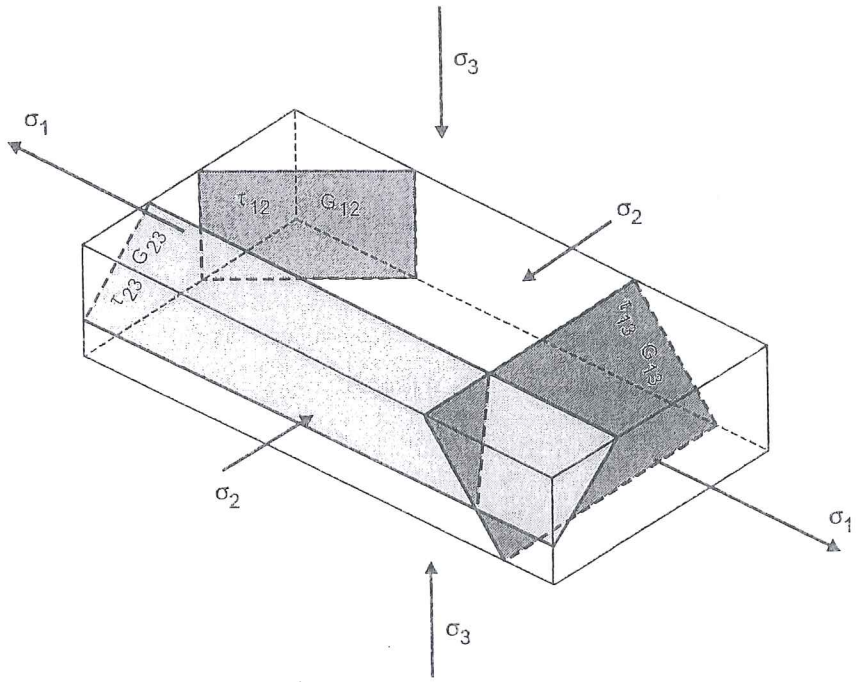

Figure 6-3 Sheet strains decomposed into plastic slips in planes oriented at 45° from principal stresses (from Hage Cheade, 1990).

As far as the hardening rule is concerned, the *3G* model applies a generalization of Bergström's model presented in section 3.5.1 (Bergström 1969). Using the 3 G as strain measures allows to extend Bergström's work on a more physical basis for any stress and strain state. It is demonstrated (Monfort & Defourny, 1994) that the plastic shear stress τ used in Tresca's theory can be related to the *3G* strain measures:

$$2\tau = A + B\left[1 - exp\left(-a\, r_{45+\beta}\left(|G_{12}| + r_{90+\beta}|G_{23}| + r_{\beta}|G_{31}|\right)\right)\right]^{1/2} \qquad (6\text{-}5)$$

where A,B and a are material constants, r_{α} is Lankford's coefficient for a direction at an angle α from the Rolling Direction, β is the angle between the first principal stress and the Rolling Direction and τ is the stress limit in Tresca's criterion, ($2\tau = \sigma_F$ is the yield stress in uniaxial tension test). For simplicity, Lankford's coefficient for any direction α is approximated by a simple function :

$$r_{\alpha} = C + D\sin^2\alpha + E\sin^2 2\alpha \qquad (6\text{-}6)$$

with 3 material constants C,D,E.

These constants can be determined from the values of r_o, r_{45} and r_{90}. As the *3G* model is based on stresses acting on the maximum shear planes, a Tresca-like criterion is used, which is consistent with the mechanism taken into account:

$$|\sigma_1 - \sigma_2| + |\sigma_2 - \sigma_3| + |\sigma_3 - \sigma_1| - 2\tau = 0 \qquad (6\text{-}7)$$

However the exact shape of the plasticity criterion is of secondary importance, since it only specifies the limiting stress level of plasticity initiation. The subsequent plastic behavior, in terms of stresses and strains is obviously more important with this non associated visco-plastic model. It is described by the flow rule presented hereafter. Returning to the physics, the evolution of the shear strain dG_{ij} is due to the creation and the propagation of mobile dislocations. It is proportional to:

- the time increment dt ;
- the rate of mobile dislocation creation[1], itself proportional to the total amount of immobile dislocations and to a thermal activation factor;
- the path free of mobile dislocations, which is assumed constant and equal to the average dimension of the dislocation cell as in Bergström's model;
- the inverse of Lankford's coefficient[2];
- the probability that a dislocation moves along a given shear plane, which is a function of the shear stresses.

Finally, the flow rules proposed by Monfort & Defourny, 1994 for the shear strains dG_{ij} are given hereafter:

$$dG_{12}^{1} = \frac{d\lambda(\sigma_1 - \sigma_2)\cos(2\alpha_1)}{2r_{(\beta-45-\sigma_1)}}$$

$$dG_{12}^{2} = \frac{d\lambda(\sigma_1 - \sigma_2)\cos(2\alpha_2)}{2r_{(\beta+45-\sigma_2)}}$$

$$dG_{23} = \frac{d\lambda(\sigma_2 - \sigma_3)}{r_1 r_{(90+\beta)}}$$

$$dG_{31} = \frac{d\lambda(\sigma_3 - \sigma_1)}{r_1 r_\beta} \qquad (6\text{-}8)$$

with : $$tg(2\alpha_1) = \frac{-D\cos(2\beta - 2\alpha_1) - 2E\sin(4\beta - 4\alpha_1)}{2C + D(1 - \sin(2\beta - 2\alpha_1)) + 2E\cos^2(2\beta - 2\alpha_1)}$$

$$tg(2\alpha_2) = \frac{D\cos(2\beta - 2\alpha_2) - 2E\sin(4\beta - 4\alpha_2)}{2C + D(1 + \sin(2\beta - 2\alpha_2)) + 2E\cos^2(2\beta - 2\alpha_2)} \qquad (6\text{-}9)$$

1 The rate of mobile dislocation creation is related to a potential function of stresses (Mecking & Lucke 1970).

2 The texture effect responsible for Lankford's coefficient value directly modifies the flow rule.

$$\frac{1}{r_1} = \frac{cos(2\alpha_1)cos(45-\alpha_1)cos(45+\alpha_1)}{2r_{(\beta-45-\sigma_1)}} + \frac{cos(2\alpha_2)cos(45-\alpha_2)cos(45+\alpha_2)}{2r_{(\beta+45-\sigma_2)}}$$

$$d\lambda = K.dt.s.\left[\frac{2\tau - A}{B}\right]^2 \frac{exp\left[\frac{|\sigma_1-\sigma_2|+|\sigma_2-\sigma_3|+|\sigma_3-\sigma_1|-4|\tau|}{W}\right]}{|\sigma_1-\sigma_2|+|\sigma_2-\sigma_3|+|\sigma_3-\sigma_1|}$$

where K : material constant,
s : average free path of dislocations,
W : viscosity constant,
α_1, α_2 : angles measuring the deviation of G_{12} gliding planes from the directions at 45° from the principal stresses (planar anisotropy effect).

Recall that all the computations are performed in the axes of principal stresses. For the orthotropic cases, the basic strain relations are:

$$d\varepsilon_{11} = dG^1_{12}\, cos(45-\alpha_1)cos(45+\alpha_1) + dG^2_{12}\, cos(45+\alpha_2)cos(45-\alpha_2) - dG_{31}$$

$$d\varepsilon_{22} = dG^1_{12}\, sin(45-\alpha_1)sin(45+\alpha_1) - dG^2_{12}\, sin(45+\alpha_2)sin(45-\alpha_2) + dG_{23}$$

$$d\varepsilon_{33} = dG_{31} - dG_{23}$$

$$d\varepsilon_{12} \cong \alpha_1 dG^1_{12} - \alpha_2 dG^2_{12} \qquad (6\text{-}10)$$

The parameter identification is well described in Monfort & Defourny 1994:

- the parameters A, B and a of the hardening rule (6-5) are determined by means of a uniaxial tensile test, a tensile test on a wide specimen test and an equiaxial stretching (bulge test);
- the parameters C,D,E defining Lankford's coefficient function are reached thanks to classical tensile tests in 3 directions;
- with s incorporated in K, the flow rule is defined by K and W constants. The parameter W can be considered as nearly constant for all steels ($W=16$ *Mpa*); the fitting of the K factor is more complicated: the interested scientist should read Monfort & Defourny 1994.

With its parameters related to fundamental physics, the *3G* model potentially has the ability to take into account the main macroscopic features of deformation under complex strain paths. For instance, pre-strain effect, or change in dislocation cell shapes and sizes can be handled with simple modifications. This advantage appears for any model based on Bergström's extension. The interesting feature of the *3G* model is to take directly into consideration changes in Lankford's coefficients; however their evolution is not provided in the present version of the model, so it neglects texture evolution effect.

Comparisons between simulation results and experiments, such as bulge test, hemispherical and cylindrical cup deep drawings, show the interest of the *3G* model. The experimental observations due to different materials properties or different friction coefficients are correctly reproduced by the implementation of the *3G* model in the ABAQUS code. For instance, experiments of cylindrical cup deep drawing at various speeds on a deep drawing steel are well predicted by simulations performed with different friction coefficients. The fracture occurring during medium to very low speed experiments is predicted (Figure 6-4). Axisymmetrical FEM simulations are performed, so the planar anisotropy is neglected.

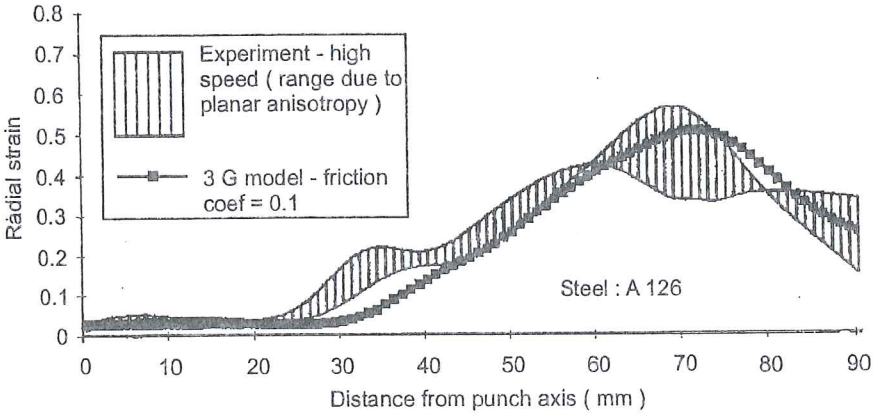

(a) High speed = low friction
(b) Medium speed = high friction

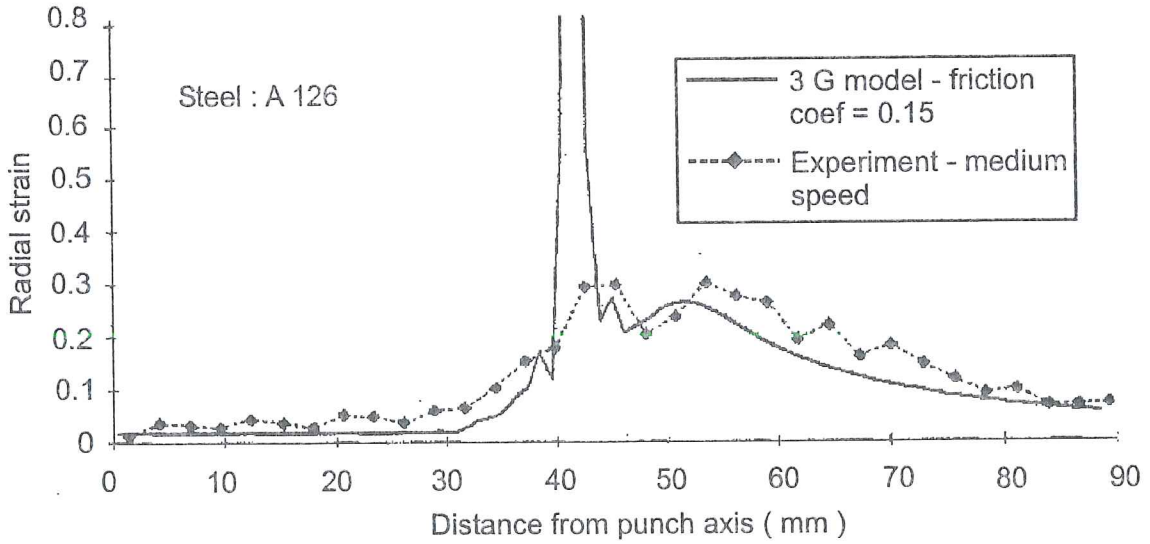

Figure 6-4 Comparisons between experiment and simulation for radial strains in cup drawing of a Deep Drawing steel (from Montfort & Defourny 1994).

The planar anisotropic behavior of the *3G* model is checked by theoretical and experimental considerations on the fracture of cylindrical cups (Montfort & Defourny 1994).

In conclusion, along simple strain paths, the *3G* model gives slightly more accurate results than the classical theory but its main advantage is to give a metallurgical background to the mathematical formulation of the material behavior. It has the basic ingredients to model the events happening in complex loading paths but specific improvements are needed to predict texture evolution or pre-strain effects. Its identification is not too heavy and its FEM implementation is not straightforward but tractable.

6.2.2. Khan & Cheng's model

Compared with a single crystal, a polycrystal contains a much larger number of slip systems, which are randomly distributed in the polycrystal. Khan & Cheng 1996's model applies the above idea to transfer the plasticity model of a single crystal to polycrystal level. Due to grain boundary effect, all slip systems interact. Describing the behavior of polycrystal implies formulating the interactions of all slip systems.

A single crystal yield locus is extended to a polycrystal yield locus by simply assuming a larger number of slip systems *s*. The macroscopic phenomenological approach of isotropic hardening is transferred to slip systems by equation (6-11), with the initial value of the plastic radius R_0 and its increment R^s. The backstress α^s modifies the center of the yield locus.

$$\left|\tau^s - \alpha^s\right| \le R^s + R_0 \tag{6-11}$$

The projection already presented at microscopic level in relation (3-2) is applied here to get the resolved shear stress:

$$\tau^s = A_{ij}^s \sigma_{ij}^{macro} \tag{3-2}$$

Isotropic and kinematic hardening rules affect each slip system; their evolution is defined by relations :

$$\dot{\alpha}^s = \sum_j^N b_\alpha \dot{\gamma}^j \left(X_0 + X_1 A_{kl}^s A_{kl}^j + X_3 \left(A_{kl}^s A_{kl}^j \right)^3 - \alpha^s \right) \tag{6-12}$$

$$\dot{R}^s = \sum_j^N b_R \dot{\gamma}^j \left(R_0 + R_2 (A_{kl}^s A_{kl}^j)^2 - R^s \right) \tag{6-13}$$

The first terms on the right hand side of relations (6-12) and (6-13) respectively correspond to classical isotropic and kinematic models. The next terms take into account the shape change of the yield surface. The final feedback terms account for the dependence of the plastic behavior of slip systems on deformation history. The constants X_0, X_1, X_3, R_0, R_2 are the saturated values of the corresponding hardening and b_α, b_R are the shape-control parameters.

To show the credibility of the extension from single crystal to polycrystal by simply increasing the number of slip systems, an alternative analysis of the self-consistent method is proposed to consider the effect of grain boundaries on the behavior of polycrystals. The analysis concludes that the effect of grain boundaries could be incorporated in the interactions of slip systems. Unfortunately, further comparisons with experiments announced in the paper I (Khan & Cheng 1996) could not be found.

6.2.3. Aifantis' models

Aifantis 1987 is a typical macroscopic model imbued from single crystal plasticity. It is based on a *scale invariance concept*, which assumes that the structure of the resulting equations is preserved during a transition from the micro-scale to the macro-scale.

The single crystal model proposed by Aifantis considers a single family of dislocations moving along a slip system identified by two vectors, n_j^s (normal unit vector to the slip plane for the slip system *s)* and b_j^s (unit vector in the slip direction for the slip system *s*). The associated Schmid's tensor K_{ij}^s (relation 3-1), its symmetric part A_{ij}^s and its skew-symmetric part Z_{ij}^s also appear. Hereafter the superscript *s* is dropped as only one slip family is taken into account.

The microscopic state is represented by two sets of equations specifically representing conservation rules and constitutive relations. The mass and momentum balance equations are :

$$\frac{\partial \rho}{\partial t} + div\, \underline{j} = \hat{c} \tag{6-14}$$

$$div \underline{\alpha} = \underline{\hat{f}} \tag{6-15}$$

with ρ the dislocation density, $\underline{j}$ the dislocation flux, $\underline{\alpha}$ the dislocation stress (associated to the classical back stress in macroscopic models), *t* the time. The source terms $\hat{c}$ and $\underline{\hat{f}}$ measure the mass and momentum exchanges between dislocations and lattice. Specifically $\hat{c}$ represents the generation, immobilisation or annihilation of dislocations and $\underline{\hat{f}}$ includes the effect of lattice friction, damping and Peach-Koehler's force acting on a dislocation as a result of the applied stress.

The constitutive equations are assumed to be of the form:

$$\underline{\alpha} = t_A \underline{A} + t_b \underline{b} \otimes \underline{b} + t_n \underline{n} \otimes \underline{n} \tag{6-16}$$

$$\underline{\hat{f}} = (a_{1b} - a_{2b} \tau_{effective} - a_{3b}\, j_b)\, \underline{b} + (a_{1n} - a_{2n} \tau_n - a_{3n}\, j_n)\, \underline{n} \tag{6-17}$$

$$\hat{c} = \hat{c}(\rho, j_b, j_n, \tau_{effective}, \tau_n) \tag{6-18}$$

where $a_{1b}, a_{2b}, a_{3b}, a_{1n}, a_{2n}, a_{3n}, t_A, t_b, t_n$ are assumed functions of ρ. The coefficients t_A, t_b, t_n measure the interaction forces between dislocations and are responsible for the development of internal stresses. The coefficients a_{1b}, a_{1n} measure the lattice-dislocation interactions and are responsible for yielding. The coefficients a_{2b}, a_{2n} measure the effect of Peach-Koehler's force, while a_{3b}, a_{3n} measure the drag associated with dislocation motion and are responsible for internal damping and viscoplastic flow. The other variables are defined by:

$$\tau_{effective} = (\sigma_{ij}^{micro} - \alpha_{ij}) A_{ij}$$

$$\tau_n = (\sigma_{ij}^{micro} - \alpha_{ij})(n_i n_j)$$

$$j_b = \underline{j}.\underline{b}$$

$$j_n = \underline{j}.\underline{n} \tag{6-19}$$

where subscript b identifies glide components and subscript n climb components. Such a microscopic model helps to predict heterogeneity of plastic flow such as shear bands or Portevin-Le Chatelier bands (Aifantis 1987).

As macroscopic plasticity smoothes out plastic micro-heterogeneities, it is assumed that, at macroscopic level, the divergence terms of relations (6-14) and (6-15) have no influence and can be dropped. The macroscopic plasticity theory neglecting volume changes, the climb process appearing in (6-17) and (6-18) is neglected. In (6-16), the stress $t_n \underline{n} \otimes \underline{n}$, which accounts for presence of dislocation dipole and decomposition, can be kept but is often neglected as in Prager's kinematic hardening rule. Consequently, the macroscopic relations chosen by Aifantis are:

$$\dot{\rho} = \hat{c}(\rho, j_b, \tau_{effective}) \tag{6-20}$$

$$a_{1b} - a_{2b}\tau_{effective} - a_{3b}\, j_b = 0 \tag{6-21}$$

$$\underline{\sigma}^{effective} = \underline{\sigma}^{macro} - \underline{\alpha}^{macro} \tag{6-22}$$

$$\underline{\alpha}^{macro} = t_A \underline{A} + t_n \underline{N} \tag{6-23}$$

with $\underline{N} = \underline{n} \otimes \underline{n}$. The microscopic stress quantities $\underline{\sigma}^{micro}$, $\underline{\sigma}^{micro}$ - $\underline{\alpha}$, $\underline{\alpha}$ are assumed to preserve their character and interrelationship during the transition to macro scale. They are respectively identified with the macroscopic total stress $\underline{\sigma}^{macro}$, the macroscopic effective stress $\underline{\sigma}^{effective}$ and the macroscopic back stress $\underline{\alpha}^{macro}$. The yield condition is directly deduced from (6-21) and the macroscopic plastic strain is

assumed to be linked to an orientation tensor A_{ij} "equivalent" to the symmetric part of Schmid's tensor in the microscopic analysis:

$$\underline{\dot{\varepsilon}}^{p\,macro} = \dot{\gamma}^{p}\,\underline{A} \tag{6-24}$$

In Aifantis 1987, the macroscopic $\underline{A}$ tensor results from the macroscopic principle of maximum dissipation for maximum entropy production. This is related to the power associated with a dislocation motion along its slip plane:

$$\tau^{effective}\, j_b > 0 \quad \Leftrightarrow \quad (\underline{\sigma}^{macro} - \underline{\alpha}^{macro}) : \underline{\dot{\varepsilon}}^{p\,macro} > 0 \tag{6-25}$$

This leads to a maximization problem:

$$maximum\ of\ (\sigma_{ij}^{effective}\ A_{ij})$$

with applied constraints :

$$tr\,\underline{A} = 0 \quad ; \quad tr\,\underline{A}^2 = \frac{1}{2} \tag{6-26}$$

by analogy to the microscopic analysis where $\underline{A}$ is the symmetric part of Schmid's tensor.

The solution found by Aifantis is:

$$\underline{A} = \frac{\underline{\hat{\sigma}}^{effective}}{2\sqrt{\frac{1}{2}(\underline{\hat{\sigma}}^{effective})^2}} \tag{6-27}$$

where $\underline{\hat{\sigma}}^{effective}$ is the deviatoric part of stress tensor $\underline{\sigma}^{effective}$. This solution allows to retrieve Prandtl-Reuss' flow rule and von Mises' yield criterion:

$$\underline{\dot{\varepsilon}}^{p} = \frac{\dot{\gamma}^{p}}{2\sqrt{J_2}}\,\underline{\hat{\sigma}}^{effective} \qquad \sqrt{J_2} = \frac{a_{1b}}{a_{2b}} = \sigma_F \tag{6-28}$$

$$\text{with } J_2 = (1/2)\,\hat{\sigma}_{ij}^{effective}\,\hat{\sigma}_{ij}^{effective}.$$

Using standard kinematic arguments in conjunction with relation (6-24), Aifantis obtains, at the microscopic level, the plastic spin formulation. His result is equivalent to the expression adopted in usual theories of crystal plasticity for the plastic spin if only one slip system is considered (see relation 4-3b):

$$\underline{\Omega}^{p} = \dot{\gamma}^{p}\,\underline{Z} \tag{6-29}$$

where $\underline{Z}$ is the non-symmetric part of Schmid's tensor. By analogy to the microscopic state, the practical macroscopic relation for the plastic spin is derived by eliminating tensor $\underline{Z}$ from (6-29) thanks to the use of expressions (6-23) and (6-24):

$$\underline{\Omega}^{p} = -t_n^{-1}(\underline{\alpha}^{macro}\,\underline{\dot{\varepsilon}}^{p} - \underline{\dot{\varepsilon}}^{p}\,\underline{\alpha}^{macro}) \tag{6-30}$$

The above relations (6-20 to 6-24), (6-27), (6-30), define Aifantis' macroscopic model, when a random texture results in an isotropic macroscopic behavior. Its interest is to be able to predict the development of axial strain due to torsion in free-end cylindrical specimens and the development of axial stress due to torsion in fixed-end cylindrical specimens (Swift effect, see section 3.5.4).

In cases where the effect of grain orientations cannot be neglected, Ning & Aifantis 1996 propose another version of the above model. The simplified relations (6-20 to 6-24), (6-27), (6-28), (6-29) are assumed here to be the constitutive relations for a single crystal.

Their model applies Taylor's assumption of equality of the velocity gradient at microscopic and macroscopic levels. It introduces an additional "texture spin" $\underline{\underline{\Omega}}^t$ not mentioned in section 4.1.1, where the material rotation was only subdivided into a plastic spin $\underline{\underline{\Omega}}^p$ and a crystal lattice rotation $\underline{\underline{\Omega}}^L$:

$$\underline{\underline{\Omega}}^{micro} = \underline{\underline{\Omega}}^{macro} = \underline{\underline{\Omega}}^p + \underline{\underline{\Omega}}^L \tag{4-3b}$$

Ning & Aifantis' texture spin $\underline{\underline{\Omega}}^t$ results from grain boundary constraints to maintain deformation compatibility. The final local material spin $\underline{\underline{\Omega}}^L$ is derived as the difference between the global spin $\left(\underline{\underline{\Omega}}^{micro} = \underline{\underline{\Omega}}^{macro}\right)$, related to the macroscopic velocity gradient, and two types of plastic spins, the usual plastic spin $\underline{\underline{\Omega}}^p$ due to crystal slip given by relation (6-29) and the texture spin $\underline{\underline{\Omega}}^t$ due to grain boundary effects:

$$\underline{\underline{\Omega}}^L = \underline{\underline{\Omega}}^{macro} - \underline{\underline{\Omega}}^p - \underline{\underline{\Omega}}^t \tag{6-31}$$

Ning & Aifantis define a crystal orientation by a unit vector $\underline{a}$ oriented in the crystal direction, expressed as a function of the slip system identifiers $\underline{n}$, $\underline{b}$ and of the angle between $\underline{a}$ and $\underline{b}$. Then, they use the classical concept of Orientation Distribution Function f, which represents the probability for a grain to be oriented along $\underline{a}$ at time t. The evolution of the ODF is prescribed by a conservation rule as already presented in section 5.5.3, which can be solved analytically in the case of an initial random texture and simple deformation gradient tensor.

Ning & Aifantis' micro-macro link differs from the classical volume average procedure expressed in its integrated form by (5-40), or in its discrete form by (5-18 or 5-19). Such a classic average procedure does not consider the effect of morphological texture. For instance, the fact that the orientation of large grains may have a more pronounced effect than that of small grains. The following improved average relation is proposed:

$$\underline{x}^{macro} = \oint \underline{\underline{K}}(\underline{a}) : \underline{x}^{micro} f(\underline{a},t)\, d\underline{a} \tag{6-32}$$

where $\underline{x}^{micro}$ is either the deviatoric Cauchy stress or the back stress at the crystal level and $\underline{x}^{macro}$ is the associated macroscopic value. The fourth order tensor $\underline{\underline{K}}$, called "texture" tensor, is a function of $\underline{a}$. Due to the stress symmetry, it is a transversely isotropic tensor finally defined by only three independent material parameters. The overall plastic flow rule and yield condition are then obtained by combining the flow rule and yield condition assumed at the crystal level (see 6-28) and the average stress relation (6-32). This results in the flow rule:

$$\underline{\dot{\varepsilon}}^{p} = \frac{\dot{\gamma}^{p}}{2\sigma_{F}(\gamma^{p})} \langle \underline{\underline{K}} \rangle^{-1} : \underline{\hat{\sigma}}^{effective} \tag{6-33}$$

and the yield condition:

$$\sqrt{\frac{1}{2} \underline{\hat{\sigma}}^{effectif} \langle \underline{\underline{K}} \rangle^{-1} \langle \underline{\underline{K}} \rangle^{-1} \underline{\hat{\sigma}}^{effectif}} = \sigma_{F}(\gamma^{p}) \tag{6-34}$$

where the overall texture tensor $\langle \underline{\underline{K}} \rangle$ is defined by the average formula:

$$\langle \underline{\underline{K}} \rangle = \oint \underline{\underline{K}} \, f(\underline{a},t) \, d\underline{a} \tag{6-35}$$

Relation (6-33) is similar to the previous phenomenological relations for the description of the yield behavior of metallic materials, based on the introduction of "modified" stress tensors as, for instance, in Karafillis & Boyce 1993, presented in section 2.1.2.

The evolution of the macroscopic back stress and the plastic spin $\underline{\Omega}^{p}$ are deduced from their microscopic value, Taylor's assumption and the same averaging procedure.

The macroscopic counterpart of the additional spin $\underline{\Omega}^{t}$ describes the overall average grain rotation. Thus, it cannot be expressed in terms of the average slip processes alone. The average procedure (6-32) is slightly modified and applied now to a vector associated with the skew-symmetric tensor $\underline{\Omega}^{t}$. The fourth order tensor $\underline{\underline{K}}$ is reduced to a second order tensor, isotropic function of vector $\underline{a}$, taking into account 2 material parameters related to plastic strain history and temperature as well as to grain size and shape.

Like the above isotropic macroscopic model, this anisotropic macroscopic model has been applied to the prediction of Swift's effect. This is a simple case as it is possible to find an analytical form of the ODF function. Analytical and experimental results are very close as shown on Figure 6-5.

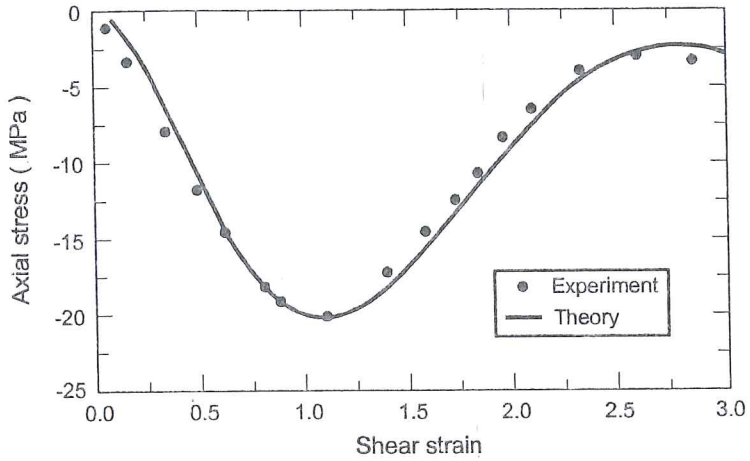

Figure 6-5 Comparison between theoretical predictions and experimental data for the non-monotonic evolution of the axial stress in a copper bar under fixed-end torsion (from Ning & Aifantis 1996).

As reported by Ning & Aifantis, these predictions were much less straightforward in previous attempts with other macroscopic models.

The yield behavior in tension coupled to torsion has been further studied for a theoretical material. For instance, Figure 6-6 and Figure 6-7 show the evolution of the initial yield locus. They respectively correspond to a tension dominated deformation state and a shear dominated deformation mode. The results show that the texture development causes both rotation and distortion of the yield surface, the shear mode having a more pronounced effect than the tension mode.

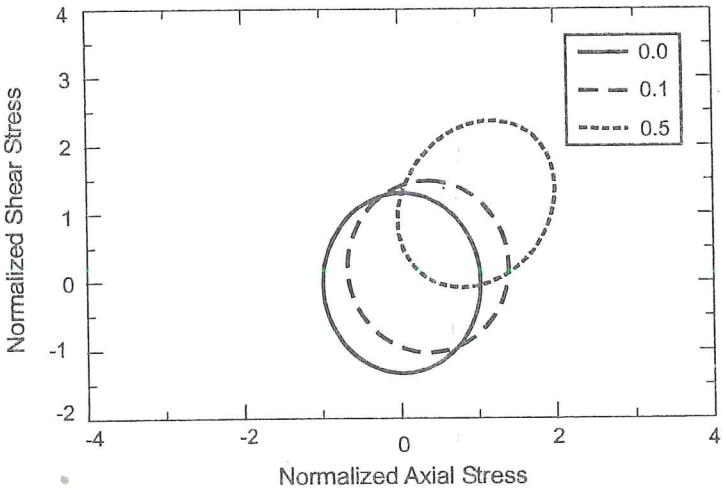

Figure 6-6 Evolution of yield surface in tension-torsion for different tensile strains: 0, 0.1, 0.5, and a ratio shear/axial strain of 1 (from Ning & Aifantis 1996).

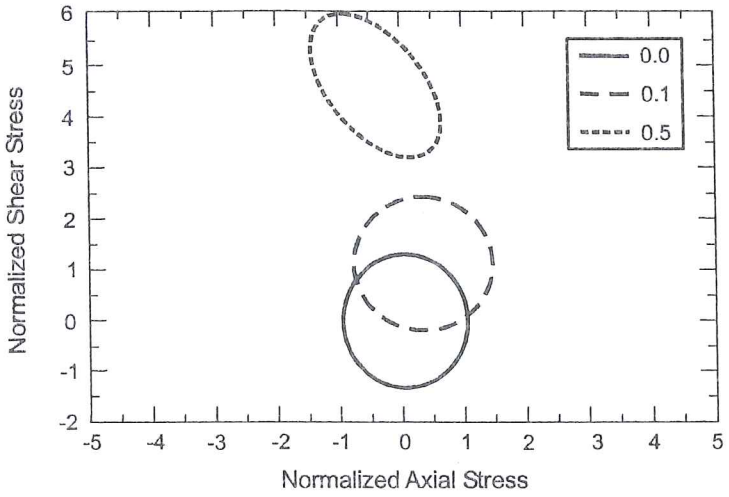

Figure 6-7 Evolution of yield surface in tension-torsion for different tensile strains: 0; 0.1; 0.5 and a ratio shear/axial strain of 5 (from Ning & Aifantis 1996).

A comparison of model predictions with available experimental data in small deformations (effect of plastic spin neglected) is presented on Figure 6-8 for 304 stainless steel in tension-torsion.

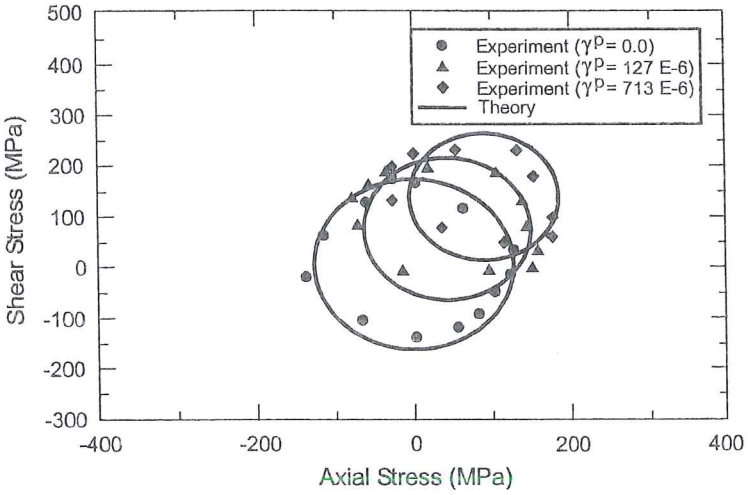

Figure 6-8 Comparison between theoretical predictions and experimental data for the yield surface of 304 stainless steel in tension-torsion, γ^p means here equivalent plastic strain (from Ning & Aifantis 1996).

In short, these macroscopic models imbued from single crystal plasticity can predict mechanical behavior quite accurately. Ning & Aifantis 1996 analytically compute the ODF evolution in some simple cases. However, the extension of this model to a general velocity gradient seems heavy from both computational and theoretical points of view. The latter model has the advantage of giving microscopic fundamental bases for phenomenological models, which propose the same form for the yield locus function.

6.2.4. Conclusion

3G or Aifantis' models propose macroscopic plasticity models based on the knowledge of crystal plasticity. Each one makes some assumptions to provide "simple" useful macroscopic constitutive laws. Their applications verify that the actual behavior under complex loading paths can be predicted. It is however clear that each specific path (tension + torsion, pre-straining...) may need some adjustments of the models.

Such models are neither straightforward to implement in FEM code nor to identify. So it is not surprising that they generally seem to be used only by the teams that have developed them. They provide more accurate results than simple phenomenological approaches. Aifantis's model also gives a theoretical justification for more advanced phenomenological models such as Karafillis & Boyce 1993.

6.3. Analytical yield loci computed from texture data

First, section 6.3.1 presents the classical way to obtain a macroscopic yield locus thanks to classical single crystal plasticity combined with texture description. As this approach does not give an analytical formulation easy to implement in FEM codes, different ways to derive an analytic function for the flow surfaces have been proposed. Some are described in sections 6.3.2 to 6.3.4.

6.3.1. Polycrystal yield locus obtained by Taylor's approach

Let us recall the important notions of Taylor's factor and average Taylor's factor, as the latter appears as a material parameter able to express the response of a textured material submitted to a given strain rate.

$M(g, \underline{U}_{\dot{\varepsilon}^p})$ is the Taylor's factor associated to a crystal of orientation g for a given strain mode $\underline{U}_{\dot{\varepsilon}^p}$ (plastic strain rate tensor divided by the equivalent plastic strain rate, relation 4-7). It is conventionally derived from the single crystal plastic power dissipation per unit volume $\dot{W}^p$ by the following relation:

$$M(g, \underline{U}_{\dot{\varepsilon}^p}) = \frac{\dot{W}^p}{\dot{\varepsilon}_{eq}^{p\,micro}\tau_c} = \sum_s \alpha_s \left|\dot{\gamma}^s_{scaled}\right| = \frac{1}{\tau_c}\sigma_{ij}^{micro}(U_{\dot{\varepsilon}^p})_{ij} \qquad (4\text{-}14)$$

Physically, it represents a certain amount of dislocation glide rate associated with a crystal orientation and an applied strain mode.

At the level of a polycrystal, the average plastic work dissipation per unit volume has been established in section 4.5.2 as a function of the ODF $f(g)$, which effect is then hidden in the average Taylor's factor $\overline{M}(\underline{U}_{\dot{\varepsilon}^p})$:

$$\overline{\dot{W}^{p}}(\underline{\dot{\varepsilon}}^{p\,macro}) = \oint \dot{W}^{p}(\underline{\dot{\varepsilon}}^{p\,micro}, g) f(g)\, dg = \dot{\varepsilon}_{eq}^{p\,macro} \bar{\tau}_c \overline{M}(\underline{U}_{\dot{\varepsilon}^p}) = \sigma_{eq}^{macro} \dot{\varepsilon}_{eq}^{p\,macro} \quad (4\text{-}33)$$

$$\overline{M}(\underline{U}_{\dot{\varepsilon}^p}) = \oint M(\underline{U}_{\dot{\varepsilon}^p}, g) f(g)\, dg \quad (4\text{-}34)$$

Taylor's assumptions of equality between the strain rates at the crystal level and at the macroscopic level as well as a common CRSS for all slip systems and all grains are both used in relation (4-33). Studying this equation :

$$\dot{\varepsilon}_{eq}^{p\,macro} \bar{\tau}_c\, \overline{M}(\underline{U}_{\dot{\varepsilon}^p}) = \sigma_{eq}^{macro} \dot{\varepsilon}_{eq}^{p\,macro} = \underline{\sigma}^{macro} : \underline{\dot{\varepsilon}}^{p\,macro} \quad (6\text{-}36)$$

one can see that, if the macroscopic strain rate $\underline{\dot{\varepsilon}}^{p\,macro}$ is known, $\overline{M}(\underline{U}_{\dot{\varepsilon}^p})$ can be computed and all stress tensors $\underline{\sigma}^{macro}$ * that satisfy (6-36) constitute hyperplanes in stress vectors space. The strain rate vector $\underline{\dot{\varepsilon}}^{p\,macro}$ are perpendicular to these hyperplanes. In practice, as already explained, only the deviatoric stress tensors are considered in the plastic state, so the stress space is a 5 dimensional space. The deviatoric stress $\underline{\hat{\sigma}}^{macro}$ corresponding to $\underline{\dot{\varepsilon}}^{p\,macro}$ is one point of the hyperplane. According to the normality rule, the yield locus must be tangent to the hyperplane at the location of $\underline{\sigma}^{macro}$ (see Figure 6-9). Since the yield locus must be convex, it is the inner envelope of the hyperplanes associated with all possible strain modes.

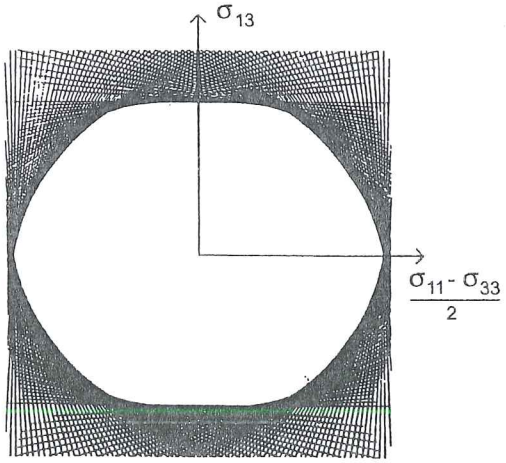

Figure 6-9 Example of projection of the yield locus onto the subspace $\frac{\sigma_{11}-\sigma_{33}}{2}, \sigma_{13}$ (from Canova *et al* 1985).

The practical way to build 2-dimensional projections of the yield surface is described in Canova *et al.* 1985, Lequeu *et al.* 1987a, van Houtte 1992. Some details on van Houtte's approach will be given in section 6.3.4.

6.3.2. Proposals applying concepts from Montheillet

Lequeu *et al.* 1987b follow the approach of Montheillet *et al.* 1985, where the principal axes of anisotropy are chosen to coincide with the $\langle 100 \rangle$ axes of the studied texture component, rather than with the symmetry axes of the workpiece. Another characteristic of this method consists in the determination of the coefficients of the yield function only from crystallographic considerations. According to Montheillet *et al.* 1985, the yield locus of a highly textured f.c.c or b.c.c polycrystal, containing a dispersion of orientations about a single ideal orientation (cube textures) is given by :

$$\begin{aligned} F_p(\underline{\hat{\sigma}}) = \alpha\left\{|\hat{\sigma}_{11}-\hat{\sigma}_{22}|^n + |\hat{\sigma}_{22}-\hat{\sigma}_{33}|^n + |\hat{\sigma}_{33}-\hat{\sigma}_{11}|^n\right\} \\ + 2\beta\left\{|\hat{\sigma}_{12}|^n + |\hat{\sigma}_{23}|^n + |\hat{\sigma}_{31}|^n\right\} = (\sqrt{6}\tau_c)^n \end{aligned} \tag{6-37}$$

where $\hat{\sigma}_{ij}$ are the components of the macroscopic deviatoric stress tensor. The coefficient n must be equal or greater than 1 to satisfy convexity requirement. The values of α and β depend on n. The parameters are identified from the best fit between (6-37) and the single crystal yield locus computed by Schmid's law and Taylor-Bishop-Hill's. Figure 6-10 and Figure 6-11 respectively show the π-plane section and the shear plane section of the yield loci computed by (6-37) and by Taylor-Bishop-Hill's formulation.

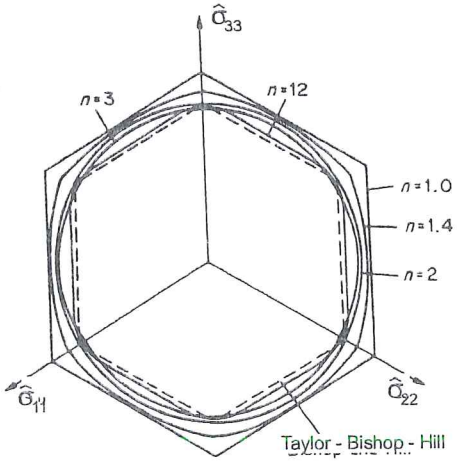

Figure 6-10 π-plane sections of Taylor-Bischop-Hill's single crystal yield locus and yield surfaces defined by (6-37) for 5 values of the exponent n (from Lequeu *et al.* 1987b).

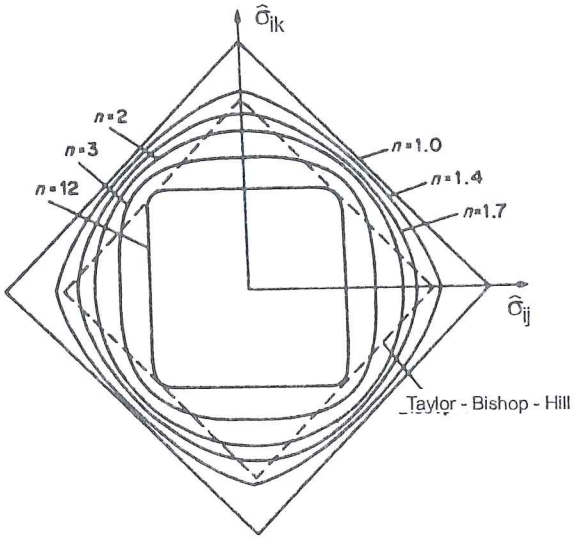

Figure 6-11 Shear plane sections of Taylor-Bischop-Hill's single crystal yield locus and yield surfaces defined by (6-37) for 6 values of the exponent n (from Lequeu *et al.*, 1987b).

The best overall fit with respect to the single crystal yield locus is obtained with $n = 1.7$, $\alpha = 0.47$, $\beta = 0.54$. The final objective is of course not an analytical yield surface describing a material with a sharp cube texture. The goal is to develop analytical models for any textured material containing one or more arbitrary orientations. Therefore the comparisons between the relation (6-37) and crystallographic yield loci should be interpreted as concerning individual texture components, which in reality are cube textures oriented along particular directions in the material. Lequeu *et al.* 1987b introduce a transformation matrix between crystallographic axes and workpiece axes, that is used to adapt the yield surface (6-37) to any texture component. When more than one texture component is involved, a Sachs' approach is used. Some comparisons between experimental and computed yield loci are shown on Figure 6-12, where σ_0 and σ_{90} are the yield stresses in uniaxial tension along rolling and transverse directions respectively. The angle ω_0, called the scatter width, expresses the misorientation about the ideal orientation associated with one texture component. Lequeu *et al.* 1987a study the effect of increasing the scatter width on π-plane and shear stress cross-sections of the yield locus .

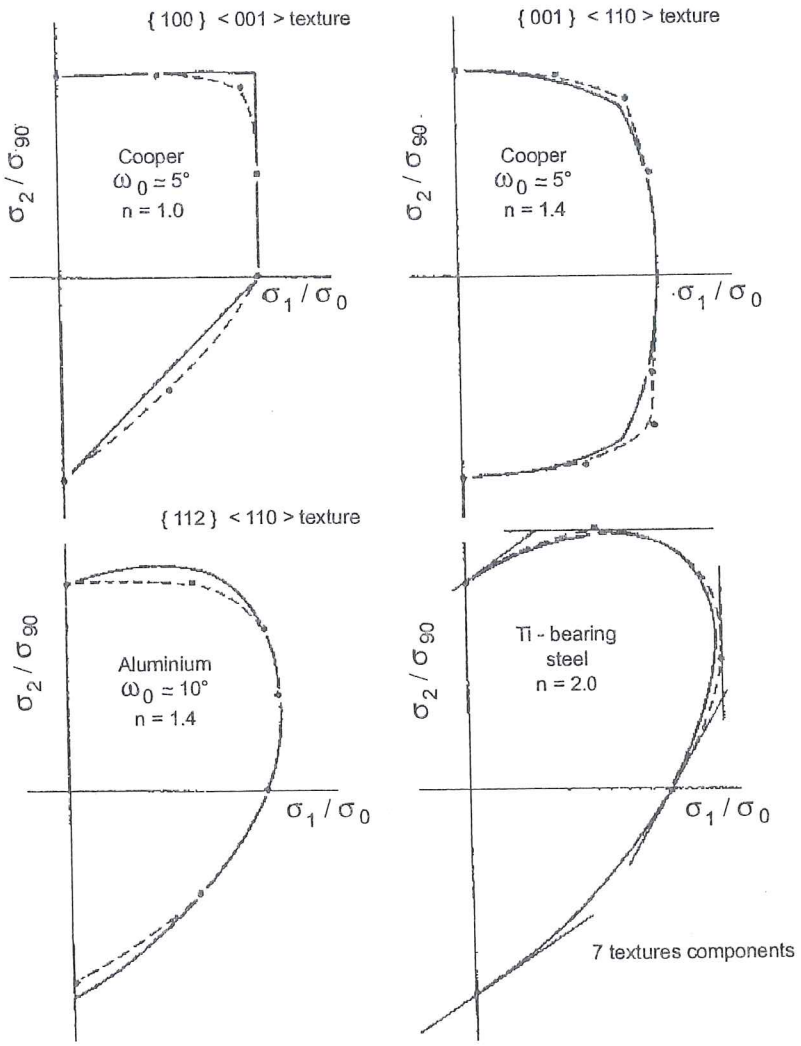

Figure 6-12 Comparison between experimental yield loci (dotted lines) reported in literature and the predictions by Lequeu's approach (straight lines), (from Lequeu *et al.* 1987b).

In summary, this approach adjusts an analytical function on Taylor-Bischop-Hill's single crystal locus; then, by rotation, adapts it according to macroscopic axes and uses a Sachs' approach when the material has more than one texture component.

Darrieulat & Piot 1996 apply the same type of approach to f.c.c materials characterised by 12 slip systems. However, they consider a more accurate representation of the microscopic behavior and take into account the ODF function to represent the texture effect.

Beginning also with the plastic behavior at the single crystal level, Darrieulat & Piot 1996 express Schmid's law by an analytical form obtained through a classical mathematical property of power averages already proposed by Arminjon 1988:

$$F_p(\underline{\hat{\sigma}}) = \left(\sum_{s=1}^{12} \left| \frac{\underline{\hat{\sigma}} : \underline{A}^s}{\tau_c^s} \right|^n \right)^{\frac{1}{n}} = 1 \qquad (6\text{-}38)$$

where $\underline{A}^s$ is the symmetric part of Schmid's tensor (3-1) associated with the slip system s. Function (6-38) is differentiable, strictly convex and is arbitrarily close to the inner envelope of the hyperplanes of equations:

$$\left| \frac{\underline{\hat{\sigma}} : \underline{A}^s}{\tau_c^s} \right| = 1 \qquad s = 1,...,12 \qquad (6\text{-}39)$$

Applying the normality rule to the yield surface, the plastic strain rate is computed by:

$$\underline{\dot{\varepsilon}}^p = \dot{\lambda} F_p^{\frac{1}{n}-1} \sum_{s=1}^{12} sgn(\underline{\hat{\sigma}} : \underline{A}^s) \left| \underline{\hat{\sigma}} : \underline{A}^s \right|^{n-1} \underline{A}^s \qquad (6\text{-}40)$$

It is interesting to note that this form is close to the macroscopic flow rule derived when the rate sensitive approach is applied at the crystal level (see relation (4-15)).

Figure 6-13 compares yield loci based on expression (6-38) for different values of n with results from Lequeu *et al.* 1987a.

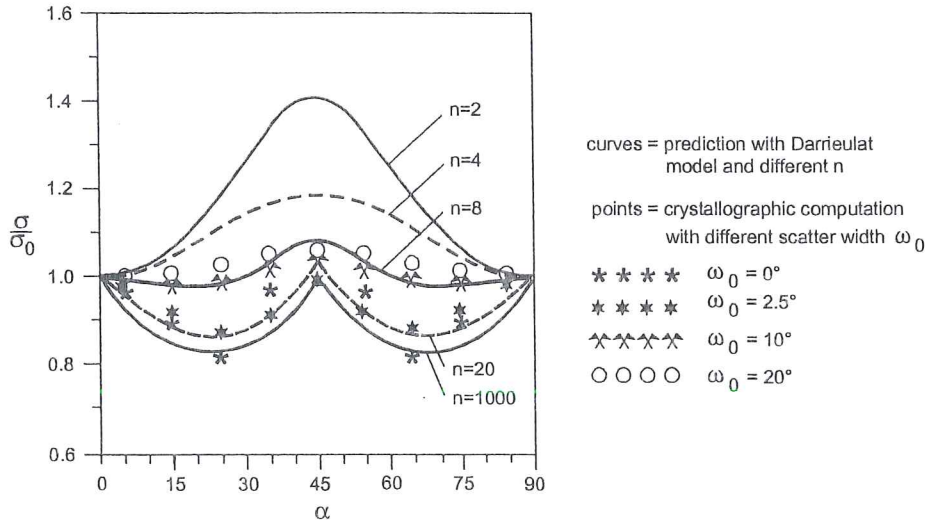

Figure 6-13 For cube orientation, yield stress versus the angle to the Rolling Direction by Darrieulat & Piot and crystal models assuming different scattering width angles ω_0 (Darrieulat & Piot 1996).

When an orthotropic material is known through its N crystallographic components, relation (6-38) provides a differentiable representation of the mechanical behavior that can be attributed to each component. The macroscopic behavior is some average between them. A simple physical assumption close to Khan & Cheng's 1996 proposal (see section 6.2.2) is that polycrystals behave like crystals possessing not 12

slip systems but 12 x N slip systems, the orientations of which are given by the texture data. Each of the N sets contributes proportionally to its volume fraction.

Let the texture be defined by an ODF $f(g)$ function of Euler's angles $\varphi_1, \Phi, \varphi_2$ (Figure 3-4). If Euler's space is covered by a step Δ, one value f_i of the ODF represents the average intensity of the orientations in the solid angle $\left[\varphi_1 - \frac{\Delta}{2}, \varphi_1 + \frac{\Delta}{2}\right] x \left[\Phi - \frac{\Delta}{2}, \Phi + \frac{\Delta}{2}\right] x \left[\varphi_3 - \frac{\Delta}{2}, \varphi_3 + \frac{\Delta}{2}\right]$. It is also the volume fraction of crystals belonging to this orientation space sector. The number of crystallographic orientations N directly depends on the size of Δ.

Using the same power average as in relation (6-38), the plastic behavior of the polycrystal is given by:

$$F_p = \left(\sum_{i=1}^{N} f_i \sum_{s=1}^{12} \left| \hat{\underline{\sigma}}_i^{micro} : \underline{A}_i^s \right|^n \right)^{\frac{1}{n}} = \bar{\tau}_c \qquad (6\text{-}41)$$

where Taylor's assumption of a common value of CRSS is adopted for all the slip systems and all the crystals. The subscript i identifies the texture component. This tensorial expression being the average of strictly convex and differentiable terms, it is also strictly convex and differentiable. It can be easily computed no matter what the chosen axes are.

If $n = 2$, relation (6-41) is a quadratic criterion similar to Hill's 1948 yield locus. Darrieulat & Piot 1996 give the 6 coefficients of Hill's 1948 criterion as functions of f_i and $\underline{A}^s$.

The macroscopic mechanical behavior $(\hat{\underline{\sigma}}^{macro}, \dot{\underline{\varepsilon}}^{p\,macro})$ of a polycrystal can be predicted from each of its component $(\hat{\underline{\sigma}}_i^{micro}, \dot{\underline{\varepsilon}}_i^{p\,micro})$ if :

- either a uniform stress $(\hat{\underline{\sigma}}_i^{micro} = \hat{\underline{\sigma}}^{macro})$ or a uniform strain $(\dot{\underline{\varepsilon}}_i^{p\,micro} = \dot{\underline{\varepsilon}}^{macro})$ assumption is accepted. Here, Darrieulat and Piot choose the stress uniformity;
- a condition of homogenisation is applied:

$$\sum_{i=1}^{N} f_i \hat{\underline{\sigma}}_i : \dot{\underline{\varepsilon}}_i = \hat{\underline{\sigma}}^{macro} : \dot{\underline{\varepsilon}}^{macro} \qquad (6\text{-}42)$$

The details are given in Darrieulat & Piot's 1996 paper, where a slightly modified relation (6-41) using two exponents instead of one is also checked. Their conclusions are that proposal (6-41) gives good results for low values of n (up to 10) but assigns a too large influence to crystallographic texture when n increases. Their validations consist in predictions of uniaxial yield stresses and Lankford's coefficients as functions of the angle with the rolling direction. This is done for a single component texture or real materials such as aluminium 3004 or 5182.

6.3.3. Arminjon, Bacroix, Imbault... 's potential formulation

Arminjon 1988, Arminjon & Bacroix 1991, Arminjon *et al.* 1994 propose an identification of the plastic work rates to derive a yield criterion applied to polycrystalline materials. When a quadratic form is assumed, the macroscopic anisotropy parameters become explicit functions of the texture coefficients. Their approach is summarized hereafter.

In visco-plastic models, the existence of two dual convex potentials E and E_c is usually assumed. They define the relationship giving the stress tensor as function of the plastic strain rate tensor as well as the inverse relation:

$$\underline{\sigma} = \frac{\partial E}{\partial \underline{\dot{\varepsilon}}^p} \qquad \underline{\dot{\varepsilon}}^p = \frac{\partial E_c}{\partial \underline{\sigma}} \tag{6-43a,b}$$

where functions E and E_c exchange by Legendre's transformation. In case of rate-independent standard plasticity, function E is simply the rate of plastic work $\dot{W}^p$. The complementary function E_c cannot be defined, since the strain rate $\underline{\dot{\varepsilon}}^p$ is only determined by the stress tensor $\underline{\sigma}$ up to the plastic multiplier $\dot{\lambda}(\underline{\dot{\varepsilon}}^p)$ and relation (2-3) of associated flow rule is used:

$$\underline{\dot{\varepsilon}}^p = \dot{\lambda}(\underline{\dot{\varepsilon}}^p)\frac{\partial F_p}{\partial \underline{\sigma}} \tag{6-44}$$

In this section, the yield locus is expressed as:

$$F_p(\underline{\sigma}) = \bar{\tau}_c \tag{6-45}$$

Following Hill 1987, F_p can be formulated as an homogeneous function of order one with respect to positive multipliers. This property implies :

$$F_p(\underline{\sigma}) = \underline{\sigma} : \frac{\partial F_p}{\partial \underline{\sigma}} \tag{6-46}$$

Relations (6-44) to (6-46) allow to give the following expression of the rate of plastic work:

$$\dot{W}^p = \underline{\sigma} : \underline{\dot{\varepsilon}}^p = F_p(\underline{\sigma})\,\dot{\lambda}(\underline{\dot{\varepsilon}}^p) = \bar{\tau}_c\,\dot{\lambda}(\underline{\dot{\varepsilon}}^p) \tag{6-47}$$

In practice, using (6-43a) and (6-47), Arminjon writes:

$$\underline{\sigma} = \frac{\partial \dot{W}^p}{\partial \underline{\dot{\varepsilon}}^p} = \frac{\partial(\bar{\tau}_c \dot{\lambda}(\underline{\dot{\varepsilon}}^p))}{\partial \underline{\dot{\varepsilon}}^p} = F_p(\underline{\sigma})\frac{\partial\, \dot{\lambda}(\underline{\dot{\varepsilon}}^p)}{\partial \underline{\dot{\varepsilon}}^p} \tag{6-48}$$

Compare the macroscopic expression of the plastic power dissipation (6-47) with the micro-macro one (4-33), presented as an average value and recalled here:

$$\overline{\dot{W}^p}(\underline{\dot{\varepsilon}}^{p\,macro}) = \oint \dot{W}^p(\underline{\dot{\varepsilon}}^{p\,micro}, g) f(g)\,dg = \dot{\varepsilon}_{eq}^{p\,macro}\,\bar{\tau}_c\,\overline{M}(\underline{U}_{\dot{\varepsilon}^p}) = \sigma_{eq}^{macro}\,\dot{\varepsilon}_{eq}^{p\,macro} \tag{4-33}$$

One can find physical interpretations for each term. $\bar{\tau}_c$ is the average CRSS in the polycrystal. $\dot{\lambda}$ is naturally expressed from the texture alone and is characterized by the average Taylor's factor defined by relation (4-34) :

$$\overline{M}(\underline{U}_{\dot{\varepsilon}^p}) = \oint M(\underline{U}_{\dot{\varepsilon}^p}, g) f(g) dg \tag{4-34}$$

The above relations assume the equality between the macroscopic strain rate and the microscopic one. So, all the further analytical formulation is based on this so-called Taylor's hypothesis.

Arminjon & Bacroix 1991 define four requirements that functions $\dot{\lambda}(\underline{\dot{\varepsilon}}^p)$ in strain rate space, or F_p in stress space, have to fulfil:

- convexity,
- respect of orthotropic material symmetry,
- homogeneity,
- use of deviatoric tensors only.

If one chooses a polynomial function, the convexity must be checked. The hereafter defined 4th order homogeneous function F of plastic strain rate (which is a deviatoric tensor) respects also the 3 other characteristics. Let us define the function in plastic strain rate space:

$$F = \sum_{k=1}^{22} \alpha_k X_k \tag{6-49}$$

$X_1 = (\dot{\varepsilon}^p_{11})^4$ $X_2 = (\dot{\varepsilon}^p_{22})^4$ $X_3 = (\dot{\varepsilon}^p_{23})^4$ $X_4 = (\dot{\varepsilon}^p_{13})^4$

$X_5 = (\dot{\varepsilon}^p_{12})^4$ $X_6 = (\dot{\varepsilon}^p_{11})^3 \dot{\varepsilon}^p_{22}$ $X_7 = (\dot{\varepsilon}^p_{22})^3 \dot{\varepsilon}^p_{11}$ $X_8 = (\dot{\varepsilon}^p_{11})^2 (\dot{\varepsilon}^p_{22})^2$

$X_9 = (\dot{\varepsilon}^p_{11})^2 (\dot{\varepsilon}^p_{23})^2$ $X_{10} = (\dot{\varepsilon}^p_{11})^2 (\dot{\varepsilon}^p_{13})^2$ $X_{11} = (\dot{\varepsilon}^p_{11})^2 (\dot{\varepsilon}^p_{12})^2$ $X_{12} = (\dot{\varepsilon}^p_{22})^2 (\dot{\varepsilon}^p_{23})^2$

$X_{13} = (\dot{\varepsilon}^p_{22})^2 (\dot{\varepsilon}^p_{13})^2$ $X_{14} = (\dot{\varepsilon}^p_{22})^2 (\dot{\varepsilon}^p_{12})^2$ $X_{15} = (\dot{\varepsilon}^p_{23})^2 (\dot{\varepsilon}^p_{13})^2$ $X_{16} = (\dot{\varepsilon}^p_{23})^2 (\dot{\varepsilon}^p_{12})^2$

$X_{17} = (\dot{\varepsilon}^p_{13})^2 (\dot{\varepsilon}^p_{12})^2$ $X_{18} = \dot{\varepsilon}^p_{11} \dot{\varepsilon}^p_{22} (\dot{\varepsilon}^p_{23})^2$ $X_{19} = \dot{\varepsilon}^p_{11} \dot{\varepsilon}^p_{22} (\dot{\varepsilon}^p_{13})^2$ $X_{20} = \dot{\varepsilon}^p_{11} \dot{\varepsilon}^p_{22} (\dot{\varepsilon}^p_{12})^2$

$X_{21} = \dot{\varepsilon}^p_{11} \dot{\varepsilon}^p_{23} \dot{\varepsilon}^p_{13} \dot{\varepsilon}^p_{12}$ $X_{22} = \dot{\varepsilon}^p_{22} \dot{\varepsilon}^p_{23} \dot{\varepsilon}^p_{13} \dot{\varepsilon}^p_{12}$

where symmetry $\varepsilon_{ij} = \varepsilon_{ji}$ is assumed and only $i \le j$ terms are present.

A scaled function is used in practice as function $\dot{\lambda}$:

$$\dot{\lambda}(\underline{\dot{\varepsilon}}^p) = \frac{\dot{W}^p}{\tau_c} = F(\underline{\dot{\varepsilon}}^p) / (\dot{\varepsilon}^p_{eq})^3 = \sum_{k=1}^{22} \alpha_k \psi_k(\underline{\dot{\varepsilon}}^p) \tag{6-50}$$

with $\psi_k(\underline{\dot{\varepsilon}}^p) = X_k(\underline{\dot{\varepsilon}}^p)/(\dot{\varepsilon}^p_{eq})^3$.

Note that symmetry $\sigma_{ij} = \sigma_{ji}$ is not assumed in (6-48) but taken into account in (6-49). So the stresses are computed by :

$$\sigma_{ij} = \bar{\tau}_c \frac{\partial \dot{\lambda}}{\partial \dot{\varepsilon}^p_{ij}} \quad if\ i = j$$
$$\sigma_{ij} = \frac{1}{2} \bar{\tau}_c \frac{\partial \dot{\lambda}}{\partial \dot{\varepsilon}^p_{ij}} \quad if\ i < j \qquad (6\text{-}51)$$

As explained hereafter, the choice (6-50) leads to represent the coefficients α_k by a linear function of coefficients C_i, equivalent to the well-known $C_l^{\mu\nu}$ coefficients of the ODF. Here for simplicity, a single index notation is adopted to identify C_i coefficients. So, the relation (3-5) defining $C_l^{\mu\nu}$ coefficients is adapted:

$$f(g) \cong \sum_{l=0}^{l_{max}} \sum_{\mu=1}^{\mu_{max}(l)} \sum_{\nu=1}^{\nu_{max}} C_l^{\mu\nu} \dot{\dot{T}}_l^{\mu\nu}(g) \qquad (3\text{-}5)$$

$$f(g) = \sum_{i=1}^{I} C_i T_i(g)$$

where l_{max} is the maximum degree of the series expansion;

I is the maximum index of Fourier's coefficients identified by a single index notation;

$\dot{\dot{T}}_l^{\mu\nu}(g)$ or $T_i(g)$ are harmonic functions of Euler's angles;

$C_l^{\mu\nu}$ or C_i are Fourier's coefficients describing the texture.

Looking at the above relations (6-51), (3-5), (4-33) and (4-34), one can express the function $\dot{\lambda}$, after algebraic manipulations, by a linear function of coefficients C_i :

$$\dot{\lambda} = \frac{\dot{W}^p}{\bar{\tau}_c} = \frac{\overline{\dot{W}^p}}{\bar{\tau}_c} = \sum_{i=1}^{I} C_i M_i^*(\underline{\dot{\varepsilon}}^p) \qquad (6\text{-}52)$$

where function M_i^* is computed from Taylor's factor and the harmonic function T_i.

The identification of the material parameters α_k, introduced in relation (6-50), directly results from the 2 expressions (6-52) and (6-50) of function $\dot{\lambda}$:

$$\alpha_k = \sum_{i=1}^{I} \beta_k^i C_i \quad k = 1,...,22 \qquad (6\text{-}53)$$

Arminjon *et al.* 1994 have found that, for a given i, the best approximation of coefficients β_k^i is based on a set of 16200 values of $\underline{\dot{\varepsilon}}^p$ and the comparison between:

$$M_i^{**}(\underline{\dot{\varepsilon}}^p) = \sum_{k=1}^{22} \beta_k^i \psi_k(\underline{\dot{\varepsilon}}^p) \quad \text{and} \quad M_i^{*}(\underline{\dot{\varepsilon}}^p)$$

Such computation is done only once with a Taylor's model and it has been checked that for steel texture, I =12 is enough. This fact means that the 22 coefficients α_k are not independent because relation (6-52) uses 13 coefficients to describe plastic dissipation (12 coefficients C_i and the value of τ).

The above process of parameters identification is independent of the C_i values and hence independent of texture. This is why it can be done only once.

The above explanations give the procedure to start from the choice of a scaled fourth order polynomial function $\dot{\lambda}(\underline{\dot{\varepsilon}}^p)$ and to finally provide an expression of this function as a linear relation of coefficients C_i. The same approach can be used if one choose $\dot{\lambda}$ as a second order polynomial function or Hill's yield locus. The application of this method will give a direct computation of 2nd order series or Hill's coefficient from C_i coefficients.

The validation of this approach can be checked on Figure 6-14 and Figure 6-15. Let us note that Figure 6-14 and Figure 6-16 give sections of the yield locus for $\sigma_{12}/\bar{\tau}_c$= 0, 0.5, 1 and 1.5 and, at the center, the value of $\sigma_{12}/\bar{\tau}_c$ for $\sigma_{11} = \sigma_{22} = 0$.

The above approach as well as Lequeu or Darrieulat's work compute an analytical yield locus from the initial texture. Figure 6-16 for steel I1 (Al killed) shows Lankford's coefficients and yield loci deduced from texture measurements in the initial state and after biaxial tension stopped at two different levels of deformation. In Figure 6-16, one observes that the effect of texture evolution cannot always be neglected. Imbault & Arminjon 1993 propose a semi-analytical method to take it into account in their analytical expression of the yield locus. In fact, the principle is simple. They assume that a linear operator, which is adjusted by comparison with a polycrystal model, can express the evolution with strain of the $C_l^{\mu\nu}$ coefficients from ODF. Of course, this linear operator depends on strain rate, which means that numerous strain rate tensors (1800) must be used to establish it. Once the $C_l^{\mu\nu}$ coefficients are known, the above identification process of the analytical expression for the yield locus can be activated.

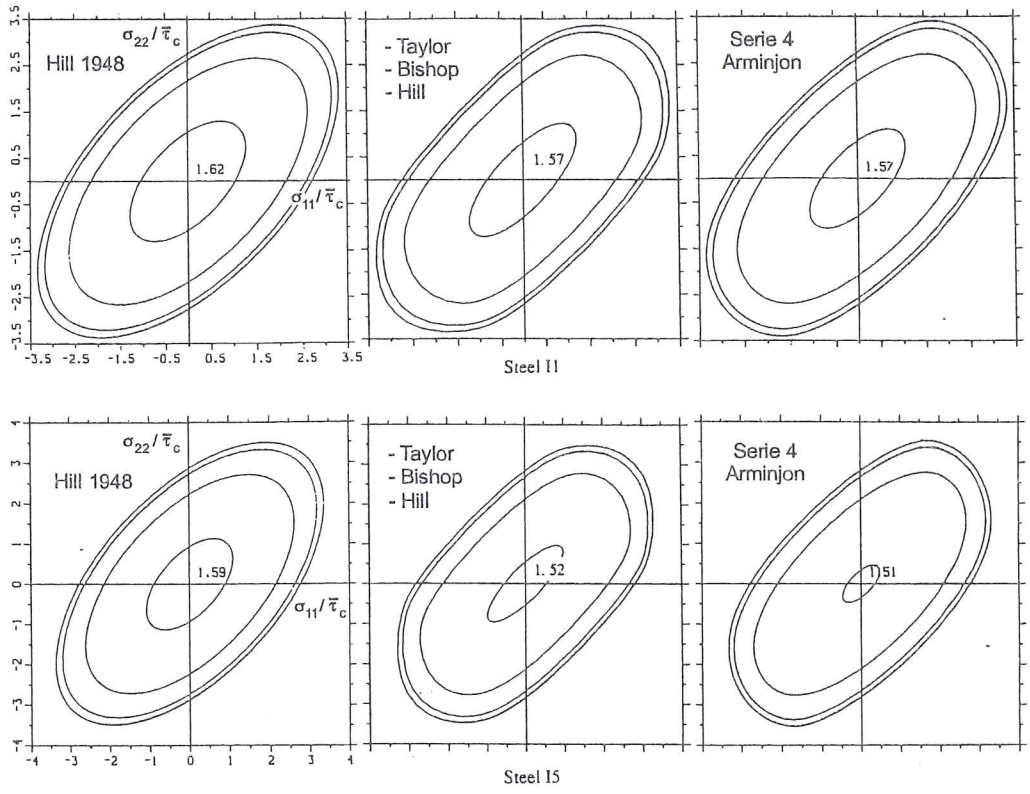

Figure 6-14 Yield locus sections computed by classical Hill's model, crystallographic Taylor-Bishop-Hill's model or Arminjon's 4th order series, for 2 industrial steels I1 (Al killed) and I5 (IF, Ti) (from Arminjon *et al.* 1994).

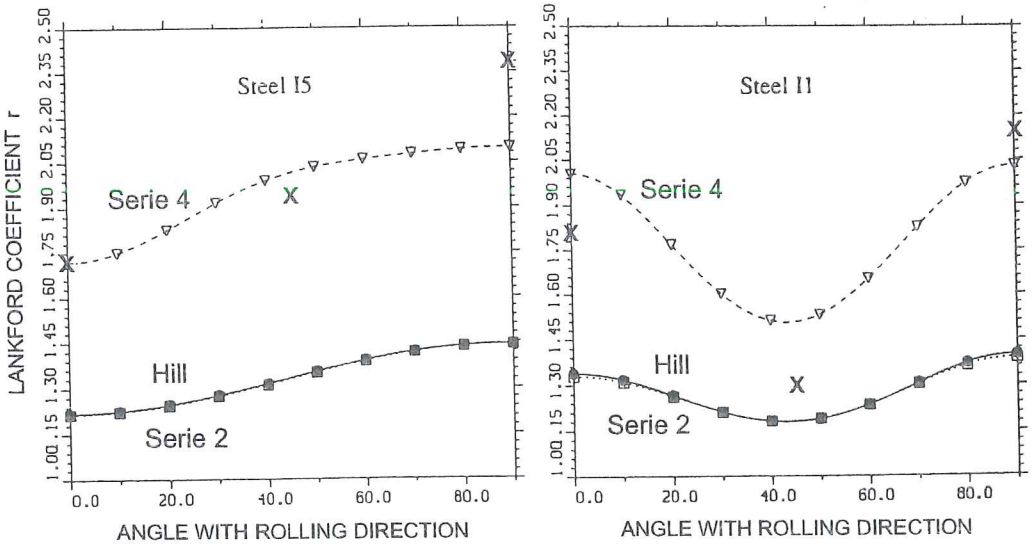

Figure 6-15 Measured (X) and computed Lankford's coefficients for 2 industrial steels I1 (Al killed) and I5 (IF, Ti) (from Arminjon *et al.*, 1994).

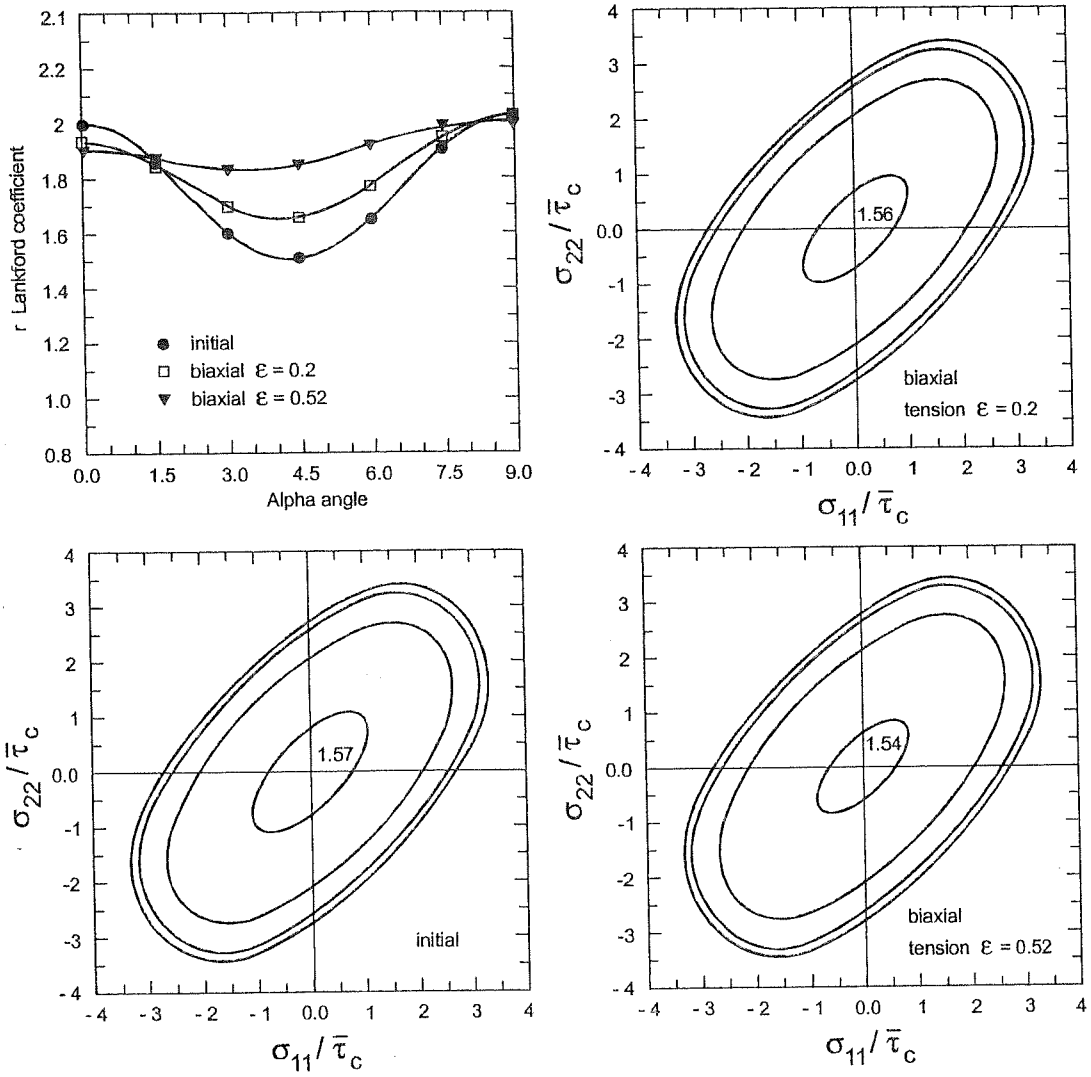

Figure 6-16 Lankford's coefficients and yield loci computed from texture measurements for a steel in its initial state and after biaxial tests performed up to 2 different levels (from Imbault & Arminjon 1993).

6.3.4. Van Houtte's potential formulation

As Arminjon, van Houtte 1994 uses the method of the dual plastic potentials to derive convenient formulae for calculating yield loci of rate insensitive anisotropic materials. In practice, the implementation in FEM code of such yield loci in strain space has been performed by one of his Ph.D. student, van Bael 1994, in collaboration with the university of Birmingham (Wang *et al.* 1989). The yield locus in stress space has been implemented in the LAGAMINE code by Winters 1996, another Ph.D. student in collaboration with MSM team (Munhoven *et al.* 1995a and b). Further developments such as the coupling with Teodosiu's hardening model (Hiwatashi *et al.* 1997) and the formulation in strain rate space in the LAGAMINE

code (Hoferlin *et al.* 1998, Hoferlin *et al.* 1999b) is described in details in Hoferlin's Ph.D. thesis (2001). The hereafter description summarizes van Houtte and co-workers' approach. It also explains what has been implemented in LAGAMINE code.

For rate-independent standard plasticity and formulation in strain rate space, the relation (6-43) computes the stress tensor:

$$\underline{\sigma} = \frac{\partial E}{\partial \underline{\dot{\varepsilon}}^p} = \frac{\partial \dot{W}^{p\,macro}}{\partial \underline{\dot{\varepsilon}}^p} \tag{6-54}$$

In practice, as already suggested by Lequeu *et al.* 1987, van Houtte's team works in the five dimensional space. The plastic strain rate is classically assumed to be deviatoric and only the deviatoric stress tensor matters with regard to plastic deformation (van Houtte *et al.* 1989). So, the tensors have only 5 independent components and are replaced by 5-dimensional vectors. This transformation, "tensor V_{ij}-vector v_p", can be defined in different ways. The version implemented in LAGAMINE by Winters 1996 assumes, as van Houtte 1988:

$$v_1 = \frac{1}{\sqrt{2}}(V_{11} - V_{22}) \qquad v_2 = \sqrt{\frac{3}{2}}(V_{11} + V_{22}) = -\sqrt{\frac{3}{2}}\,V_{33}$$

$$v_3 = \sqrt{2}\,V_{23} \qquad v_4 = \sqrt{2}\,V_{31} \qquad v_5 = \sqrt{2}\,V_{12} \tag{6-55}$$

This vector representation has the following property:

$$\underline{V} : \underline{W} = V_{ij}\,W_{ij} = \underline{v}.\underline{w} = v_p\,w_p \tag{6-56}$$

The vector forms of plastic strain rate and deviatoric stress tensors are respectively noted $\underline{\dot{e}}$ and $\underline{s}$ and their components $\dot{e}_p$ and s_p.

Using the potential relation (6-54), Taylor's hypothesis and micro-macro relations (4-33), (4-34), the deviatoric stress is computed by:

$$\underline{\hat{\sigma}} = \frac{\partial}{\partial \underline{\dot{\varepsilon}}^p}\left(\oint \dot{W}^{p\,micro}(\underline{\dot{\varepsilon}}^{p\,micro}, g)\,f(g)\,dg\right) = \frac{\partial}{\partial \underline{\dot{\varepsilon}}^p}\left(\dot{\varepsilon}_{eq}^{p\,macro}\,\overline{\tau}_c\,\overline{M}(\underline{U}_{\dot{\varepsilon}^p})\right) \tag{6-57a}$$

$$\underline{\hat{\sigma}} = \overline{\tau}_c \frac{\partial}{\partial \underline{\dot{\varepsilon}}^p}\left(\dot{\varepsilon}_{eq}^{p\,macro}\,\overline{M}(\underline{U}_{\dot{\varepsilon}^p})\right) \tag{6-57b}$$

where $\underline{U}_{\dot{\varepsilon}^p} = \underline{\dot{\varepsilon}}^{p\,macro} / \dot{\varepsilon}_{eq}^{p\,macro}$ is a strain mode as defined in Chapter 4. The relation (6-57b) assumes that the average CRSS is independent of further applied strain rate modes. It helps to understand how van Houtte and co-workers completely dissociate the size ($\overline{\tau}_c$) and the shape of the yield locus $\frac{\partial}{\partial \underline{\dot{\varepsilon}}^p}\left(\dot{\varepsilon}_{eq}^{p\,macro}\,\overline{M}(\underline{U}_{\dot{\varepsilon}^p})\right)$.

In practice, Winters 1996 proposes an isotropic hardening model. He updates $\bar{\tau}_c$ via a simple Swift's law (3-11) applied at the macroscopic stress strain level. The transfer to $\bar{\tau}_c(\bar{\Gamma})$ is based on the first term of the relation (4-40):

$$\frac{d\sigma}{d\varepsilon} = \bar{M}^2 \frac{d\bar{\tau}_c}{d\bar{\Gamma}} + \bar{\tau}_c \frac{d\bar{M}}{d\varepsilon} \tag{4-40}$$

where $\bar{\Gamma}$ is the total polycrystal slip. The stress σ and the strain ε are those of a uniaxial test. Neglecting the second term of (4-40) means that the texture evolution is dropped. This will be assumed in further developments, except when clearly specified.

Hiwatashi *et al.* 1997 applies a kinematic hardening assumption and slightly modifies the relation (6-57b) which becomes:

$$\underline{\hat{\sigma}} - \underline{\alpha} = \bar{\tau}_c \frac{\partial}{\partial \underline{\dot{\varepsilon}}^p} \left(\dot{\varepsilon}_{eq}^{p\,macro} \bar{M}(\underline{U}_{\dot{\varepsilon}^p}) \right) \tag{6-58}$$

where $\underline{\alpha}$ is the back-stress and defines the updated center of the yield locus. The evolutions of $\underline{\alpha}$ and $\bar{\tau}_c$ follow the model proposed by Teodosiu, already described in section 3.5.5.

The size and position of the yield locus being defined by the choice of the hardening model, what about its shape? Relation (6-57b) clearly shows the role of the texture via the average Taylor's factor $\bar{M}(\underline{U}_{\dot{\varepsilon}^p})$. $\underline{u}$ or u_p are the vector forms of this strain mode. The average Taylor's factor can be approximated by an analytical function $Q(u_p)$ of the components u_p:

$$\bar{M}(\underline{U}_{\dot{\varepsilon}^p}) = \bar{M}(\underline{u}) \approx Q(\underline{u}) = F_{p_1 p_2 p_3 \ldots p_N}\, u_{p_1} u_{p_2} u_{p_3} \ldots u_{p_N} \tag{6-59}$$
$$N = \text{order of series expansion} \qquad p_i = 1,\ldots 5 \quad i = 1,\ldots N$$

For instance, if N is reduced to 2, there are 15 coefficients:

$$Q(\underline{u}) = F_{11}u_1u_1 + F_{12}u_1u_2 + F_{13}u_1u_3 + F_{14}u_1u_4 + F_{15}u_1u_5 + F_{22}u_2u_2 \ldots + F_{55}u_5u_5 \tag{6-60}$$

van Bael 1994 has extensively described the symmetry properties of such an analytical expression, the main drawback of which is its lack of convexity. He explains that an odd order choice gives a non centro-symmetrical yield locus, which allows to model stress differential effects. It has been checked by van Bael *et al.* 1996 and Munhoven *et al.* 1997 that the 6th order is required to reproduce, with an analytical description, the accuracy of polycrystal approaches.

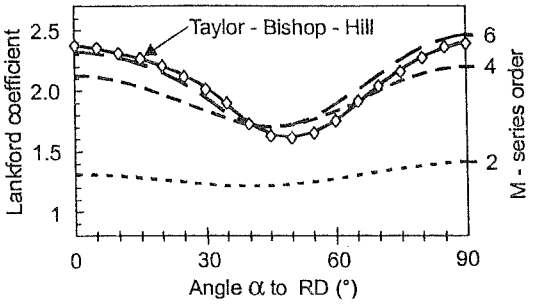

Figure 6-17 Lankford's coefficient of a classical interstitial steel computed by a polycrystal model or by means of 2nd, 4th, 6th order series in strain rate space (from Munhoven *et al.* 1997).

This choice of N=6 leads to 210 coefficients $F_{p_1 \cdots p_6}$. To identify them, it is interesting to note that any strain mode tensor can be represented by means of 4 independent parameters and not 5 because $\underline{U}_{\dot{\bar{\varepsilon}}^p} : \underline{U}_{\dot{\bar{\varepsilon}}^p} = \frac{3}{2}$. van Houtte 1994 demonstrates:

$$\underline{U}_{\dot{\bar{\varepsilon}}^p} = \begin{pmatrix} U_{11} & U_{12} & U_{13} \\ & U_{22} & U_{23} \\ \text{SYM} & & U_{33} \end{pmatrix} \qquad \underline{U}_{\dot{\bar{\varepsilon}}^p} = \underline{R}^T \underline{U}^X_{\dot{\bar{\varepsilon}}^p} \underline{R} \tag{6-61}$$

with :

$$\underline{R} = \underline{R}(\beta_1, \beta_2, \beta_3) \text{ and } (\beta_1, \beta_2, \beta_3) \in (0, 2\pi) \times (0, \pi/2) \times (0, \pi) \tag{6-62}$$

$$\underline{U}^X_{\dot{\bar{\varepsilon}}^p} = \begin{pmatrix} U^X_{11} & & \\ & U^X_{22} & \\ & & U^X_{33} \end{pmatrix} \text{ but } tr\left(\underline{U}^X_{\dot{\bar{\varepsilon}}^p}\right) = 0 \text{ and } \underline{U}^X_{\dot{\bar{\varepsilon}}^p} : \underline{U}^X_{\dot{\bar{\varepsilon}}^p} = \frac{3}{2} \tag{6-63}$$

$$U^X_{11} = \cos\left(\beta_4 - \tfrac{\pi}{3}\right), \quad U^X_{22} = \cos\left(\beta_4 + \tfrac{\pi}{3}\right), \quad U^X_{33} = -\cos\left(\beta_4\right) \tag{6-64}$$

The 3 Euler's angles $\beta_1, \beta_2, \beta_3$ define the orientation of the strain rate mode principal directions with respect to the sample reference system. The fourth angle gives the deviation of the current strain rate mode with respect to an axisymmetric compression along the third principal axis. Finally discrete variations of β_i, for instance $\Delta\beta_1 = \Delta\beta_2 = \Delta\beta_3 = 10°$ and $\Delta\beta_4 = 7.5°$ define a discrete set of strain rate modes (around 70300). The average Taylor factor is computed by the texture and crystalline approach (full Constrained Taylor-Bischop-Hill's model) for each of these modes. Then, the coefficients of the series expansion are provided by a least square fit of Q function (6-59).

Relation (6-57b) calculating the stress from the dissipation, is modified to take into account both the vector formulation and the analytical expression of the average Taylor's factor:

$$s_p = \bar{\tau}_c \frac{\partial\left(\dot{\varepsilon}^p_{eq}\, Q(\underline{u})\right)}{\partial \dot{e}_p} \tag{6-65}$$

In FEM, one usually needs the yield locus point corresponding to a given stress direction $\underline{s}^*$. So, Legendre's transformation must be applied. Let $s\underline{s}^*$ describe one stress vector belonging to the yield locus : the scalar factor s is the vector norm $\sqrt{s_p s_p}$ of the stress point, it is called stress radius, and $\underline{s}^*$ is its unit vector direction. Assuming that $\underline{u}$ is the strain rate mode associated with this stress direction $\underline{s}^*$ and using the average Taylor's factor definition, one gets :

$$\overline{M}(\underline{u}) = min_{\underline{u}'} \frac{s\,\underline{\underline{s}}^*}{\tau_c}.\underline{u}' = \text{minimum in strain rate space} \tag{6-66}$$

where $\underline{u}'$ represents all the possible strain modes of the strain rate space.
As $\underline{u}$ is actually unknown, one has to minimize the ratio:

$$\frac{s}{\tau_c} = min_{\underline{u}'} \frac{\overline{M}(\underline{u}')}{\underline{u}'\underline{s}^*} \tag{6-67a}$$

$$\frac{s}{\tau_c} = min_{\underline{u}'} \frac{Q(\underline{u}')}{\underline{u}'\underline{s}^*} \tag{6-67b}$$

The scaled factor $\bar{\tau}_c$ clearly shows that the shape does not depend on the size of the yield locus. If a formulation in strain rate space is adopted, $Q(\underline{u})$ is known and (6-67b) is used to perform the minimization. Figure 6-18 explains this procedure graphically. As reported above, the field of strain rate modes can be covered by 4 independent parameters, which limits the operation duration. Additionally, Hoferlin *et al.* 1999a propose a way to speed up significantly the minimization : with a BFGS type method instead of a classical Newton's method and by splitting the minimization process.

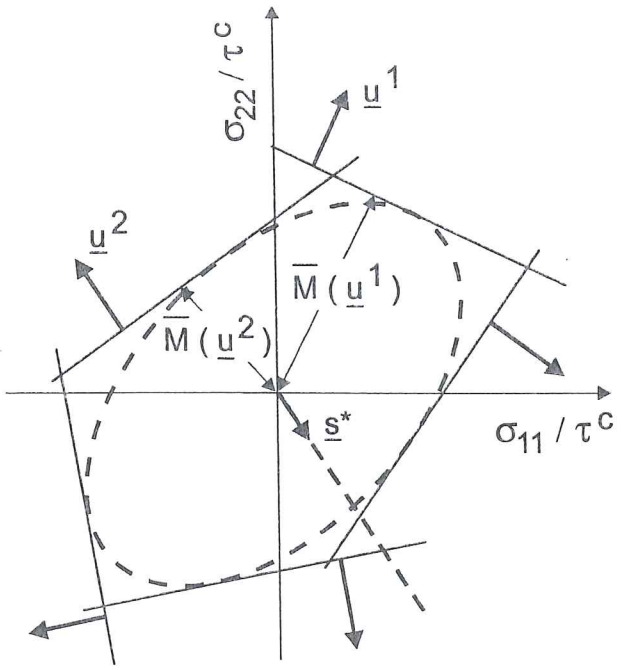

Figure 6-18 Graphical view of the minimization procedure to find a point on the yield locus (adapted from Hoferlin *et al.* 1999a).

As the convexity of the function $Q(\underline{u})$ in strain rate space is not perfect, gathering all stress points computed by (6-67b) does not produce a convex yield locus in stress space. Some fishtails appear as demonstrated by Figure 6-19. This drawing applies to an almost single f.c.c. crystal texture generated around the Goss' orientation (Gaussian distribution with 11° spread around (011)[100]). The left figure shows the π- section of one yield locus in strain rate space. For a pure single crystal, linear segments compose this locus. The series expansion reproduces linear segments by oscillating around them. The application of the minimization (6-67b) provides a yield locus in stress space with fishtails: see figure on the right.

Real materials generally present a less sharp texture; so their yield loci are smoother and the 4^{th} or 6^{th} order series expansions should be convex descriptions. However as non convex loci fail to bring convergence in FEM simulations, some secure approach should be implemented. Hoferlin's proposal consists in repeating the minimization (6-67b) with different starting guesses for $\underline{u}'$ and choosing the smallest result s, as the one giving the point on the yield locus. This procedure cuts off the fishtails and prevents convergence problems due to lack of convexity.

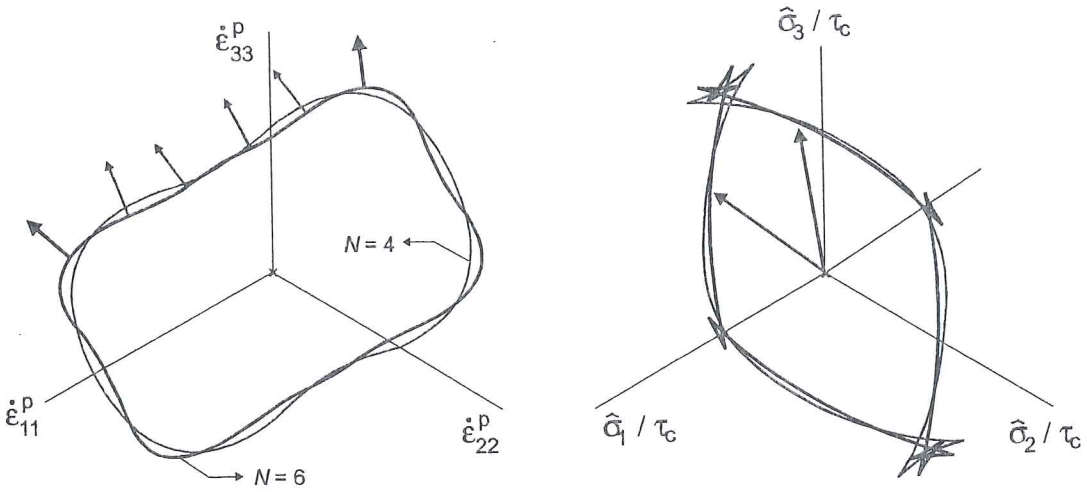

Figure 6-19 π-plane sections of the yield loci expressed in strain rate space (left) and in deviatoric stress space (right) for a f.c.c polycrystal with Goss' texture component (from Hoferlin *et al.* 1999a).

Another choice can be to implement an analytical yield locus in stress space, computed from texture and crystal plasticity approaches. The above presentation explains how to find points belonging to the yield locus. For a set of directions $\underline{s}^*$ in stress space, (6-67a) or (6-67b) provide the stress radius s. These two ways to obtain sets of yield points are not exactly equivalent.

The first way uses relation (6-67a), where $\overline{M}(\underline{u}')$ has no analytical expression and is computed for a certain number of strain rate modes. It is similar to the polycrystal method to get yield locus sections (see section 6.3.1.). By analogy, this method is called "geometrical approach". These yield points generally describe a nearly convex yield locus.

The second way uses relation (6-67b) and gives a set of points defining an approximate yield locus, not necessarily convex as shown by Figure 6-19.

In both cases, one has not yet reached an analytical yield formulation of the stress yield locus F_p. To reach this goal, one must fit an analytical function on these points. By analogy to the work in strain rate space, a series expansion is applied. Relations (6-68) and (6-69) present two possible choices:

$$\frac{s}{\tau_c} = Q(\underline{s}^*) \;\rightarrow\; F_p = \frac{s}{Q(\underline{s}^*)} - \tau_c = 0 \;\rightarrow\; u_p^* = \lambda \frac{\partial(s \,/\, Q(\underline{s}^*))}{\partial s_p^*} \qquad \text{(6-68a,b,c)}$$

$$\frac{s}{\tau_c} = \frac{1}{Q(\underline{s}^*)} \;\rightarrow\; F_p = sQ(\underline{s}^*) - \tau_c = 0 \;\rightarrow\; u_p^* = \lambda \frac{\partial(s\, Q(\underline{s}^*))}{\partial s_p^*} \qquad \text{(6-69a,b,c)}$$

where $\underline{u}^*$ is chosen as a unit vector. Its relation with the previous identification of the strain modes in vector form is $\underline{u}^* = \underline{u}/\sqrt{\underline{u}.\underline{u}}$. It defines the direction of the strain rate mode $\underline{u}$.
The third relations (6-68c), (6-69c) express a weak form of the normality rule in which the vector norms are not defined since both $\underline{s}^*$ and $\underline{u}^*$ are unit vectors. The scalar λ is computed to keep the norm of the strain rate mode tensor equal to unity.

In practice, Winters 1996 chooses (6-69) in order to use all the routines already developed to compute the formulation (6-65) in strain rate space. His function $Q(\underline{s}^*)$ is a 6^{th} order series expansion, the coefficients of which are fitted to the inverse of the stress radii:

$$Q(\underline{s}^*) = G_{p_1 p_2 \cdots p_N} s^*_{p_1} s^*_{p_2} \ldots s^*_{p_N} = \frac{\bar{\tau}_c}{s} \tag{6-70}$$

This set of points $\frac{\bar{\tau}_c}{s}$ is provided by the first way presented above. So, the yield locus will exhibit no fishtail. However as illustrated by figure 6-20, it must be observed that this yield locus in stress space is not completely convex. The locus on the left in strain rate space results from the approximation (6-59) in strain rate space while the one in stress space on the right is computed by (6-69b) and the first way to get the set of stress points.

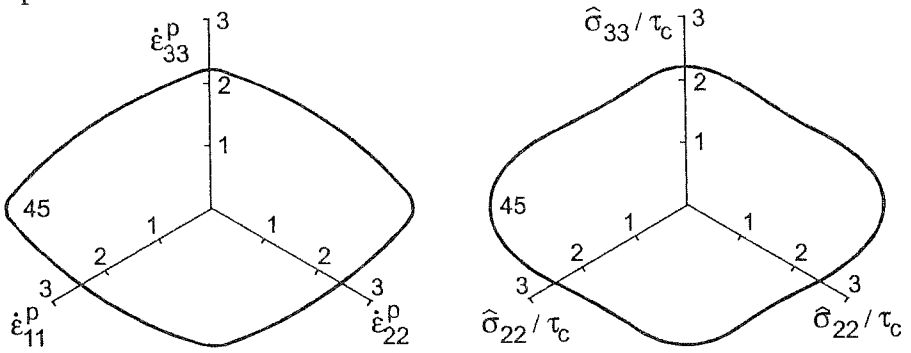

Figure 6-20 π-plane sections of the yield loci expressed in the strain rate space (left) and in deviatoric stress space (right), relative to a polycrystal with cube texture component and a Gaussian spreading of 16.5° (adapted from Winters 1996).

Further investigations have computed Lankford's coefficient: from (6-69) i.e. calculations in stress space, from (6-59) i.e. calculations in strain rate space and from Taylor-Bishop Hill's model. Both works from Winters 1996 and van Bael *et al.* 1996 reach the same conclusion that the yield locus in stress space is less accurate than the formulation in strain rate space.

Finally, is it better to use a formulation in strain rate or in stress space? The answer depends on your primary interest: accuracy, low CPU time, necessity of texture updating. Table 6-1 summarizes the advantages and drawbacks of each approach:

	Stress space $\frac{\underline{s}}{\bar{\tau}_c} = \frac{1}{Q(\underline{s}^*)}$	Strain-rate space $\dot{W}^p = \bar{\tau}_c \dot{\bar{\varepsilon}}^p_{eq} Q(\underline{u})$
Speed of FEM	faster	slower 4-dim. minimization
Texture evolution	Slower texture→ $\overline{M}$ → 4-dim. minimization→ Q	faster texture→ $\overline{M}$ → Q
Sharp textures	one stress direction →one stress point	one stress direction →fishtails (extra cost)
Accuracy	Lower	Higher

Table 6-1 Comparison between stress and strain rate formulations for analytical yield loci implemented in FEM codes (adapted from Hoferlin *et al.* 1999a).

Two points are completely missing in this description: the integration scheme and the numerical way to identify the position of material axes. Both are described in Winters 1996. For material axes, the solution proposed by Munhoven *et al.* 1995 is applied: each step is characterized by a constant local velocity gradient, which determines the evolution of material axes. This method has been described in part C, section 7.3.1 of this thesis. Another explanation of the same mathematical approach is proposed by Hoferlin *et al.* 1999b, using Ponthot's 1995 constant co-rotational strain rate tensor.

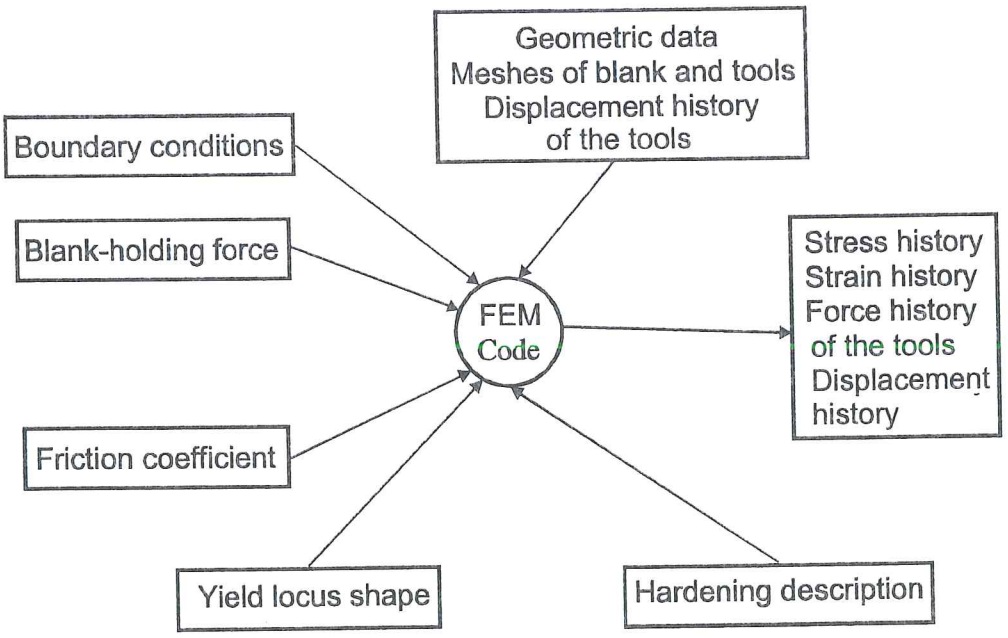

Figure 6-21 Schematic view of inputs and outputs of a FEM deep drawing simulation.

Figure 6-21 recalls the usual input and output of a FEM deep-drawing simulation when no texture updating is performed.

Figure 6-22 summarizes all the necessary steps to reach the yield locus shape expressed in stress or strain rate spaces.

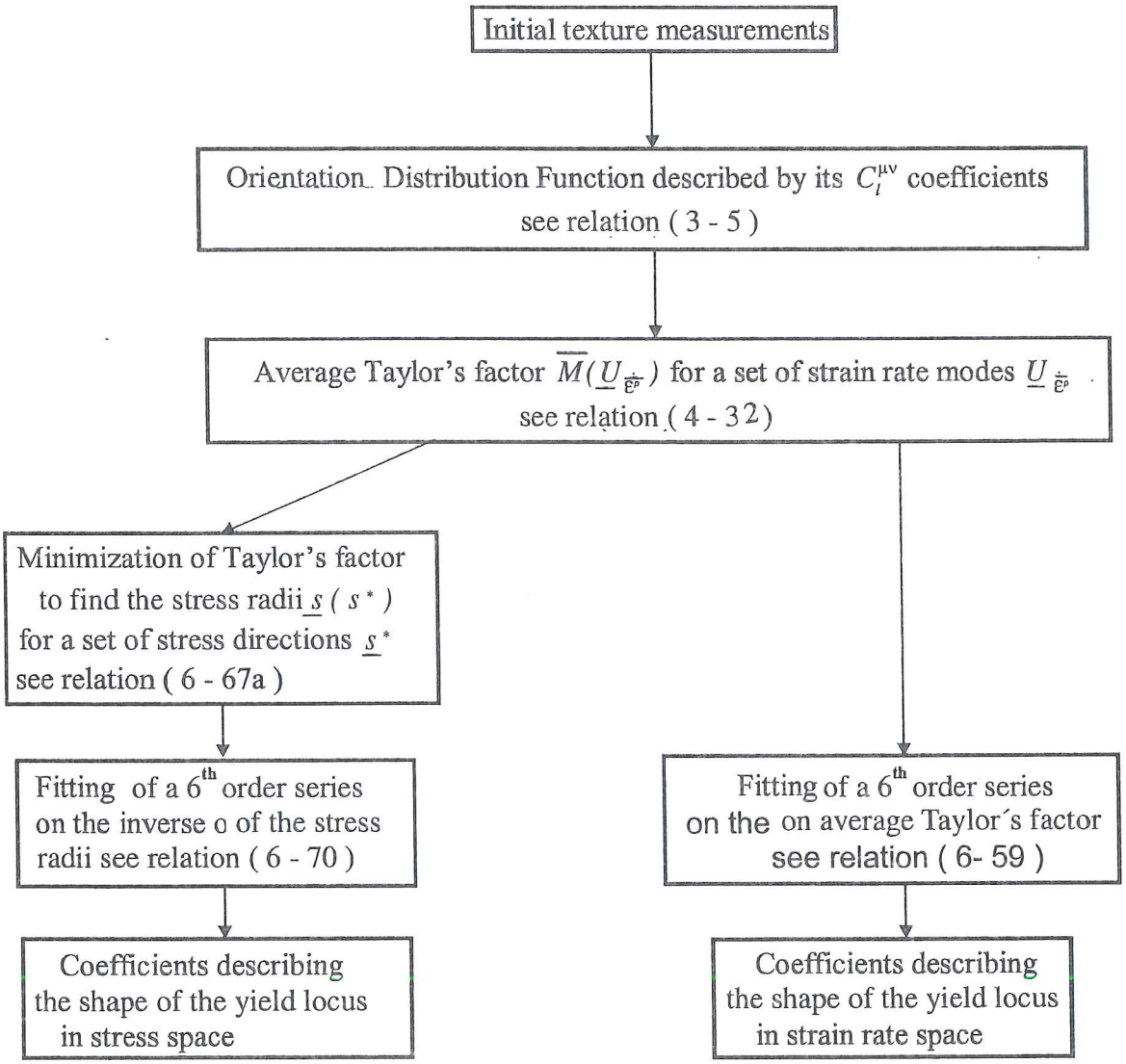

Figure 6-22 Successive operations to reach the shape description of the yield locus in stress or strain rate space.

6.3.5. Conclusion

Sections 6.3.2 to 6.3.4 propose models able to describe the behavior of real materials. They can be implemented in FEM codes and each one presents some advantages and drawbacks.

Darrieulat's micro-macro approach seems more accurate than Lequeu's. However, for real materials where important number of texture components are present, the FEM computations must be quite lengthy as their approach finally considers the yield locus associated to each component. Uniform stress approach must bring some difficulties in the FEM integration scheme.

The proposals from Arminjon, van Houtte and co-authors seem quite interesting. The identification of yield locus coefficients from texture coefficients can be optimized outside the FEM code. Taylor's assumption leads to a direct macroscopic stress-strain formulation.

Arminjon's semi-analytical method (shortly summarised at the end of section 6.3.3) to take texture updating into account is probably difficult to use for arbitrary velocity gradient. The approach proposed by Hoferlin (yield locus in strain rate space) seems more adapted in a FEM context. However, the CPU time is still important, as working in the strain rate space is slower than in stress space.

6.4. Models developed by MSM

6.4.1. First steps in coupling FEM with texture codes

Thanks to a collaboration with the team of Professor van Houtte, scientists of MSM department had, in 1995, the possibility to identify a 6^{th} order series describing a yield locus in stress space from the $C_l^{\mu\nu}$ coefficients of an ODF (see Figure 6-22). The constitutive law called "ANI3VH" (ANIsotropic 3 dimensions Van Houtte law) described by (6-69) and (6-70) was implemented in LAGAMINE. It allows to simulate deep drawing experiments (Munhoven *et al.* 1995a, Munhoven *et al.* 1995b, Munhoven *et al.* 1996b) such as cup-drawing and to predict the earing profile. The 6^{th} order polynomial series expansion defining the yield locus in the stress space is fitted once, from the initial ODF measurements and is not updated from the texture evolution. A simple isotropic hardening Swift's law (3-11) is applied at the microscopic level. This hardening law is fitted thanks to tensile test experiments and the micro-macro transition is done via (4-40) as explained in section 6.3.4.

From the collaboration with van Houtte's team, MSM department received a "Pascal version" of Taylor's model that allows texture evolution computations (see section 4.1). As inputs, such a module requires the initial texture approximated by a discrete set of orientations, the crystal slip systems identified by Schmid's tensors, the ratio between CRSS associated to slip systems and the macroscopic velocity gradient provided by the FEM analysis. With all these data, Taylor's model computes the updated crystal orientations, which can be used to retrieve the continuous ODF.

With these numerical tools, MSM team has simulated the experimental axi-symmetric deep drawing of a cold-rolled interstitial free steel sheet, described on Figure 6-23.

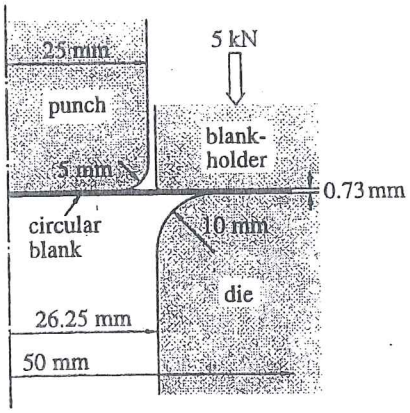

Figure 6-23 Radial section of the cup-drawing process
(from Munhoven *et al.* 1995a).

The elastic part of the deformation is assumed to follow the isotropic Hooke's law. The total strain rate is split into elastic and plastic parts and an integration scheme developed by Winters 1996 is applied. Taking advantage of the orthotropic symmetry of the blank material, only one quarter is simulated. A single layer of 8-node hexahedral solid elements is used; they are of the assumed strain family with one-point quadrature and hourglass control (Zhu & Cescotto 1996). Figure 6-24 shows the blank mesh with an indication about the positions of the tools.

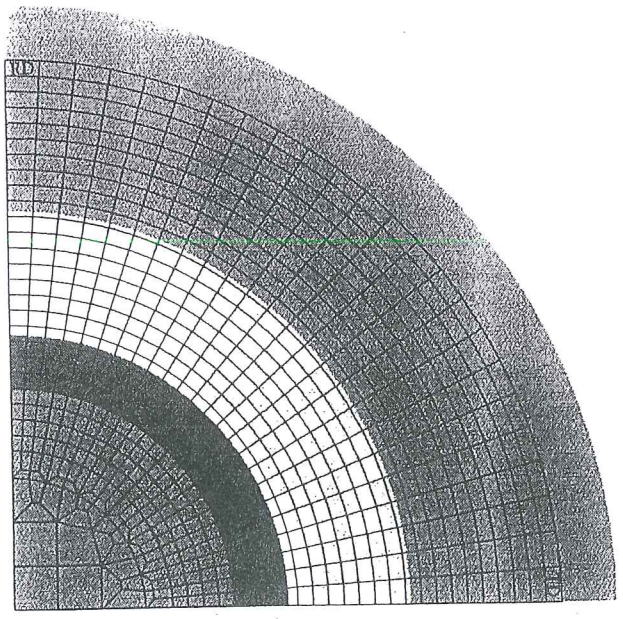

Figure 6-24 Discretization of the blank (656 elements, 1396 nodes) with an indication of tool positions (from Munhoven *et al.* 1996).

The die, punch and blank-holder are meshed by 1080 triangular elements and a Coulomb-type friction law (Charlier & Habraken 1990) is applied. The deformed mesh is presented on Figure 6-25, where the progressive earing of the drawn cup can be observed.

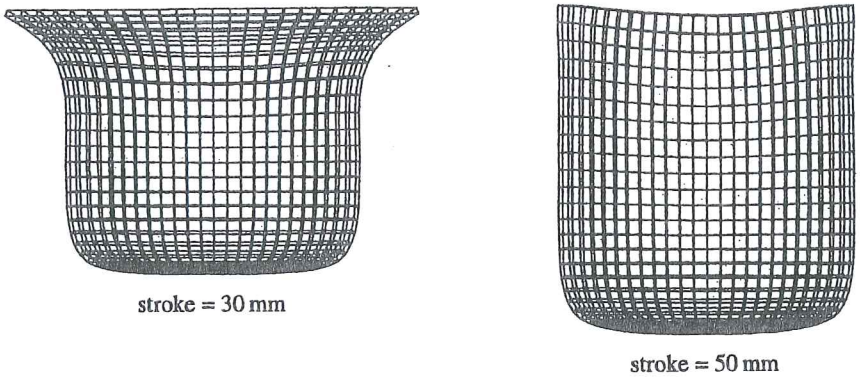

Figure 6-25 Orthogonal projections of the deformed mesh (from Munhoven *et al.* 1996).

The percentage of earing, defined as :

$$e = (h - h_{min}) / h_{min} \tag{6-71}$$

where h is the cup height depending on α angle with the initial rolling direction, and h_{min} is its minimal value, is plotted on Figure 6-26. Considering the absence of texture updating on the yield locus and the simple constant friction model, a quite good agreement is found.

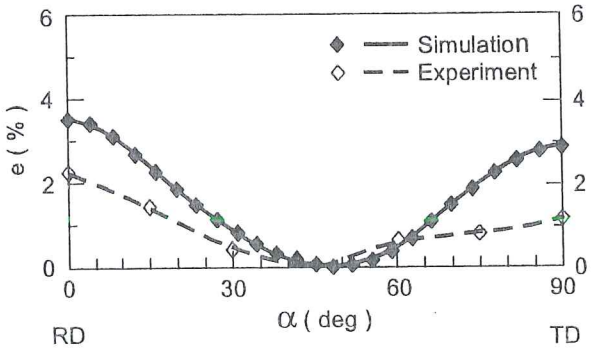

Figure 6-26 Simulated and experimental percentage of earing e (from Munhoven *et al.* 1996).

In general, a large portion of Euler's space angles (φ_1, ϕ, φ_2) has to be considered in order to get a correct idea of an ODF. In the present case, however, the symmetries of the material and the particular deformation history make a $\varphi_2 = \pi/4$ section very representative. Figure 6-27 a) shows some ideal texture features in such a plot. Comparison with Figure 6-27 b), corresponding to the cold-rolled steel before deep-

drawing, underscores the presence of a strong γ-fiber: many crystallites have a $\{1\,1\,1\}$ crystallographic plane parallel to the rolling plane, but no direction $\langle u\ v\ w\rangle$ within this plane has a preferential orientation.

After deep-drawing, samples are cut out of the cup at different positions and their textures are measured. Their texture evolution is also computed according to the FEM results using the "full constraints" Taylor's model of van Houtte, 1988. Experimental and numerical results are shown in Figure 6-27 c) to f) for two points (defined in Figure 6-24) near the cup rim, in the rolling (RD) and transverse direction (TD). In both cases, the initially strong γ-fiber has disappeared. Note that the texture sheet is measured at mid-thickness.

In RD, an *E*-component texture has appeared: $\{1\,1\,1\}$ planes are still parallel to the sheet-plane, but now direction $\langle 1\,1\,0\rangle$ has become strongly aligned with the initial RD. This evolution is typically observed in a plane strain situation, with elongation along RD and compression along TD. Since it is not exactly the case here, the texture peaks are slightly shifted away from *E*, as it appears in both experimental and simulated results. Considering that the "full constraints" Taylor's model typically produces too sharp textures, satisfactory agreement is found.

In TD, the situation is similar, except that radial flow now occurs in TD instead of RD. Up to a rotation of 90° around the vertical direction, results should thus be quite analog: an *F*-component texture with $\{1\,1\,1\}$ planes still parallel to the sheet plane is expected but, this time, with $\langle 1\,1\,2\rangle$ preferentially parallel to the initial RD. Again, up to a slight shift, this is obtained experimentally and numerically.

It is important to note that, in the present case, material flow is almost fully constrained. In addition, the rim ondulations are very small. As a consequence, the flow pattern does not dramatically depends on texture and corresponding evolution of the yield locus.

In order to progress in the development of a model in which texture updating is coupled with the FEM simulation, Munhoven has written a new version of Taylor's model in "Fortran 90", better adapted to be efficiently linked with the LAGAMINE code (Munhoven 1997, Habraken 1998a, Habraken 1998b). Taylor's factors associated with each crystal are the direct results of the simplex linear programming of Taylor's model (van Houtte 1988). They are combined to give the average Taylor's factor. Another interesting point is the fact that the simplex multipliers are none but the components of the five-dimensional vector representation of the crystal scaled deviatoric yield stress $s_p / \bar{\tau}_c$. The macroscopic stress is reached by averaging crystal stresses, weighted by the volume fraction associated with each crystal orientation (see relation (5-19)). It is important to note that, for b.c.c crystals and orthotropic sheets, a lot of symmetries are present. If one is interested in scalar values such as average Taylor's factor, one can choose a set of representative crystals

with Euler's angles $\varphi_1, \phi, \varphi_2$ in the reduced space of $[0°,90°]x[0°,90°]x[0°,90°]$. However, to reach tensor values such as macroscopic stresses, a less reduced space must be adopted: $[0°,360°]x[0°,90°]x[0°,90°]$ (Pospiech 1982). The new Fortran 90 module has been checked by comparisons with van Houtte's module and gives entire satisfaction (Habraken 1998a).

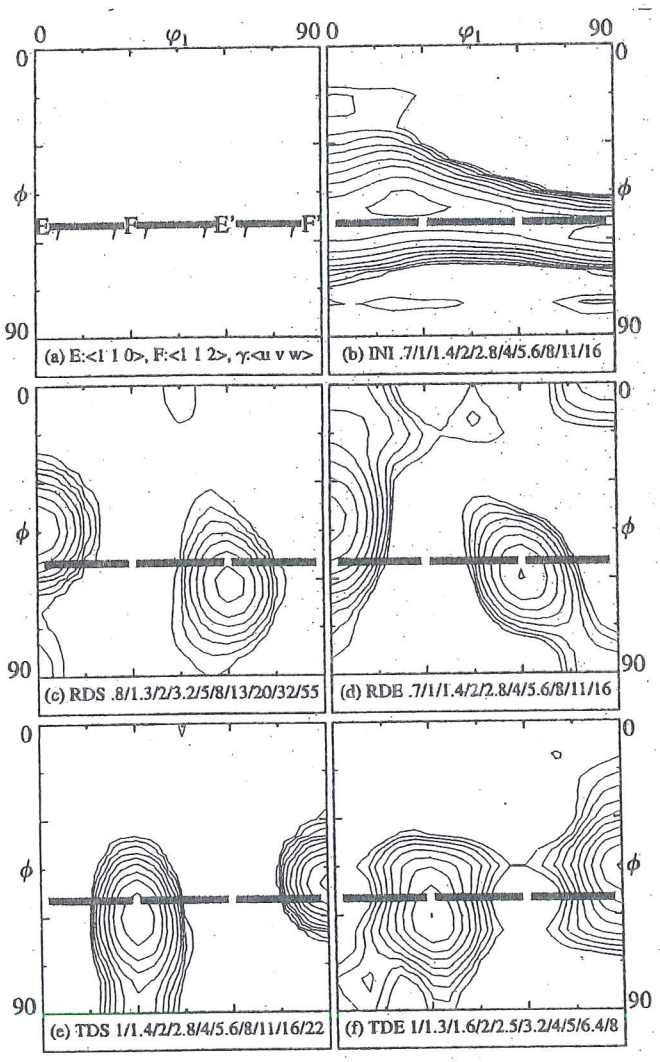

Figure 6-27 $\varphi_2 = 45°$ sections of Euler's space(from Munhoven *et al.* 1996).

a) some b.c.c. texture components:
$E = \{111\}\langle 110\rangle \quad F = \{111\}\langle 112\rangle \quad \gamma - fiber = \{111\}\langle uvw\rangle$
b) initial texture
c) simulated texture at RD point located in Figure 6-24
d) measured texture at RD point
e) simulated texture at TD point located in Figure 6-24
f) measured texture at TD point.

Figure 6-28 summarizes inputs and outputs of Taylor's module used by LAGAMINE.

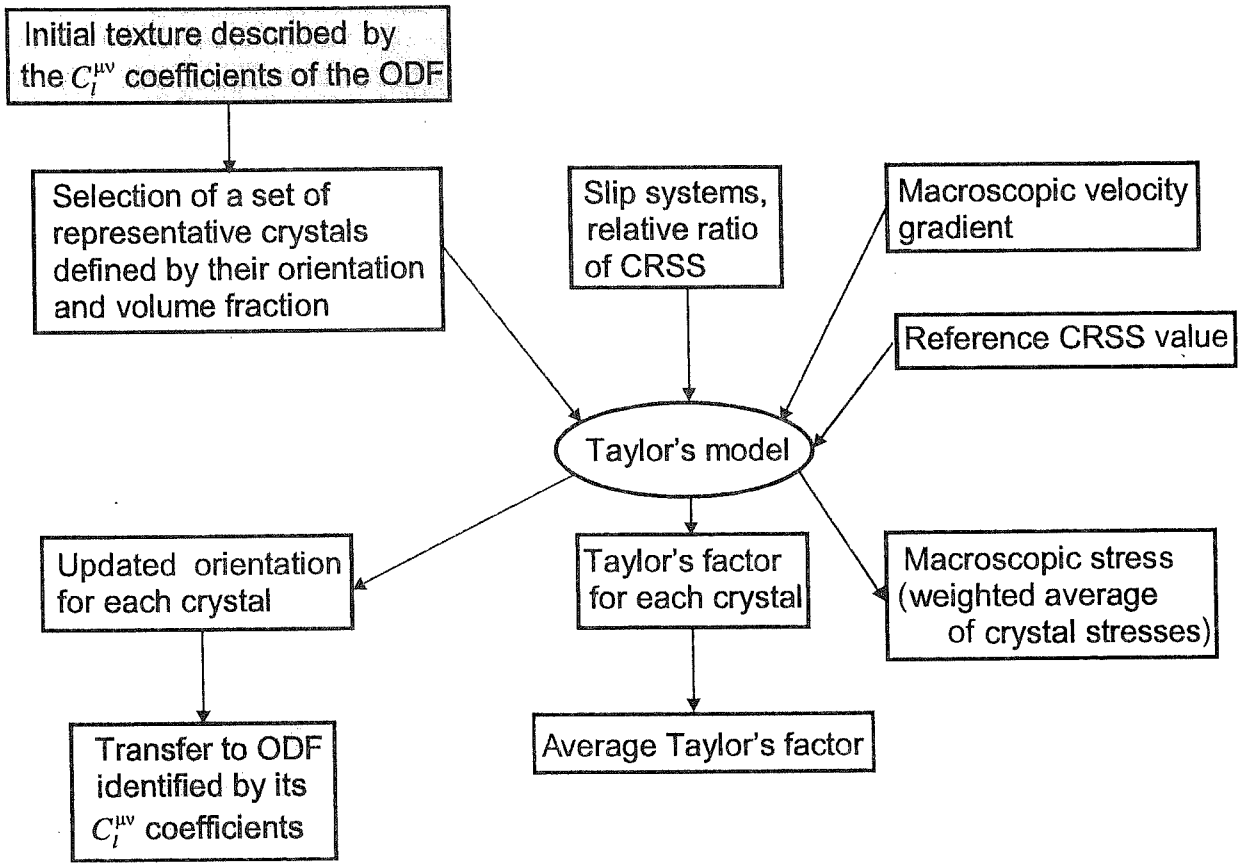

Figure 6-28 Texture updating by Taylor's model.

The "American way" of selecting a representative set of crystals has already been shortly described in section 5.3.1. However, here the approach called "STAT" from Tóth & van Houtte 1992 is applied. In practice, a 5°-grid in Euler' space is used to define N boxes in Euler' space. These boxes are given sequence numbers i ranging from 1 to N. Let us compute f_i the integral of the ODF in box i:

$$f_i = \int_{box\ i} f(g)\, dg \tag{6-72}$$

The property of the ODF yields:

$$\sum_{i=1}^{N} f_i = 1 \tag{6-73}$$

A kind of staircase function $F(j)$ is built with some smoothing between the steps:

$$F(j) = \sum_{i=1}^{j} f_i \tag{6-74}$$

If g_j represent Euler's angles at the center of box j, one can plot the diagram (g_j, F_j) in Figure 6-29.

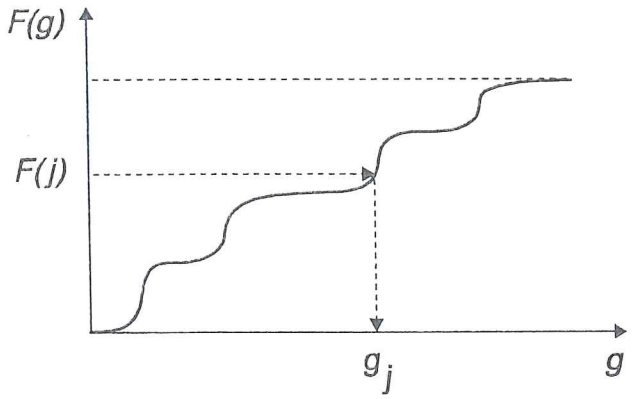

Figure 6-29 Staircase function of crystal orientation (adapted from Tóth & van Houtte 1992).

To discretize the ODF, a set of n numbers s_k, called selectors, is generated in the range $[0,1]$. They represent points of the vertical axis. By inverting function $F(g)$, one reaches, on the horizontal axis, the orientation g_k or the box k associated to s_k. The selectors s_k have a uniform probability distribution. The probability $p(i)$ of selecting a particular box i is f_i. Further details on the statistical properties of the STAT method are given in Tóth & van Houtte 1992.

In Degueldre *et al.* 1996, my co-workers and myself have applied the texture prediction module to an experiment of aluminium extrusion shown on Figure 6-30 and performed by the R&D Center of Hydro Aluminum in Norway.

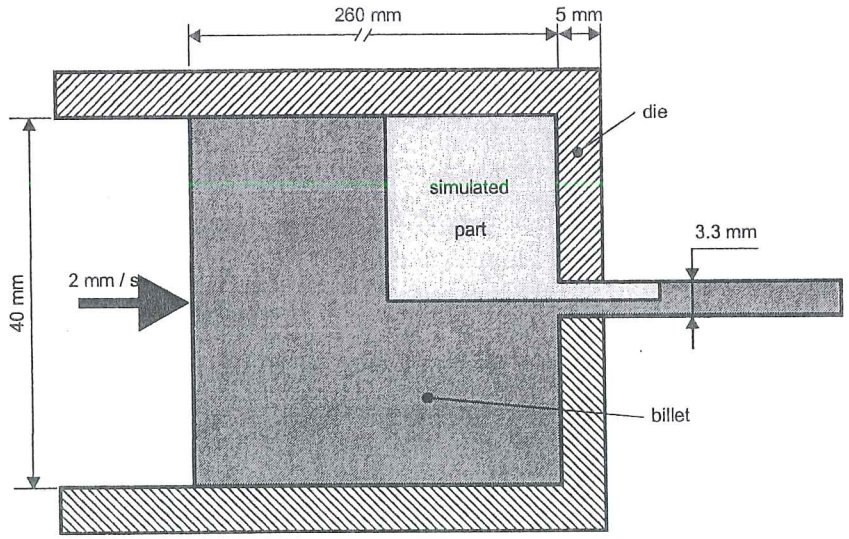

Figure 6-30 Cross section of the experimental set up (plane extrusion), adapted from Aukrust *et al.* 1994.

As the LAGAMINE code is Lagrangian, an automatic remeshing procedure (Dyduch *et al.* 1995) has been applied and the process is simulated until stationary conditions are reached. Three successive meshes are presented on Figure 6-31.

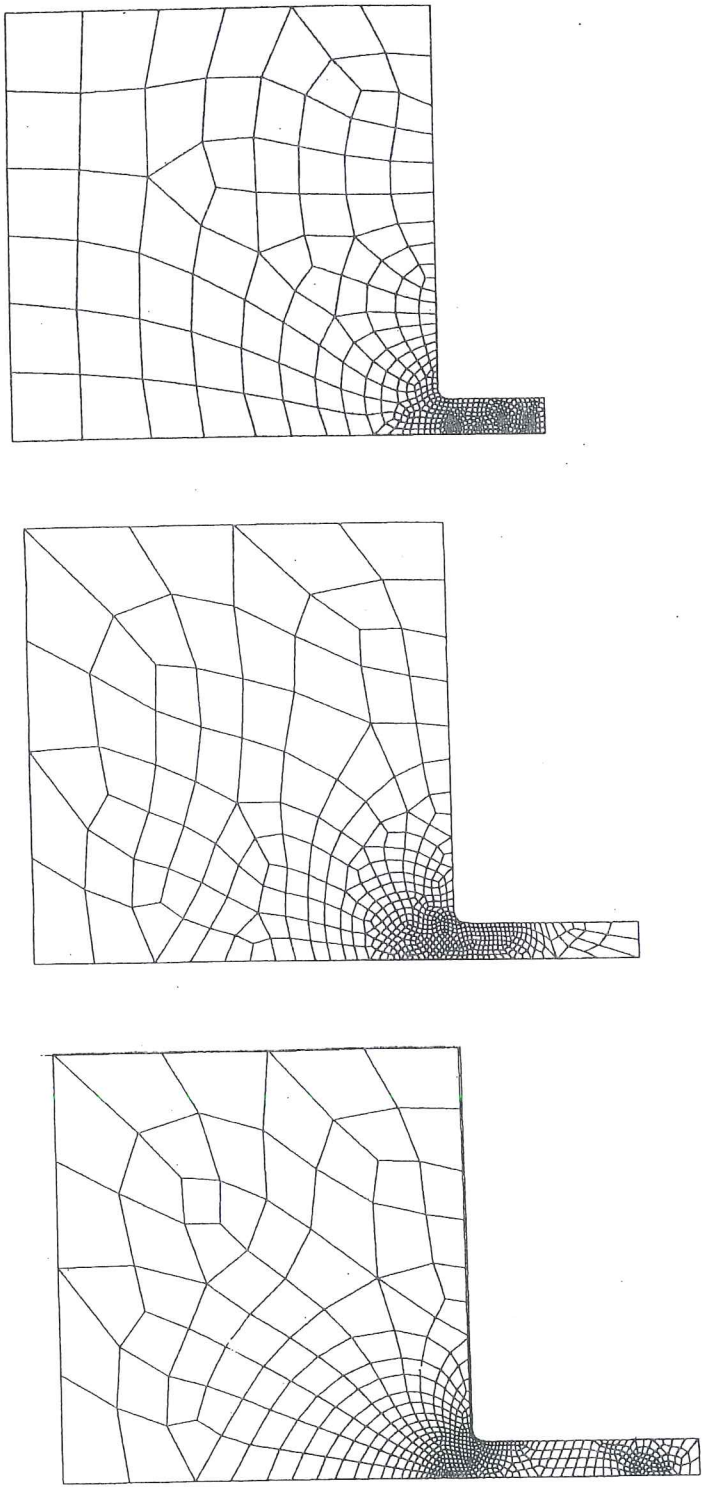

Figure 6-31 Three successive meshes in the extrusion simulation.

A macroscopic elasto-visco-plastic law (Cescotto et Grober, 1985) represents the isotropic behavior of the hot material. The experimental boundary conditions and particularly the friction coefficient to be used in Coulomb's friction model were not clearly identified. So, depending on contact conditions (case A or B) and on small variations of the parameters of the elasto-visco-plastic law (law 1 or 3), different velocity fields were computed. The material strain history was extracted from the FEM results thanks to a special post processing (Munhoven 1996) and used as data for Taylor's model. The material initial texture was isotropic and, after extrusion, different textures were observed according to the vertical position in the extruded section. The coordinate S identifies this location: $S=0$ at the center and $S=1$ at the surface. Figure 6-32 presents pole figures at the center and near the surface of the extruded section. The results, produced by the measurements, by a Norwegian team (Aukrust *et al.* 1997) using a FEM Eulerian code with Full Constraints (FC) or Relaxed Constraints (RC) Taylor's model and by our group, are plotted in Figure 6-32.

A good agreement is found at the center, while predictions close to the surface appear to be highly sensitive to simulation conditions. Comparisons of velocity fields near the surface also show a lot of scatter, depending on boundary conditions, material parameters and FEM codes. So it is not surprising that textures computed from these different strain histories vary.

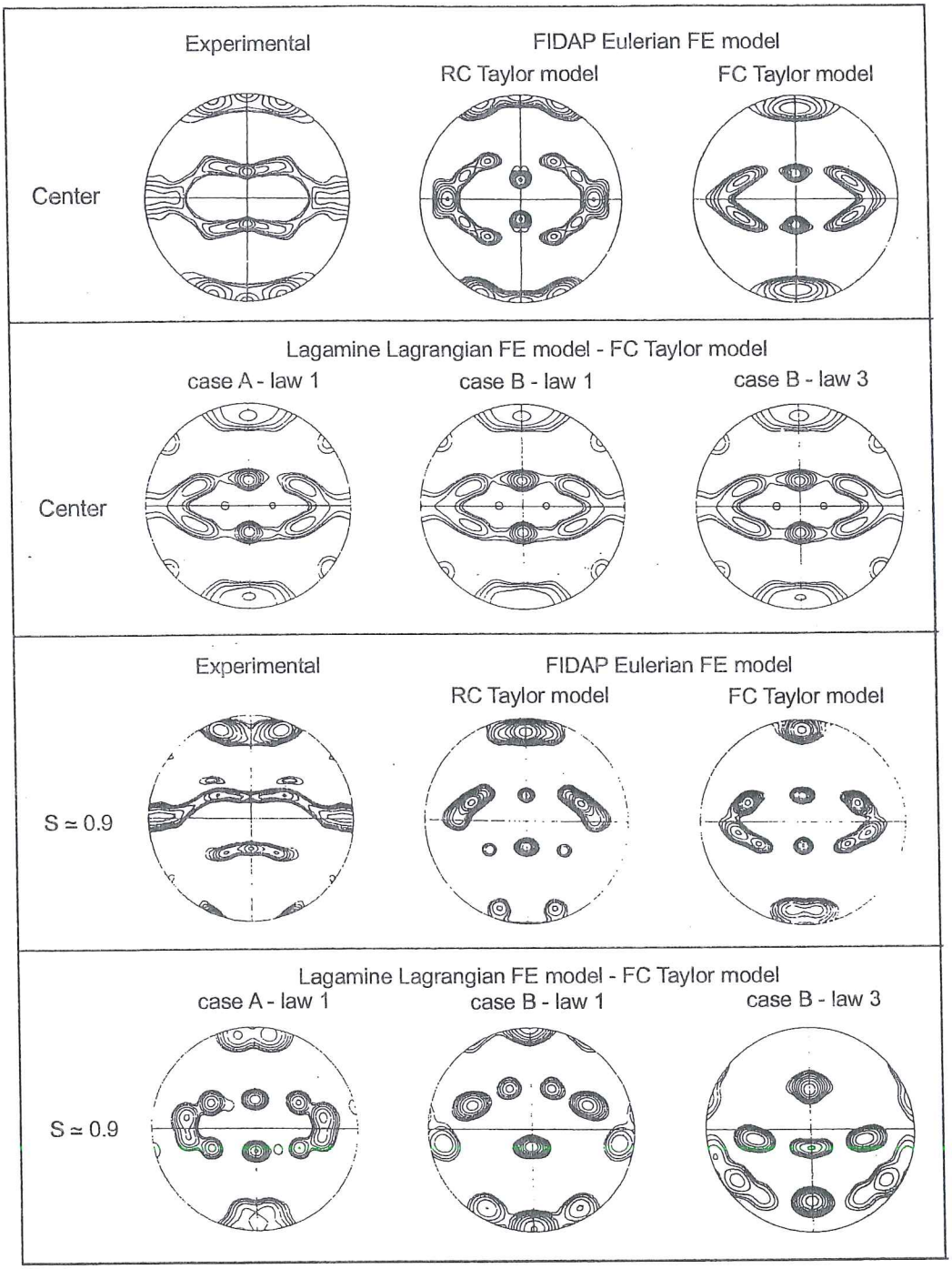

Figure 6-32 $\{111\}$ pole figures at the center and near the surface of the extruded section (from Degueldre *et al.* 1996).

6.4.2. Texture updating coupled with FEM simulations

As verified by Figure 6-27 and Figure 6-32, the texture evolution during a forming process is not always negligible. Material properties such as Lankford's coefficients and the yield locus computed from texture measurements before and after biaxial tension show a clear evolution (see Figure 6-16). So, to obtain FEM simulations that

really represent the material behavior during forming processes, it is interesting to couple a FEM code using a yield locus based on texture and a texture prediction module.

One possible global scheme is described by Figure 6-33. In this approach, every Interpolation Point of each finite element is associated with a representative set of crystal orientations. One yield locus in stress space is computed by a "Micro-Macro transition" as summarized by Figure 6-22. Then, the FEM code is run for a chosen number of loading steps and it computes the macroscopic velocity gradient that feeds a texture prediction module (Taylor's model). This module provides the updated orientations of the set of representative crystal orientations and the loop goes on.

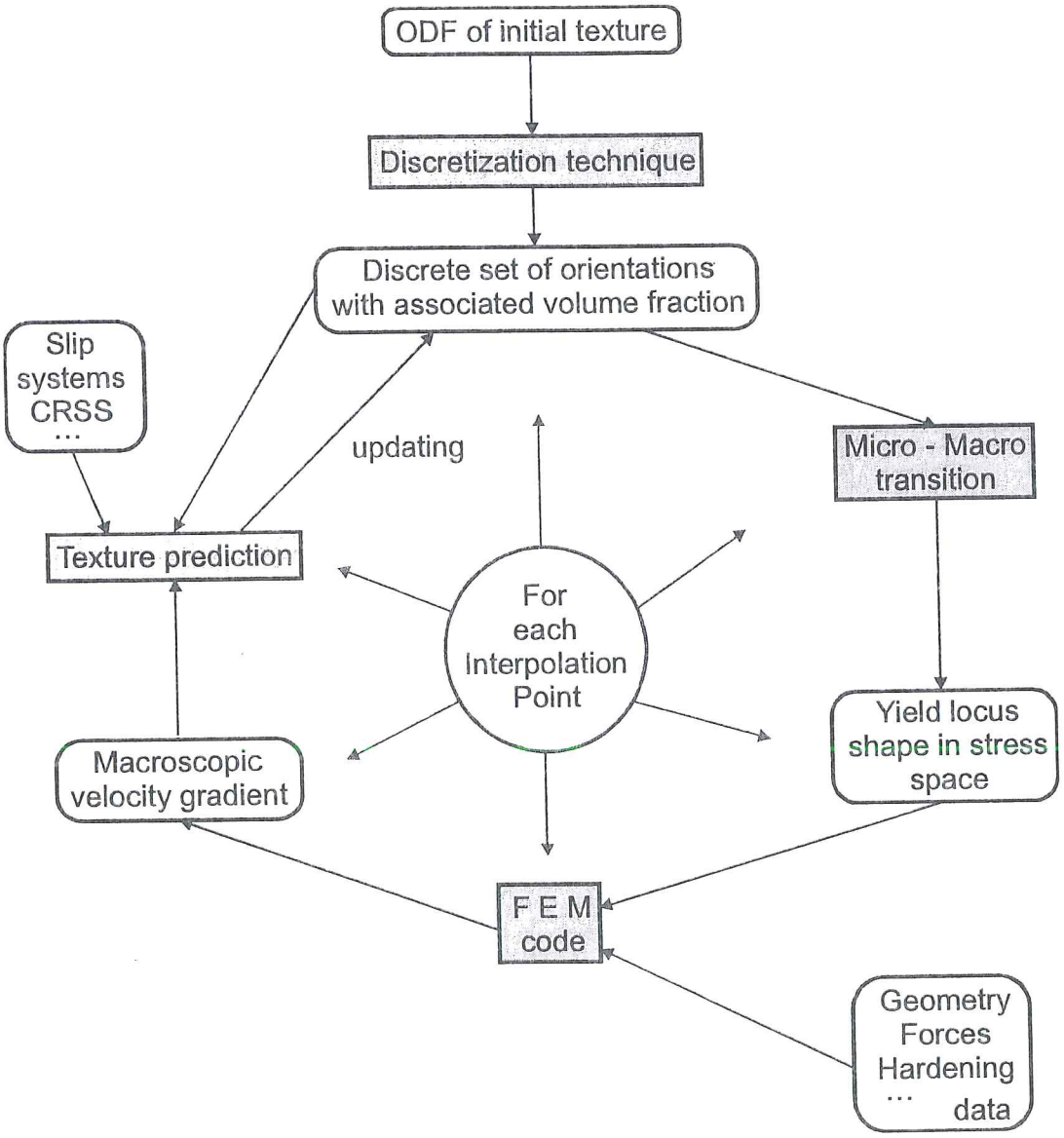

Figure 6-33 Complete flowchart for coupling yield locus and crystallographic texture.

Does such a scheme bring any economy compared with the simulations without yield locus presented in section 5.3?

Concerning memory requirement, certainly not. There are not only the parameters describing the set of representative crystals for each interpolation point to be stored but, in addition, the coefficients describing the shape of the yield locus.

Concerning CPU time, probably yes... In fact, in the models of section 5.3, Taylor's model is called each time the stress must be computed that is at each iteration of each loading step. In Figure 6-33, Taylor's model is called after a "few steps", when the strain history produces a significant texture evolution. If these "few steps" are reduced to one, the economy resulting of the proposal on Figure 6-33 is reduced but still exists: there is only one Taylor's call per step, after convergence of the equilibrium iterations. However, this advantage is counterbalanced by all the computations needed in the "Micro-Macro transition" box. If an important number of steps can be done between the phase of texture updating, the model described by Figure 6-33 is certainly more economical. So, a key point should be to find a criterion based on strain history to determine when a texture updating is necessary.

Other tracks can be studied to reduce CPU time of the coupling scheme on Figure 6-33. For instance, Hoferlin *et al.* 1999a and b prefer to use the yield locus in strain rate space instead of the one in stress space. They assume that the fact that this approach slows down the FEM code is compensated by a quicker identification of the shape of the yield locus from texture data. This choice should also increase accuracy.

As already summarized in the introduction (section 6.1), Cescotto, Munhoven, Radu and Habraken (MSM team) have chosen to use an incomplete yield locus, called "local yield locus zone", determined by only 5 or 6 calls to Taylor's model. This strongly reduces the time spent in the "Micro-Macro transition" box. Recall that, for the general case, 70300 Taylor's factors are computed in Figure 6-22. However, it increases the FEM computation time, because, sometimes during the simulation, the known part of the yield locus must be updated by means of additional calls to Taylor's model.

The implementation of the scheme on Figure 6-33 in the LAGAMINE environment is based on compatible software modules. So, if some day, one wants to replace Taylor's model by a self-consistent model, the rest of the coupling approach will not be modified.

The idea of a "local yield locus zone" and a long practice of the finite element discretization approach have first resulted in a discretized portion of the yield surface in stress space by hyperplanes. This discontinuous model introduces a lot of convergence difficulties and is now forgotten. It is however described in section 6.4.3 as it allows to identify the important properties of a local model description. The second approach, presented in section 6.4.4, gives entire satisfaction. It is rather

an interpolation scheme than a yield locus approach. However, such an interpolation is based on the existence of a yield locus in strain or stress space.

6.4.3. Hyperplane model

This model developed in 1996 and 1997 is described in reports of a Région Wallonne project (Habraken & Munhoven 1996, Radu *et al.* 1997, Habraken & Radu 1997). A lot of improvements have been implemented by Duchêne (Duchêne 1998a, b, c).

A. Principles

As in van Houtte's approach explained in section 6.3.4, this approach dissociates the shape and the size of the yield locus. The vector representation of deviatoric tensors described by (6-55) is applied and the same notations are adopted:

$\underline{s}$	vector form of $\hat{\underline{\sigma}}$, the deviatoric stress tensor, defined by its components s_p,
s	size of the stress vector, computed by $\sqrt{s_p s_p}$,
$\underline{s}^*$	unit vector, direction of the stress vector, computed by $\underline{s}/s$.

Concerning the strain rate tensor $\dot{\underline{\varepsilon}}^p$, the strain rate mode $\underline{U}_{\dot{\varepsilon}^p} = \dot{\underline{\varepsilon}}^p / \dot{\varepsilon}^p_{eq}$ and its vector form $\underline{u}$ or components u_p introduce scalar coefficients 3/2 in the formulation. So the unit vector form $\underline{u}^*$ is preferred to describe the strain rate direction, with its components u^*_p.

The chosen definition of the yield function is very close to (6-69) but is slightly different. It is:

$$F_p = \frac{s}{\tau_c} Q(\underline{s}^*) - 1 = 0 \qquad (6\text{-}75)$$

However here, no complete analytical function exists for $Q(\underline{s}^*)$, only a local discretization is available.

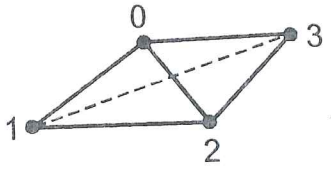

Figure 6-34 Approximation in 3 dimensional space *X, Y, Z* by 3 triangular facets of a surface described by a central point *0* and 3 neighbor points *1, 2, 3* from Habraken & Munhoven 1996.

In three dimensions, triangular plane facets are the simplest discretization of complex surfaces. For instance, if a surface must be described around a central point *0*, three triangular facets *(0,1,2; 0,2,3; 0,1,3)* defined on 3 neighbor points *1, 2, 3* belonging also to the surface, approximate the surface. This is shown by Figure 6-34.

Each triangle can be described by the isoparametric concept recalled on Figure 6-35:

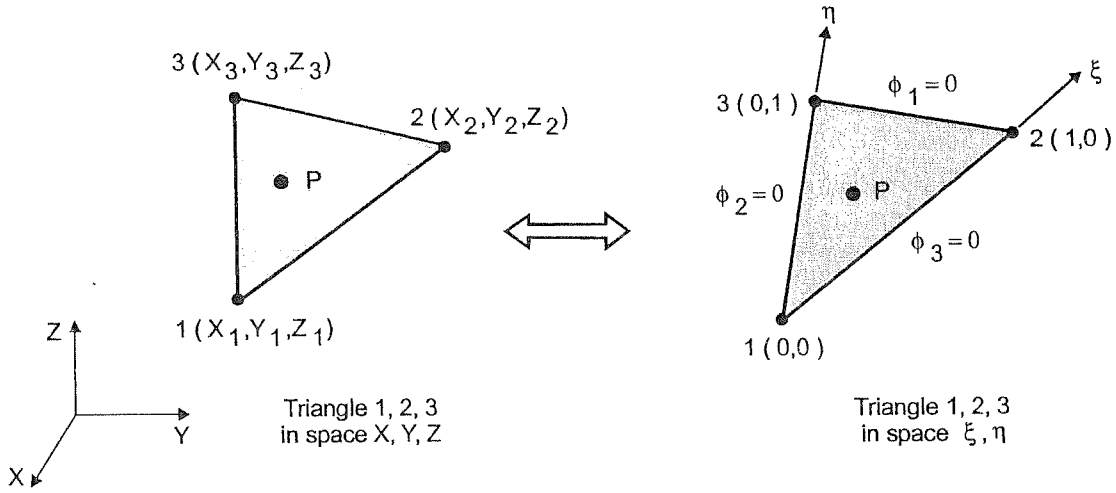

Figure 6-35 Concept of isoparametric triangle, adapted from Habraken and Munhoven 1996.

Each point *P*, defined by its coordinates X_P, Y_P, Z_P inside the triangle *1, 2, 3*, is associated with isoparametric coordinates ξ,η in the range $[0,1]$. These coordinates follow the relation:

$$\begin{Bmatrix} X_P \\ Y_P \\ Z_P \end{Bmatrix} = \sum_{i=1}^{3} \Phi_i(\xi,\eta) \begin{Bmatrix} X_i \\ Y_i \\ Z_i \end{Bmatrix} \tag{6-76}$$

where interpolation functions are introduced:

$$\Phi_1 = 1-\xi-\eta; \quad \Phi_2 = \xi; \quad \Phi_3 = \eta \tag{6-77}$$

The nodal points 1,2,3 are characterized by isoparametric coordinates equal to 0 or 1, and the edges 12, 23, 31 respectively correspond to $\Phi_3 = 0, \Phi_1 = 0, \Phi_2 = 0$.

The above concept, described in a three-dimensional space, is applied to the five-dimensional space related to the five components of the vector representation of deviatoric stress tensors. Six points belong to the stress yield locus: the central point *0* surrounded by five neighbors *1,2,3,4,5*. This local part of the yield locus is approximated by five hyperplane facets built on the central point and four neighbor points: *(0 1 2 3 4), (0 2 3 4 5), (0 1 3 4 5), (0 1 2 4 5), (0 1 2 3 5)*. The coordinates of

a point belonging to a hyperplane facet is computed by a relation analogous to (6-76):

$$s_p = \sum_{k=1}^{5} \Phi_k s_p^{(k)} \text{ with } p = 1,5 \tag{6-78}$$

where $s_p^{(k)}$ is the p^{th} component of the (stress) nodal point number k that determines the hyperplane facet. The interpolation functions are:

$$\Phi_1 = 1 - \xi_1 - \xi_2 - \xi_3 - \xi_4 \quad \Phi_2 = \xi_1$$

$$\Phi_3 = \xi_2 \quad \Phi_4 = \xi_3 \quad \Phi_5 = \xi_4 \tag{6-79}$$

This approximation by hyperplane facets can only be accurate if the six points are quite close to each other. The five neighbor points must really surround the central point *0*. For instance, a good and a bad configuration are shown in three-dimensional space on Figure 6-36.

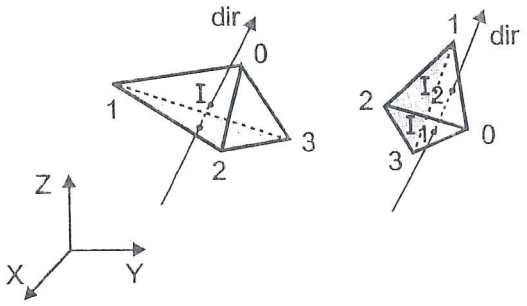

Figure 6-36 Disposition of surrounding points around central point in three-dimensional case, adapted from Radu *et al.* 1997.

Let *dir* define a direction for which the intersection *I* with the discretized surface is required. On the left of Figure 6-36, this direction first intersects the triangle *123*, which does not belong to the discretized surface but constitutes the base of the tetrahedral volume the other faces of which approximate the surface. Then, *dir* intersects only one triangle facet of the approximated surface and gives the requested point *I*. On the right of Figure 6-36, *dir* intersects 2 such facets and not the base triangle. The points I_1, I_2 are 2 potential solutions, which proves a bad approximation of the real surface.

So, transposed into the five-dimensional stress space, the set of five hyperplane facets built on the six points *0,1,2,3,4,5* must give only one intersection in one direction $\underline{s}^* = \underline{s}/\bar{\tau}_c$. In practice, the following method allows to define six points, well distributed in stress space. The plastic strain rate direction $\underline{u}^*$ associated with the central point *0* is assumed to be known. Let $\underline{a}$ be a vector and $\underline{v}$ its associate unit vector such as:

$$\underline{a} = (11111) \quad \underline{v} = \underline{a}/\sqrt{a_i a_i} \tag{6-80}$$

The perturbated vectors $\underline{a}^{(i)}$ and $\underline{v}^{(i)}$ are computed by:

$$\begin{aligned}\underline{a}^{(1)} &= \underline{v} + \beta(10000)\\ \underline{a}^{(2)} &= \underline{v} + \beta(01000)\\ \underline{a}^{(3)} &= \underline{v} + \beta(00100)\\ \underline{a}^{(4)} &= \underline{v} + \beta(00010)\\ \underline{a}^{(5)} &= \underline{v} + \beta(00001)\end{aligned} \tag{6-81}$$

$$\underline{v}^{(i)} = \underline{a}^{(i)} / \sqrt{a_p^{(i)} a_p^{(i)}} \quad \text{with no summation on } (i) \tag{6-82}$$

with β a parameter to be defined. Somehow it is a measure of the size of the local yield locus zone. Let $\underline{R}$ be the rotation matrix linking the plastic strain rate direction $\underline{u}^*$ and vector $\underline{v}$:

$$\underline{u}^* = \underline{R}\,\underline{v} \tag{6-83}$$

This matrix is used to find $\underline{u}^{*(i)}$:

$$\underline{u}^{*(i)} = \underline{R}\,\underline{v}^{(i)} \qquad i = 1,5 \tag{6-84}$$

which constitute five perturbations of $\underline{u}^*$. Then, Taylor's module, described on Figure 6-28, computes the stress points associated with $\underline{u}^*$ and its five perturbations $\underline{u}^{*(i)}$.

According to the idea of an associate plasticity model, using five hyperplane facets to approximate the yield locus should give five discrete values for the associate normals or plastic strain rate but undetermined normals at the hyperplane intersections. To try to increase the accuracy of the model and to prevent indetermination, it was decided to interpolate the normals separately. So, the hyperplane model is a non associate plasticity model. This aspect of the computation is now described. At a given instant of the FEM computation, for example during an equilibrium iteration, the local yield locus zone is known and one has to search its intersection with a stress direction *dir*, hopefully close to $\underline{s}^*$ (the stress direction corresponding to point 0). If no intersection is found, this means that the local yield locus zone is not correctly located and a new one has to be computed.

If the intersection is found, $\xi_1^*, \xi_2^*, \xi_3^*, \xi_4^*$ are its isoparametric coordinates. They identify the scaled yield stress in direction *dir*. The associated normal $\underline{u}^{interpolated}$ is computed by:

$$u_p^{nterpolated} = \sum_{k=1}^{5} \Phi_k(\xi_1^*, \xi_2^*, \xi_3^*, \xi_4^*)(u_p)_k \quad \text{with } p = 1,...5 \tag{6-85}$$

where $(u_p)_k$ is the p^{th} component of the strain rate direction associated with the five nodal points, k identifies the five points determining the hyperplane facet in which the intersection has been found. Four strain rate directions correspond to the $\underline{u}^{(i)}$, resulting of the perturbation process described above and one to the central strain rate direction $\underline{u}^*$. The corresponding unit vector $\underline{u}^{int\ erpolated}$ is then calculated since relation (6-85) does not produce a unit vector. Figure 6-37 shows, in a two-dimensional space, all the directions of "normals" to the stress yield locus. It is assumed that $\underline{u}^{int\ erpolated}$ is a better approximation of the true strain rate direction $\underline{u}^{true}$ than $\underline{u}^{hyperplane}$.

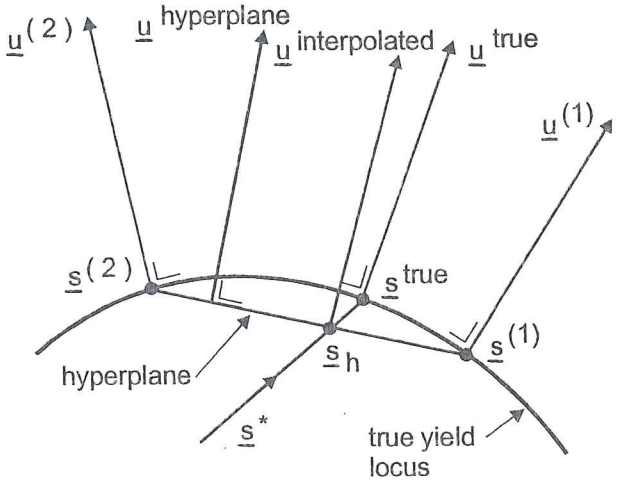

Figure 6-37 Normals to the stress yield locus, adapted from Habraken & Munhoven 1996.

The above description defines the hyperplane model except for the hardening evolution (factor τ) since only scaled values have so far been treated. The simple isotropic hardening approach proposed by Winters 1996 and already described in 6.3.4 is applied. Radu *et al.* 1997 and Habraken & Radu 1997 give all the details on the hyperplane approach.

The implementation in LAGAMINE of this constitutive law requires of course an integration scheme. Three different integration schemes were tested (Duchêne 1998a, Duchêne 1998c, Duchêne *et al.* 1999a). The first one is an application of the tangent cutting plane algorithm (Simo & Ortiz 1985). This procedure, already implemented by Li 1996 in LAGAMINE for the integration of Hill's constitutive law, can be visualized by Figure 6-38.

Its application to the hyperplane model introduces two iterative loops as summarized by the flowchart on Figure 6-39.

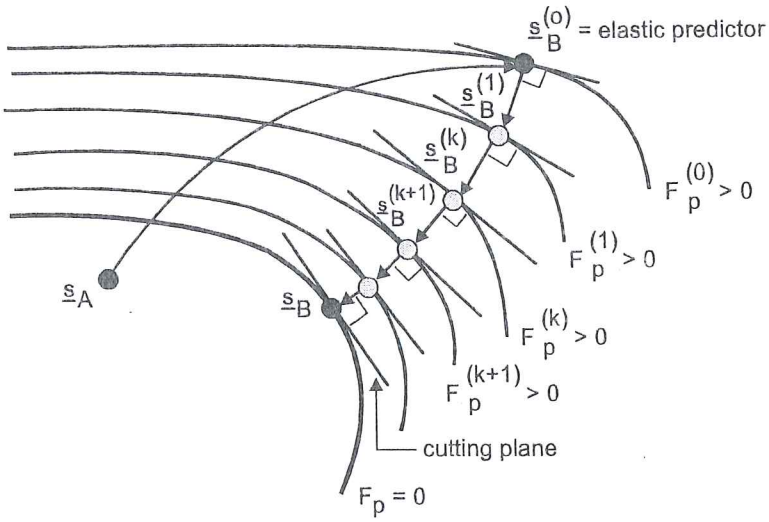

Figure 6-38 Tangent cutting plane algorithm, $\underline{s}_A$ stress at the step start, $\underline{s}_B$ stress at the step end (from Li 1996).

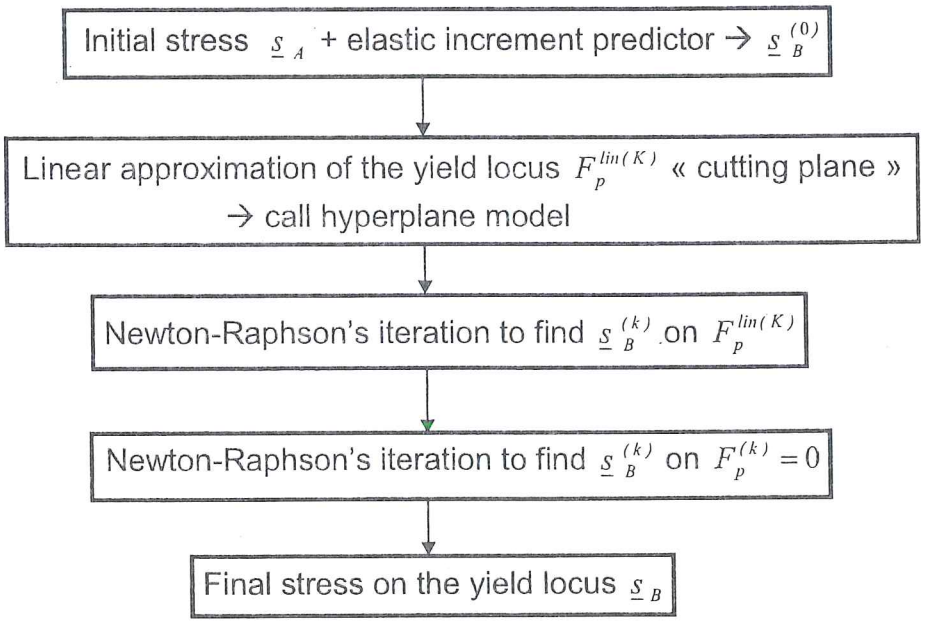

Figure 6-39 Flow chart of cutting plane algorithm (from slides used for Duchêne *et al.* 1999a's presentation).

The details can be found in Habraken & Munhoven 1996. This first scheme is quite expensive in CPU time. So, Duchêne 1998a has proposed a second integration scheme where only one iteration loop appears. Its principle is visualized in Figure 6-40, and Figure 6-41.

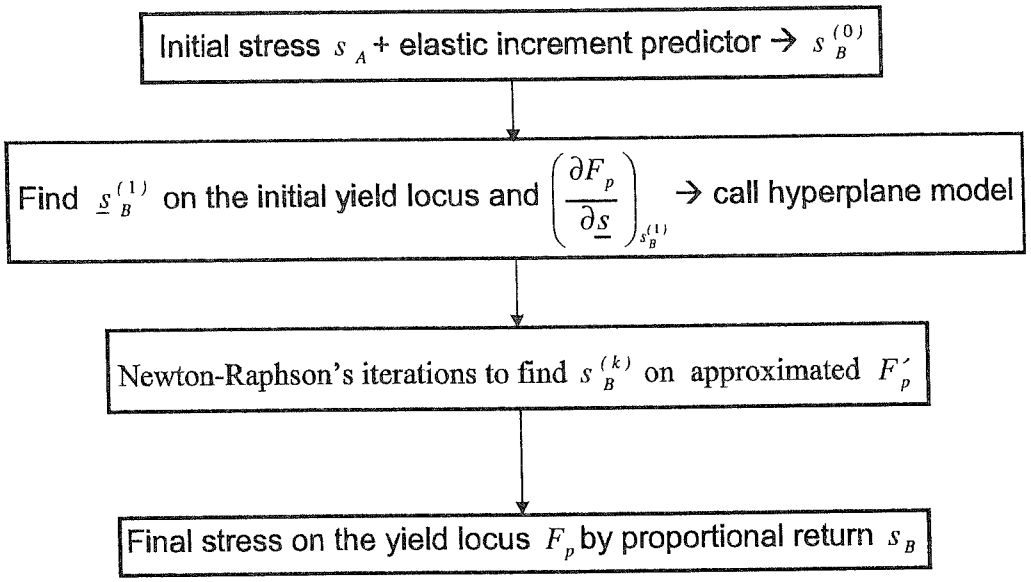

Figure 6-40 Flowchart of Duchêne's integration scheme (from slides used for Duchêne *et al.* 1999a's presentation).

The exact stress $\underline{s}_B^{true}$ is located on the real yield locus updated by hardening. It differs slightly from the final stress $\underline{s}_B$ provided by Duchêne's scheme. An improved solution could be reached by performing a radial return along the normal associated to $\underline{s}_B$. However, as this new iteration loop slows down the integration scheme, it has not been implemented.

Sometimes, the initial elastic trial can be very far from the initial yield stress at the step beginning and also very far from the final stress at the step end. In this case, the local yield locus zone must be updated a few times during the integration scheme to cover the interesting part of the yield locus. So, we decided to use an elasto- plastic predictor (Figure 6-41) to increase the life time of one set of hyperplanes.

The matrix used to compute the elasto-plastic predictor comes from the preceding converged step. This requires its storage or its computation. So, even if the scheme seems very simple, this method is not so direct.

These 3 integration schemes have been compared thanks to FEM simulations modeling a simple tensile test with one finite element. It appears (Duchêne *et al.* 1999a) that the elasto-plastic predictor scheme provides the best accuracy, convergence rate and lowest CPU time. It reduces the number of updates of the yield locus zones. Concerning CPU time, Duchêne's scheme comes in second position and provides the same accuracy as the other elastic predictor scheme (Li 1996). The size of hyperplane approximation has also been investigated. It is characterized by the scalar β (relation 6-81) or by the angle θ between the $\underline{u}^{(i)}$ directions, with

$cos\theta = \underline{u}^{*}.\underline{u}^{*(j)}$. This is a key parameter for both accuracy and CPU time. The smallest size gives the highest accuracy but also high CPU time. Table 6-2 shows the CPU time comparison with the time unit set to 1 for the fastest case.

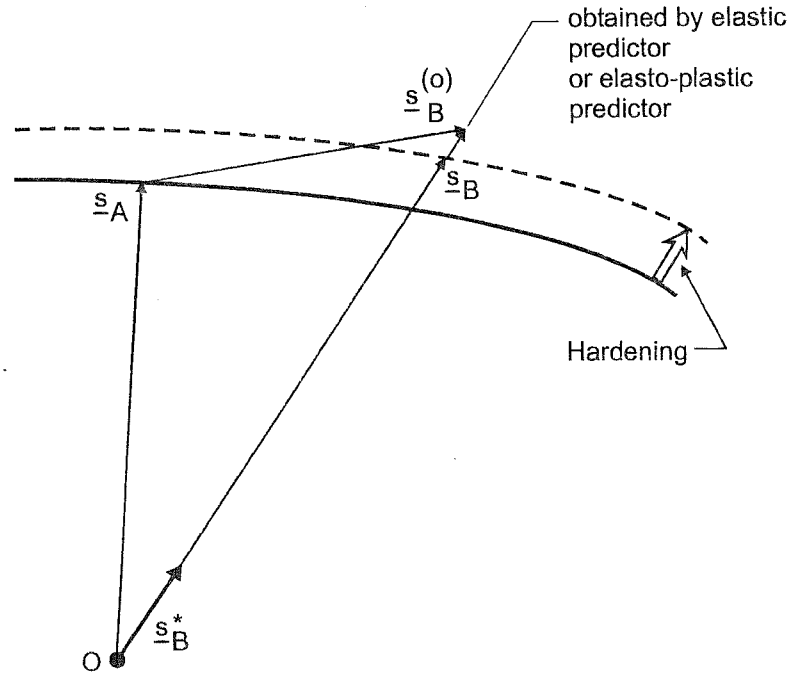

Figure 6-41 Schematic view of plastic predictor scheme (from slides used for Duchêne *et al.* 1999a's presentation).

Angle θ	1°	5°	10°	20°	30°
First method (elastic predictor 1)	-	98.9	1.40	1.27	1.15
Second method (elastic predictor 2)	-	89.8	1.34	1.22	1.05
Third method (plastic predictor)	1.92	1.15	1.14	1.01	1

Table 6-2 Comparison of the CPU time for tensile tests (from Duchêne *et al.* 1999a).

Eight different strain rate tensors, modeling situations more complex than uniaxial tension have been computed by "one finite element" simulations (Duchêne 1998c). It appears from these more complex strain states, that the elasto-plastic predictor scheme yields poor accuracy. It updates the local yield locus zone more often than the elastic predictor scheme proposed by Duchêne.

A tensile test of a plane sheet with a hole has also been simulated by 766 finite elements. The results confirm that elastic prediction of Duchêne's scheme is a better choice.

B. Stiffness matrix

The implicit finite element approach of the LAGAMINE code requires a global tangent stiffness matrix assembled from the local tangent stiffness matrices associated with each finite element. So, at each interpolation point, the $\underline{C}^{ep}$ matrix linking the stress increment to the strain increment is necessary. Different evaluations (Li 1996) are possible:

- classical tangent matrix, which is directly obtained from the continuum rate constitutive equation:

$$\overset{\nabla}{\sigma} = \underline{C}^{ep}\,\underline{\dot{\varepsilon}} \tag{6-86}$$

- consistent tangent matrix, which is computed by consistent linearization of the integration scheme;
- numerical tangent matrix, which is evaluated by numerical perturbations. The stress at the end of the time step is first computed for the actual strain increment ($\dot{\varepsilon}\,\Delta t$). Then, one at a time, each strain rate component is perturbed and the integration scheme provides a new perturbed stress. The difference between perturbed stress and actual stress, divided by the strain perturbation, yields one column of the tangent matrix.

These 3 approaches (Duchêne 1998a) have been implemented. The consistent tangent matrix is known to preserve the quadratic convergence of the global iteration scheme. However in the performed simulations, it does not clearly provide a better convergence than the classical tangent matrix. As the approximation of the tangent matrix by the numerical tangent matrix induces a higher convergence rate, it suggests that our linearization approach should be refined. The numerical tangent matrix suffers from two main drawbacks: the influence of the numerical perturbation amplitude and the CPU time required to compute it.

C. Yield locus section

The influence of the size of the local yield locus zone can be visualized as follows. The modules computing the stress are called for successive stress directions determining the π section of the yield locus.

Figure 6-42 results from different choices of hyperplane sizes, defined by angle θ. The parameter β, or its associated angle θ, strongly modifies the yield locus approximation and the number of necessary updates of the hyperplane approximation to cover a whole π section. One can verify on this figure that large hyperplane facets underestimate the yield stress and create very strong discontinuities when the local approximation of the yield locus is updated. From this figure and the convergence of different simulations, the size corresponding to 5° or 10° should be adopted.

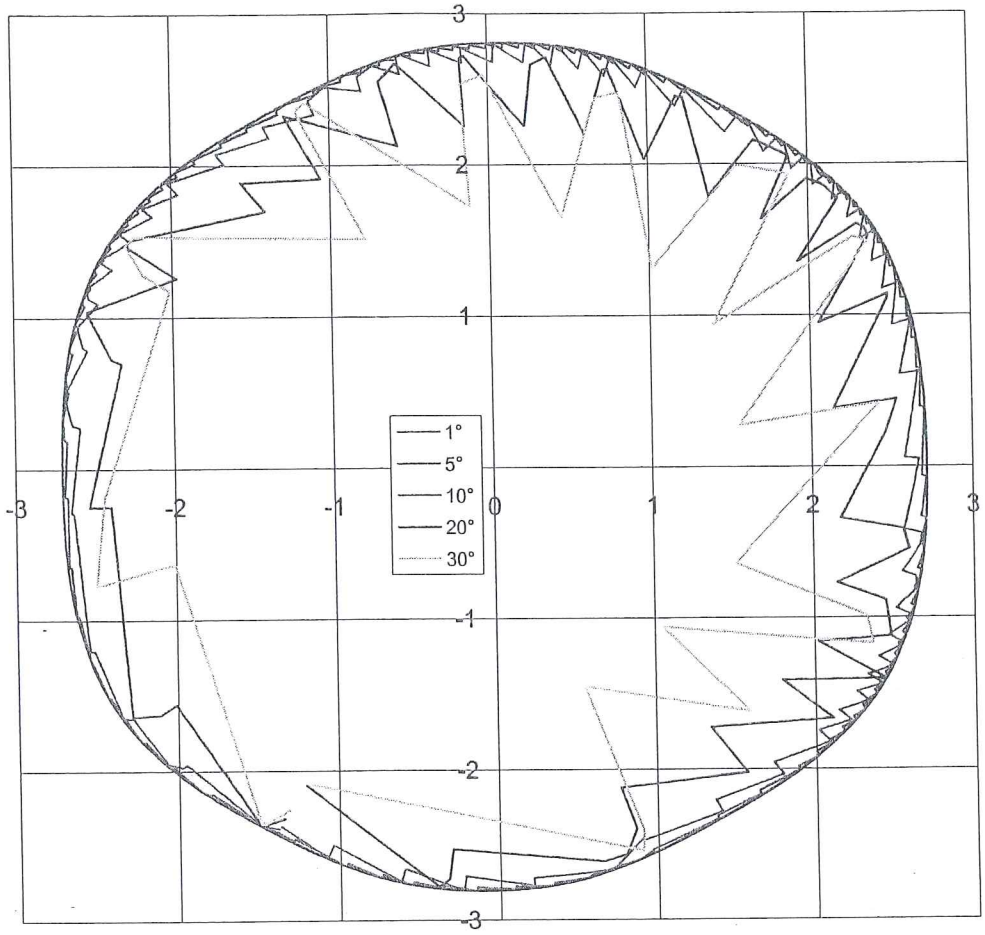

Figure 6-42 π section of the yield locus for different hyperplane sizes, SPXI steel sheet (from Duchêne *et al.* 1999c).

D. Conclusion

This local yield locus approach suffers from strong discontinuities that explain the convergence problems happening in finite element simulations with a large number of finite elements. It has been dropped in favor of a new method, more continuous, directly inspired from the investigations required to develop the hyperplane approach.

6.4.4. Interpolation approach

Developed thanks to a close cooperation of Godinas, Duchêne and Habraken, this method appears more stable and less expensive in CPU time than the hyperplane approach. Duchêne's Ph.D thesis, which should come to an end during 2001, will present numerous comparisons between deep drawing experiments, FEM simulations with and without texture updating and FLD predictions.

This method has already been described in Duchêne's master (Duchêne 2000). Its summary and some results have been published in ICOTOM, NUMISHEET, and ESAFORM proceedings (Duchêne *et al.* 1999b and c, 2000, 2001). Theory and applications are recalled here to give the reader a complete overview of the performed work. The text is adapted to the notations and principles introduced in previous chapters.

A. Local description of a scaled yield locus

The shape of the yield locus is our present goal. The size of the yield locus is defined by a simple hardening law, as already proposed by Winters 1996. The method proposed hereafter is more an interpolation approach than a local representation of a scaled yield locus. A "function" locally describing the plastic surface is not developed. Nevertheless, this interpolation method assumes the existence of a yield locus.

Keeping the notations of the previous sections, let $\underline{s}^{*\circ}$ be a unit stress vector, corresponding to the direction of the central point of the local yield locus zone. $\underline{s}^{*(i)}$ are $N(=5)$ unit stress vectors surrounding $\underline{s}^{*\circ}$ and determining the interpolation domain. They will be called the "domain limit vectors." In practice, the approach has been developed for a N dimensional space but it is directly applied to the five dimensional case as the goal is to define a local yield locus zone in deviatoric stress or strain rate space. Hereafter, the notation choice is adapted to stress space but the whole approach can be transposed to strain rate space. The six or $(N+1)$ vectors (five $\underline{S}^{*(i)}$ and one $\underline{s}^{*\circ}$) have the following properties:

-they are unit vectors:

$$\underline{s}^{*(i)}.\underline{s}^{*(i)} = 1 \quad \text{and} \quad \underline{s}^{*\circ}.\underline{s}^{*\circ} = 1 \tag{6-87}$$

-there is a common angle between all $\underline{s}^{*(i)}$:

$$\underline{s}^{*(i)}.\underline{s}^{*(j)} = 1 + \beta^2(\delta_{ij} - 1) \quad \text{with } i,j = 1,...N \tag{6-88}$$

-there is a common angle between each $\underline{s}^{*(i)}$ and $\underline{s}^{*\circ}$:

$$\underline{s}^{*0}.\underline{s}^{*(i)} = \cos\theta \quad \text{with } i = 1,...N \tag{6-89}$$

-they determine a regular domain.

These choices induce that $\underline{s}^{*0}$, the central direction, can be computed as a scaled average of the five (N) limit vectors $\underline{s}^{*(i)}$:

$$\underline{s}^{*0} = \frac{1}{\cos\theta} \sum_{i=1}^{N} \underline{s}^{*(i)} \tag{6-90}$$

Both the angle θ and the parameter β determine the size of the interpolation domain. They are linked by the relation:

$$\beta^2 = \frac{N}{N-1} \sin^2\theta \tag{6-91}$$

As the N $\underline{s}^{*(i)}$ vectors are linearly independent, they constitute a vector basis for the N-dimensional space. However, as they are not orthogonal, it is interesting to introduce N new vectors $\underline{ss}^{(i)}$ with the following orthogonal property:

$$\underline{ss}^{(i)} . \underline{s}^{*(j)} = \delta_{ij} \tag{6-92}$$

These vectors are called "contravariant vectors". Relation (6-87) implies that they are not unit vectors and one can verify that they depend linearly on vectors $\underline{s}^{*(i)}$ and $\underline{S}^{*}$:

$$\underline{ss}^{(i)} = \frac{1}{\beta^2} \left(\underline{s}^{*(i)} - \frac{1-\beta^2}{\cos\theta} \underline{s}^{*0} \right) \tag{6-93}$$

The N η coordinates representing any vector $\underline{v}$ in the $\underline{s}^{*(i)}$ vector basis:

$$\underline{v} = \sum_{i=1}^{N} \eta_i \underline{s}^{*(i)} \tag{6-94}$$

are determined thanks to the N $\underline{ss}^{(i)}$ vectors:

$$\underline{v} . \underline{ss}^{(j)} = \sum_{i=1}^{N} \eta_i \underline{s}^{*(i)} . \underline{ss}^{(j)} = \sum_{i=1}^{N} \eta_i \delta_{ij} = \eta_j \tag{6-95}$$

These N η coordinates are independent of each other. They determine both the length and the direction of vector $\underline{v}$. It is important to note that, for a unit vector $\underline{v}$ equal to a domain limit vector $\underline{s}^{*(i)}$, the $\eta_j^{(i)}$ coordinates are:

$$\eta_j^{(i)} = \delta_{ij} \quad \text{with } j = 1,...5 \tag{6-96}$$

These vectors represent the domain vertices. Each of the N limit boundaries (or edges) of the interpolation domain correspond to a function such that:

$$\eta_i = 0 \tag{6-97}$$

In fact, the properties associated with isoparametric interpolations already recalled on Figure 6-35 are retrieved but extrapolated to N-dimensions. The above choices imply that any point belonging to the interpolation domain is associated with positive η coordinates.

A practical way to determine the 5 domain limit vectors $\underline{s}^{*(i)}$ is identical to the procedure described by 6-80 to 6-84. A particular central direction $\underline{s}'^{*0}$ is chosen in such a way that its N components are identical. To obtain associated domain limit vectors $\underline{s}'^{*(i)}$, one successively computes a linear relation between the central direction and each vector of the Cartesian basis $\underline{e}^{(i)}$:

$$\underline{s}'^{*(i)} = \alpha' \underline{s}'^{*0} + \beta \underline{e}^{(i)} = \underbrace{\alpha' \frac{1}{\sqrt{N}}}_{=\alpha} \begin{pmatrix} 1 \\ 1 \\ 1 \\ 1 \\ 1 \end{pmatrix} + \beta \begin{pmatrix} 0 \\ \vdots \\ 1 \\ \vdots \\ 0 \end{pmatrix} \tag{6-98}$$

Using the conditions that $\underline{s}'^{*(i)}$ and $\underline{s}'^{*0}$ must be unit vectors and relation (6-89), one obtains:

$$\alpha = \frac{\cos\theta}{\sqrt{N}} - \frac{\sin\theta}{\sqrt{N \cdot (N-1)}} \text{ and } \beta^2 = \frac{N}{N-1} \sin^2\theta \tag{6-99}$$

Then the rotation linking the actual required central point $\underline{s}^{*0}$ and the particular one $\underline{s}'^{*0}$ is computed by:

$$\underline{R} = \underline{I} + 2\,\underline{s}^{*0} \otimes \underline{s}'^{*0} - \frac{\left(\underline{s}^{*0} + \underline{s}'^{*0}\right) \otimes \left(\underline{s}^{*0} + \underline{s}'^{*0}\right)}{1 + \underline{s}^{*0} \cdot \underline{s}'^{*0}} \tag{6-100}$$

where $\underline{I}$ is the second order unit tensor. This rotation applies $\underline{s}'^{*0}$ onto the real central vector $\underline{s}^{*0}$:

$$\underline{R} \cdot \underline{s}'^{*0} = \underline{s}^{*0} \tag{6-101}$$

It also provides the domain limit vectors:

$$\underline{R} \cdot \underline{s}'^{*(i)} = \underline{s}^{*(i)} \tag{6-102}$$

If $\underline{s}^{*0}$ and $\underline{s}'^{*0}$ are opposite vectors, equation (6-100) is not valid; the domain limit vectors $\underline{s}^{*(i)}$ can be computed as the opposite of the $\underline{s}'^{*(i)}$.

This interpolation domain is called a regular one because the angles between the domain limit vectors are identical (6-89) and the domain limit vectors are unit vectors. However, it is possible to define interpolation domains based on limit vectors that are non-uniformly located and are non unit vectors provided they are

linearly independent. With such non-regular domains, the η coordinates are still available and require the definition of $\underline{ss}^i$ vectors (see relations 6-90, 6-92, 6-95).

The above considerations are sufficient to understand the interpolation approach finally implemented in the LAGAMINE code. However, it is interesting to note that further details and properties of such parameterization of a N dimensional space were investigated by Godinas 1998 and Duchêne 2000. They study different interpolation methods: linear interpolation in Cartesian coordinates or hyperplane model, linear interpolation in spherical coordinates, approach enriched by bubble mode...

Now, consider both five dimensional stress and strain rate spaces. A regular domain is built in strain rate space. It is defined by its five vertices $\underline{u}^{*(i)}$ (unit vectors). Thanks to five calls to Taylor's module (Figure 6-38), the associated stress vectors $\underline{s}^{(i)}$ can be defined. At this level, no hardening is assumed, so only a scaled yield locus is determined. These five stress vectors define a non-regular domain in stress space. In each space, the concept of contravariant vectors, from relation (6-92), is applied:

$$\underline{uu}^{(i)} . \underline{u}^{*(j)} = \delta_{ij} \tag{6-103}$$

$$\underline{ss}'^{(i)} . \underline{s}^{(j)} = \delta_{ij} \tag{6-104}$$

The contravariant vectors $\underline{ss}'^{(i)}$ and $\underline{ss}^{(i)}$, respectively computed by (6-104) and (6-92), differ only because in (6-92) unit stress directions $\underline{s}^{*(i)}$ are used. Here the length of the stress vectors $\underline{s}^{(j)}$ is an important characteristic as it defines the yield locus anisotropy. These contravariant vectors $\underline{ss}'^{(i)}$ and $\underline{uu}^{(i)}$ give in each space, the η coordinates associated with any stress $\underline{s}$ or unit strain rate $\underline{u}^*$:

$$\eta_i = \underline{uu}^{(i)} . \underline{u}^* \tag{6-105}$$

$$\eta_i = \underline{ss}'^{(i)} . \underline{s} \tag{6-106}$$

So any stress vector $\underline{s}$ or strain rate direction $\underline{u}^*$ can be represented according to the vector basis of their space and the η coordinates:

$$\underline{u}^* = \sum_{i=1}^{5} \eta_i \, \underline{u}^{*(i)} \tag{6-107}$$

$$\underline{s} = \sum_{i=1}^{5} \eta_i \, \underline{s}^{(i)} \tag{6-108}$$

Physically, a material state corresponds to a stress point and a strain rate direction. In a yield locus formulation, a point on the locus and its normal define both stress and

associated strain rate. Here, two interpolation domains are defined; they are physically linked because Taylor's model computes their domain limit vectors. Due to this close link between the two spaces, it is assumed that the η coordinates computed by (6-105) and (6-106) are equal when the stress $\underline{s}$ and the strain rate direction $\underline{u}^*$ are physically associated. This property is exactly fulfilled for the domain limit vectors. The stress $\underline{s}^{(i)}$ corresponds to the strain rate direction $\underline{u}^{*(i)}$ and their η coordinates are $\eta_i = 1$ and $\eta_j = 0 (i \neq j)$ in both spaces. Inside the domain, this property is extended by convenience. It is an assumption. The so-called interpolation approach directly derives from this hypothesis of equality and from relations (6-108) and (6-105). They provide the interpolation relation:

$$\underline{s} = \sum_{i=1}^{5} (\underline{\underline{uu}}^{(i)} . \underline{u}^*) \underline{s}^{(i)} = \underline{\underline{uu}}^{(i)} \otimes \underline{s}^{(i)} . \underline{u}^* = \underline{\underline{C}} . \underline{u}^* \qquad (6\text{-}109)$$

For each domain, the $\underline{\underline{C}}$ matrix is computed only once from the stress domain limit vectors $\underline{s}^{(i)}$ and the contravariant vectors $\underline{\underline{uu}}^{(i)}$ associated with the 5 strain rate vertices $\underline{u}^{*(i)}$. Inside a domain, relation (6-109) provides the stress state if the strain rate direction is given. The η coordinates computed by relation (6-105) control the domain validity. If their values do not belong to the interval $[0,1]$, then a new local yield locus zone is required.

B. Updating of the scaled yield locus description

When the available local description of the scaled yield locus does not cover the interesting zone anymore, one has to find another local description enclosing the interesting part of the yield locus. Of course, the procedure described in previous section could be repeated using a new strain rate direction $\underline{u}^*$ as central point. However, this would provide a new local description forgetting the previous information and the discontinuities observed with the hyperplane approach would appear again. Looking at the η coordinate that does not belong to $[0,1]$ anymore, one can identify the boundary that is not respected by the new explored direction. This boundary is identified by $N-1$ (4) domain limit vectors and can belong to two regular domains. A 3 dimensional analogy represented on Figure 6-43 helps to understand.

The two neighboring domains defined by their common boundary require only one additional domain limit vector to be completely defined. So, only one new vertex must be computed by Taylor's model to identify the neighboring domain that probably contains the new explored strain rate direction. This is the option adopted in the LAGAMINE code.

associated strain rate. Here, two interpolation domains are defined; they are physically linked because Taylor's model computes their domain limit vectors. Due to this close link between the two spaces, it is assumed that the η coordinates computed by (6-105) and (6-106) are equal when the stress $\underline{s}$ and the strain rate direction $\underline{u}^*$ are physically associated. This property is exactly fulfilled for the domain limit vectors. The stress $\underline{s}^{(i)}$ corresponds to the strain rate direction $\underline{u}^{*(i)}$ and their η coordinates are $\eta_i = 1$ and $\eta_j = 0 (i \neq j)$ in both spaces. Inside the domain, this property is extended by convenience. It is an assumption. The so-called interpolation approach directly derives from this hypothesis of equality and from relations (6-108) and (6-105). They provide the interpolation relation:

$$\underline{s} = \sum_{i=1}^{5} (\underline{uu}^{(i)} . \underline{u}^*) \underline{s}^{(i)} = \underline{uu}^{(i)} \otimes \underline{s}^{(i)} . \underline{u}^* = \underline{C} . \underline{u}^* \qquad (6\text{-}109)$$

For each domain, the $\underline{C}$ matrix is computed only once from the stress domain limit vectors $\underline{s}^{(i)}$ and the contravariant vectors $\underline{uu}^{(i)}$ associated with the 5 strain rate vertices $\underline{u}^{*(i)}$. Inside a domain, relation (6-109) provides the stress state if the strain rate direction is given. The η coordinates computed by relation (6-105) control the domain validity. If their values do not belong to the interval $[0,1]$, then a new local yield locus zone is required.

B. Updating of the scaled yield locus description

When the available local description of the scaled yield locus does not cover the interesting zone anymore, one has to find another local description enclosing the interesting part of the yield locus. Of course, the procedure described in previous section could be repeated using a new strain rate direction $\underline{u}^*$ as central point. However, this would provide a new local description forgetting the previous information and the discontinuities observed with the hyperplane approach would appear again. Looking at the η coordinate that does not belong to $[0,1]$ anymore, one can identify the boundary that is not respected by the new explored direction. This boundary is identified by $N-1$ (4) domain limit vectors and can belong to two regular domains. A 3 dimensional analogy represented on Figure 6-43 helps to understand.

The two neighboring domains defined by their common boundary require only one additional domain limit vector to be completely defined. So, only one new vertex must be computed by Taylor's model to identify the neighboring domain that probably contains the new explored strain rate direction. This is the option adopted in the LAGAMINE code.

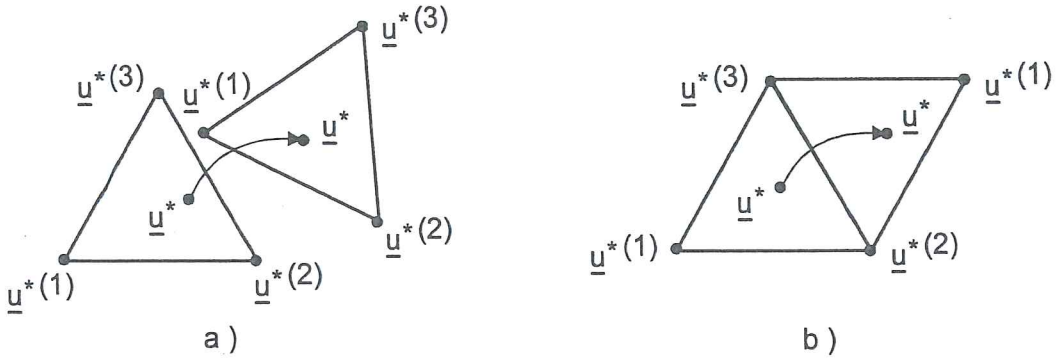

Figure 6-43 Updating of the local description
a) Completely new local description b) Neighborhood domain,
(from Duchêne 2000).

C. Integration scheme

The stress-strain interpolation relation (6-109) does not use the concept of yield locus in a classical way. So, a specific integration scheme has been developed. At this level, the actual stress and not the scaled one is aimed at, so the size and the shape of the yield locus cannot be dissociated anymore. As relation (6-109) expresses the shape and is assumed to model a reference level of hardening, an additional factor τ is introduced to represent hardening:

$$\boxed{\underline{s} = \tau \, \underline{C} . \underline{u}^*} \tag{6-110}$$

It plays the same role as the hardening factor $\bar{\tau}_c$ in (6-57b) and is simply linked to the total polycrystal slip Γ by a Swift's law:

$$\tau = K(\Gamma_0 + \Gamma)^n \tag{6-111}$$

As in Winters 1996, this micro-macro hardening law is identified by a tensile uniaxial macroscopic test and the first term of relation (4-40) (see the summary of this approach in section 6.3.4.).

Relation (6-110) assumes plastic loading. Writing this equation at the step beginning, identified by subscript A, and at the step end, identified by subscript B, subtracting these two relations and neglecting higher order terms yields the incremental form:

$$d\,\underline{s} = \underline{C} . \left(d\tau \, \underline{u}^*_A + \tau_A \, d\underline{u}^* \right) \tag{6-112}$$

with $d\,\underline{s} = \underline{s}_B - \underline{s}_A$; $d\tau = \tau_B - \tau_A$ and $d\,\underline{u}^* = \underline{u}^*_B - \underline{u}^*_A$.

During such a time step, Hooke's law links the stress and the elastic strain increments:

$$d\,\underline{s} = \underline{C}^e . \left(d\underline{\varepsilon}^{tot} - d\underline{\varepsilon}^p \right) = \underline{C}^e . \left(d\underline{\varepsilon}^{tot} - \dot{\varepsilon}^p_{eq} \, dt \, \underline{u}^*_A \right) \tag{6-113}$$

where it has been assumed that, during this time step, the direction of the strain rate $\underline{u}_A^*$ tensor is not modified. This assumption induces an approximation on the final tangent stiffness matrix provided by following considerations.
Because $\underline{u}_A^*$ and $\underline{u}_B^*$ are unit vectors, one can find that:

$$d\underline{u}^* . \underline{u}_A^* = 0 \tag{6-114}$$

Using (6-112) to (6-114), one can obtain :

$$d\tau = \underline{u}_A^* . \underline{C}^{-1} . \underline{C}^e . d\underline{\varepsilon}^{tot} - \underline{u}_A^* . \underline{C}^{-1} . \underline{C}^e . \underline{u}_A^* \dot{\varepsilon}_{eq}^p dt \tag{6-115}$$

The time derivative of relation (6-111) and the micro-macro relation established between the total polycrystal slip and the plastic strain (4-39) give:

$$d\tau = \frac{n\tau_A}{(\Gamma_0 + \Gamma_A)} \overline{M}\, \dot{\varepsilon}_{eq}^p dt \tag{6-116}$$

Both relations (6-115) and (6-116) allow to find an expression for $\dot{\varepsilon}_{eq}^p dt$:

$$\dot{\varepsilon}_{eq}^p\, dt = \frac{\underline{b} . \underline{C}^e . d\underline{\varepsilon}^{tot}}{\underline{a} . \underline{b} + \dfrac{n\tau_A}{\Gamma_0 + \Gamma_A} \overline{M}} \tag{6-117}$$

with $\underline{a} = \underline{C}^e . \underline{u}_A^*$ and $\underline{b} = \underline{u}_A^* . \underline{C}^{-1}$.

Relation (6-117), introduced in equation (6-113), provides an estimation of $\underline{C}^{tan}$, the tangent operator:

$$d\underline{s} = \left(\underline{C}^e - \frac{\underline{a} . \underline{b}\ \underline{C}^e}{\underline{a} . \underline{b} + \dfrac{n\tau_A}{\Gamma_0 + \Gamma_A} \overline{M}} \right) . d\underline{\varepsilon}^{tot} = \underline{C}^{tan} . d\underline{\varepsilon}^{tot} \tag{6-118}$$

If an explicit integration scheme is chosen, $\underline{s}_B$, the deviatoric stress at the step end, is directly computed by (6-118) and a Jaumann correction because of large deformation context:

$$\underline{s}_B = (\underline{I} + \underline{\Omega}) . \underline{s}_A + \underline{C}^{tan} . \Delta\underline{\varepsilon}^{tot} \tag{6-119}$$

The hardening is also computed by an explicit formulation:

$$\tau_B = \tau_A + \frac{n\tau_A}{(\Gamma_0 + \Gamma_A)} \overline{M}\, \Delta\varepsilon_{eq}^p \tag{6-120}$$

This rather simple formulation yields poor accuracy unless very small time steps or large number of subintervals are used. Adding a radial return slightly improves this

simple scheme. In this case, relation (6-119) computes $\underline{s}_{B\,trial}$, a trial stress. Then, it is corrected in order to return on the yield locus approximation:

$$\underline{s}_B = k\,\underline{s}_{B\,trial} \tag{6-121}$$

The strain rate direction $\underline{u}_B^*$ associated by (6-110) to this trial stress direction is assumed to be correct:

$$\underline{u}_B^* = \underline{\underline{C}}^{-1}.\underline{s}_{B\,trial}\,\frac{k}{\tau_B} \tag{6-122}$$

To respect the interpolation method, $\underline{u}_B^*$ must be a unit vector. One can compute k in order to respect this condition:

$$\underline{u}_B^*.\underline{u}_B^* = 1 \quad \Rightarrow \quad k = \frac{\tau_B}{\sqrt{\underline{b}_{trial}.\underline{b}_{trial}}} \tag{6-123}$$

with $\underline{b}_{trial} = C^{-1}.\underline{s}_{B\,trial}$.

Finally, in order to allow large time steps while retaining accuracy, an implicit scheme has been implemented in the LAGAMINE code. The stress at the step end is computed by:

$$\underline{s}_B = (\underline{\underline{I}} + \underline{\underline{\Omega}}).\underline{s}_A + \underline{\underline{C}}^e.(\Delta\underline{\varepsilon}^{tot} - \Delta\underline{\varepsilon}^p) \tag{6-124}$$

The plastic strain increment during the step is decomposed into its length $\Delta\varepsilon_{eq}^p$ and its direction, which is classically computed by a linear interpolation between the initial direction $\underline{u}_A^*$ and the final direction $\underline{u}_B^*$:

$$\Delta\underline{\varepsilon}^p = \Delta\varepsilon_{eq}^p\,k\left((1-\theta)\underline{u}_A^* + \theta\,\underline{u}_B^*\right) \tag{6-125}$$

with $0 \le \theta \le 1$. Again, the fact that the direction of the plastic strain increment $\underline{u}_B^*$ is a unit vector defines the value of k:

$$k = \frac{1}{\sqrt{1 + 2\theta(1-\theta)(\underline{u}_A^*.\underline{u}_B^* - 1)}} \tag{6-126}$$

If one replaces relations (6-126) and (6-125) into (6-124), this yields an equation with 2 unknown variables on the right side : $\underline{u}_B^*$ and $\Delta\varepsilon_{eq}^p$. It will be solved thanks to the interpolation relation (6-110) and the fact that $\underline{u}_B^*$ is a unit vector.

The following flowchart summarizes the implementation of the interpolation method as a constitutive law without sub-interval. More details can be found in Duchêne 2000, which proposes a description that conforms to the LAGAMINE routines. A sub-interval approach and the possibility to use an analytical tangent operator or a numerical one computed by a perturbation method are also described.

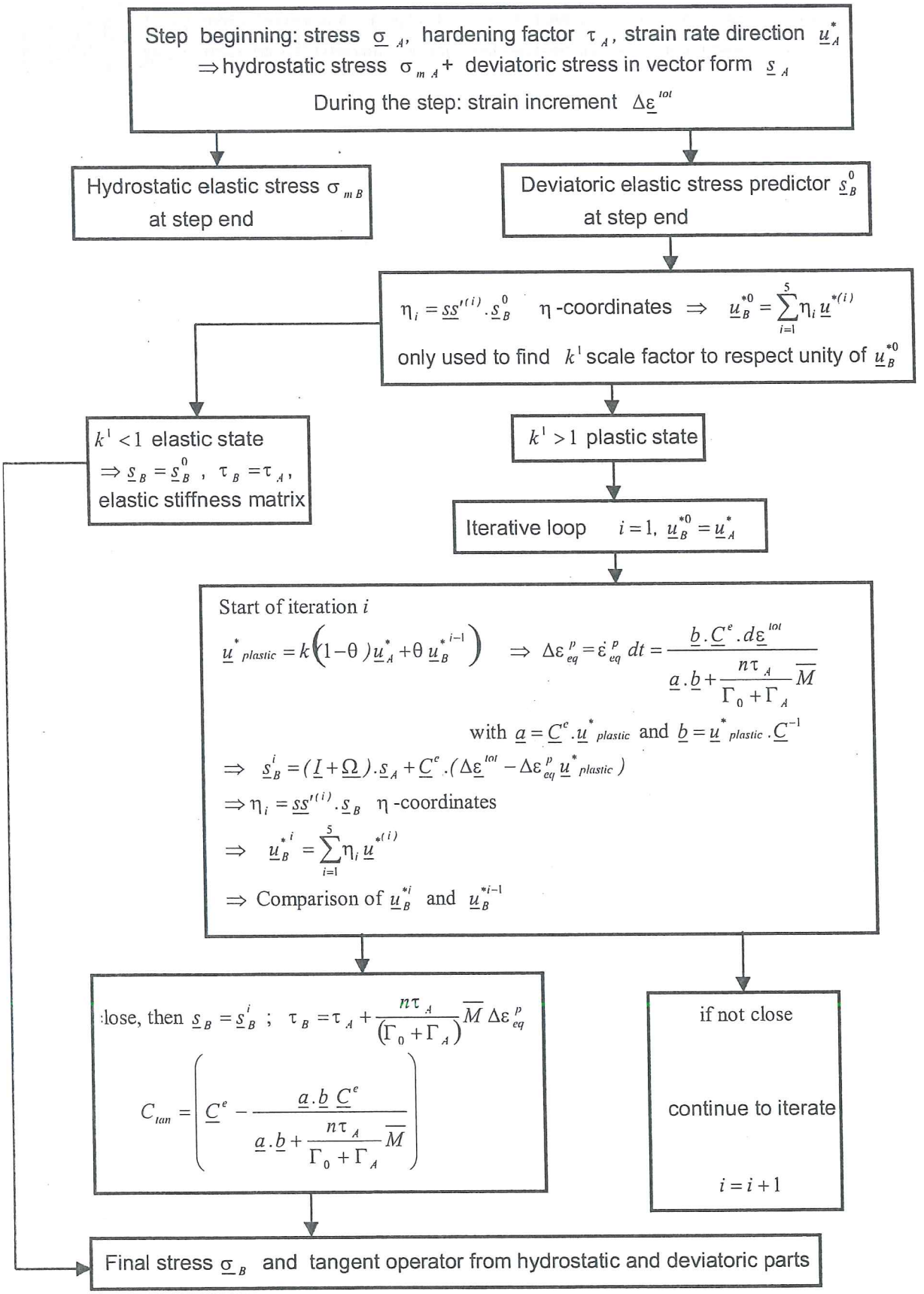

Figure 6-44 Flowchart of the interpolation method as constitutive law.

6.4.5. Conclusion

The hyperplane has been dropped to concentrate our research on the interpolation method. Key factors for its application are the number of crystal orientations, the size of the domain and the criterion to decide when texture updating is necessary. These questions are still under investigation and should be solved in Duchêne's Ph. D. thesis.

6.5. Validations of our models

6.5.1. Discrete sets of crystallographic orientations

In the developed constitutive laws, Taylor's model (see Figure 6-44) computes the domain limit stress vectors from the domain limit strain rate directions. So the number of discrete crystallographic orientations used to represent the texture is an important factor. It defines the accuracy of the domain limit stress vectors but also the CPU time. An estimation of the accuracy can be based either on ODF description or on stress computation.

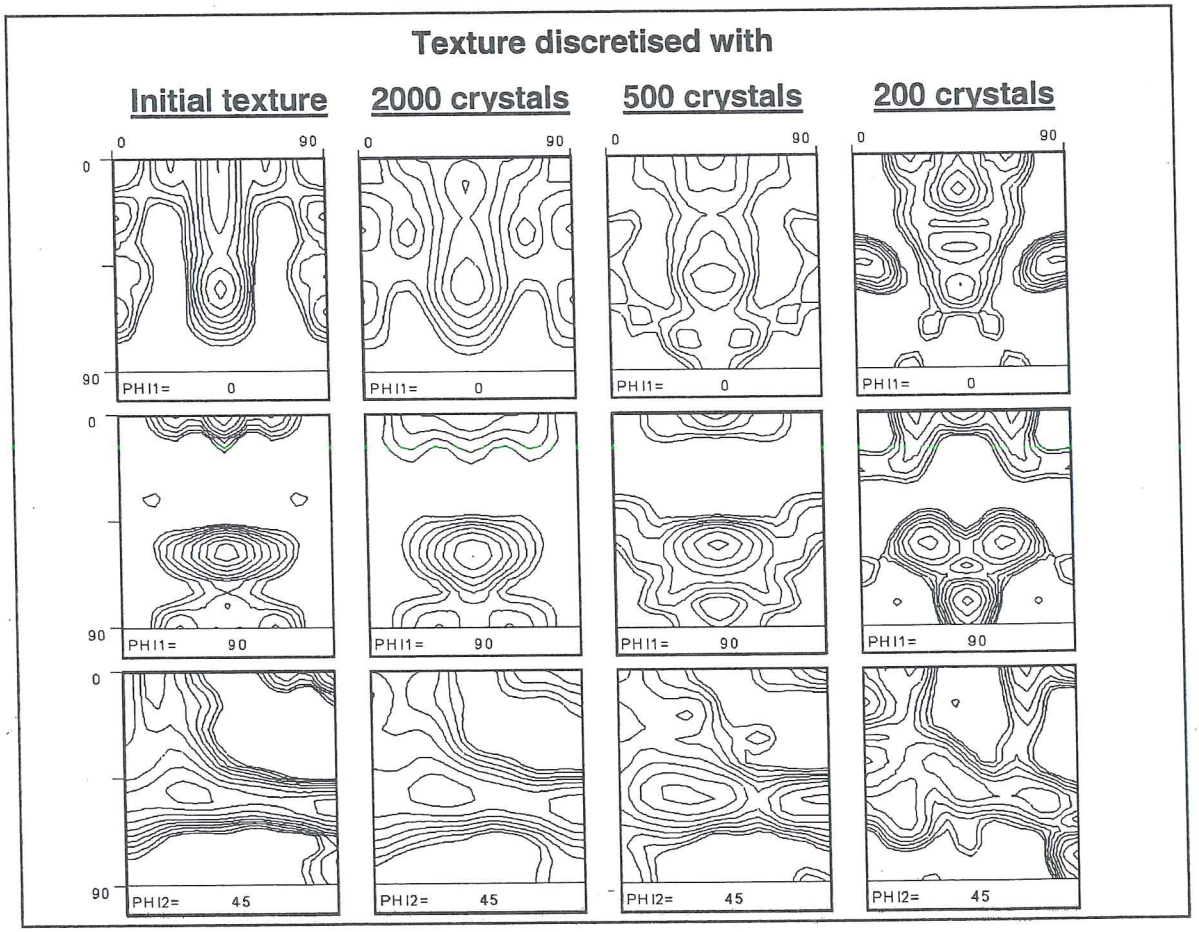

Figure 6-45 ODF sections before and after the use of discrete sets of orientations (from Duchêne *et al.* 2000).

For a SPXI steel sheet, Figure 6-45 shows sections of an ODF known by its coefficients after X-ray measurements. The method described in section 6.4.1 is applied to define 2000, 500 or 200 crystals that are representative of this texture. Then $C_l^{\mu\nu}$ coefficients are deduced from these 2000, 500 or 200 crystals respectively and sections of the ODF are drawn again on Figure 6-45. One can see that for 2000 crystals, the location of maxima is preserved as well as the section shape. However, with 200 crystals, there are still similitudes between ODF sections but a lot of features are lost.

Another way to compare the accuracy of discrete sets of orientations is to use them in Taylor's model to compute a stress tensor from different velocity gradients. Figure 6-46 computes the "error" due to a discrete representation of the texture for 2 different steel sheets (IF ULC Ti and SPXI) and 3 different velocity gradients. The reference response is provided by a Taylor's call using 40000 crystals. Here again one can check the important effect of the number of orientations on the result accuracy.

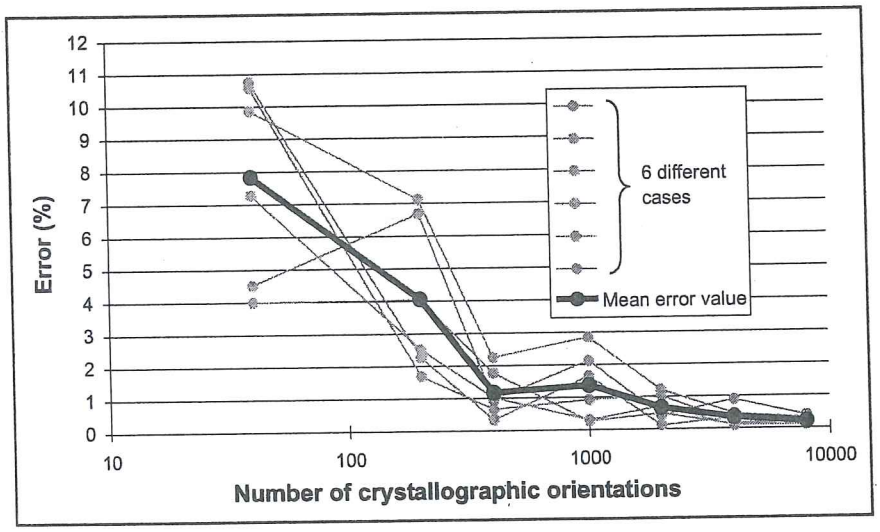

Figure 6-46 Error on stress computed by Taylor's model with different numbers of crystal orientations (from Duchêne *et al.* 2000).

A final means to estimate the effect of the number of crystal orientations is to use Taylor's model to compute π-sections of the yield locus. For the SPXI steel already described by its ODF on Figure 6-45, Figure 6-47 shows the effect of different ways to represent the texture.

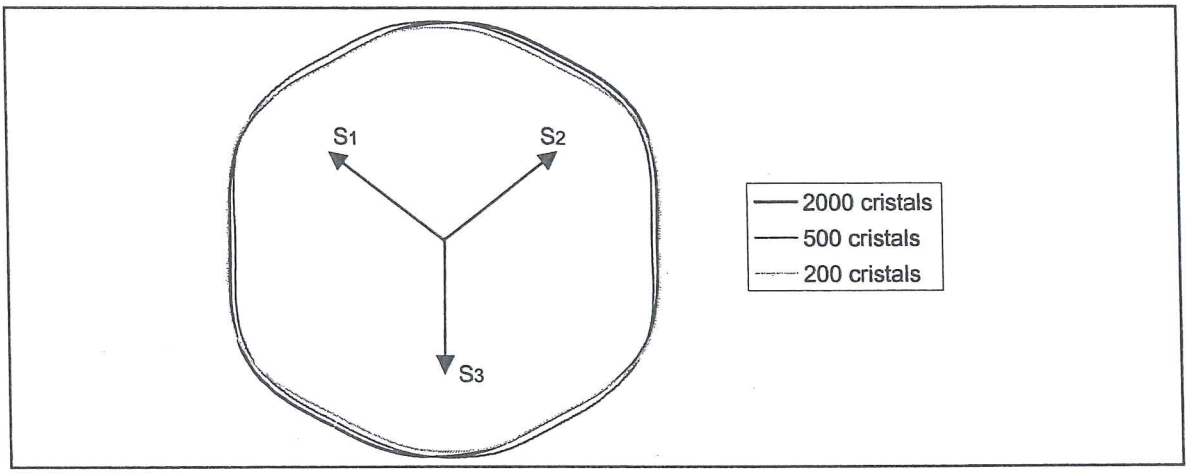

Figure 6-47 π-sections computed by Taylor's model for different representations of the texture, SPXI steel (from Duchêne *et al.* 2000).

In practice, a lot of our computations rely on 2000 crystals but further validations are necessary to know if this number can be decreased or not.

6.5.2. π-sections of the yield locus computed by local and non-local methods

For the SPXI steel sheet the texture of which is shown on Figure 6-45, the π-section has been computed by 5 different approaches:

- 6^{th} order = global yield locus in stress space described by a 6^{th} order series from van Houtte (see section 6.3.4).
- Hyp. 1°or 20° = Hyperplane approach with an angle of 1° or 20° between the strain rate directions used as domain limit vectors $\underline{u}^{*(i)}$ (see section 6.4.3).
- S-s I 1° or 20° = Stress-strain rate Interpolation approach with an angle of 1° or 20° between the strain rate directions used as domain limit vectors $\underline{u}^{*(i)}$ (see section 6.4.4)

The computational method to obtain π-sections has been described at the end of section 6.4.3. Figure 6-48 compares the π-sections obtained with the 5 investigated procedures. For the local approaches with large domains (Hyp. 20° and S-s I 20°), the associated yield locus normals, which represent the deviatoric plastic strain rates, are also plotted. Normals from the hyperplane approach are clearly discontinuous.

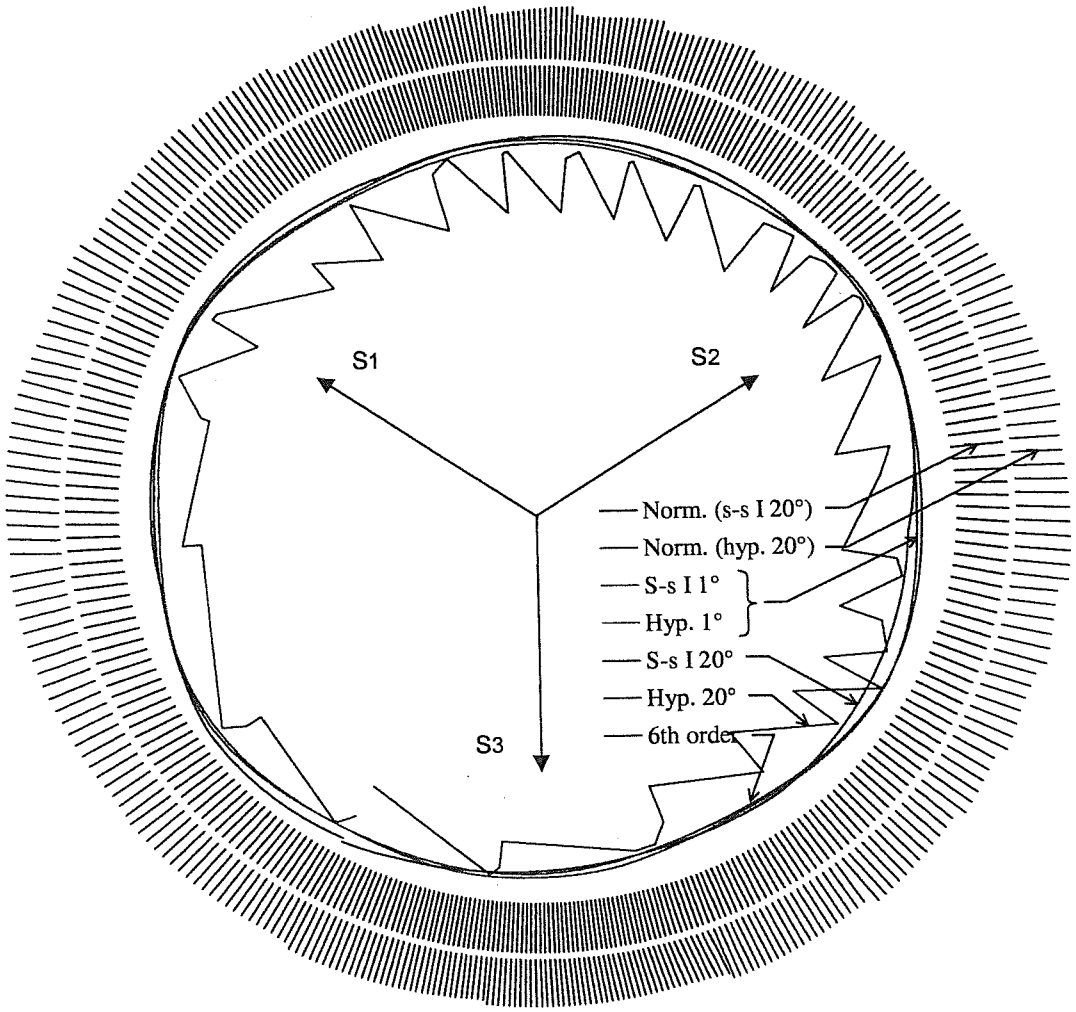

Figure 6-48 π-sections of the yield locus computed by 5 models, and normals to the yield loci computed by stress-strain rate interpolation and hyperplane method with a size of 20° (from Duchêne *et al.*1999c).

When small local domains are used (1°), their associated yield loci are superposed and very close to the yield locus computed by the 6th order series. For larger domain size (20°), the results of the hyperplane and interpolation methods strongly differ: while the interpolation approach is continuous and close to the yield loci computed by more accurate methods, the hyperplane result is discontinuous and diverges from other results.

Figure 6-47 and Figure 6-48 show that both the number of crystal orientations used to describe the texture and the size of the local description adopted in the interpolation method are key factors for the accuracy.

6.5.3. Lankford's coefficient prediction

For the SPXI steel sheet and the deep drawing IF ULC Ti steel sheet already treated in previous sections, Lankford's coefficients have been investigated.

Two sets of experimental results are available, the ones performed by MSM laboratory (Exp. MSM) and the others from the Research and Development Cockerill Sambre center (Exp. RDCS). These results take into account the hardening and the evolution of the yield locus as they are computed by the average of instantaneous Lankford's coefficient measured at strains of 10, 12, 14, 16, 18 %. The MSM measurements are described in Wauters 2000. Tests are systematically repeated 3 or 5 times. Their agreement with a previous set of measures, limited to strains 0 and 10% and performed by Charles (Charles & Habraken 1996) is not perfect. So, even with the same equipment a different set of sheets present variation. So, different equipment and different sets of sheets can explain the differences in the measurements from RDCS and MSM.

All the predictions of Lankford's coefficient are based on the initial texture. The results identified by "Texture" are computed directly from the texture information and Taylor's model as explained in van Houtte 1995. The points characterized by "6th order" rely on a global yield locus in stress space described by a 6th order series. The curves identified by S-s I 1°, 5°, or 10° are computed thanks to the interpolation method with different domain sizes.

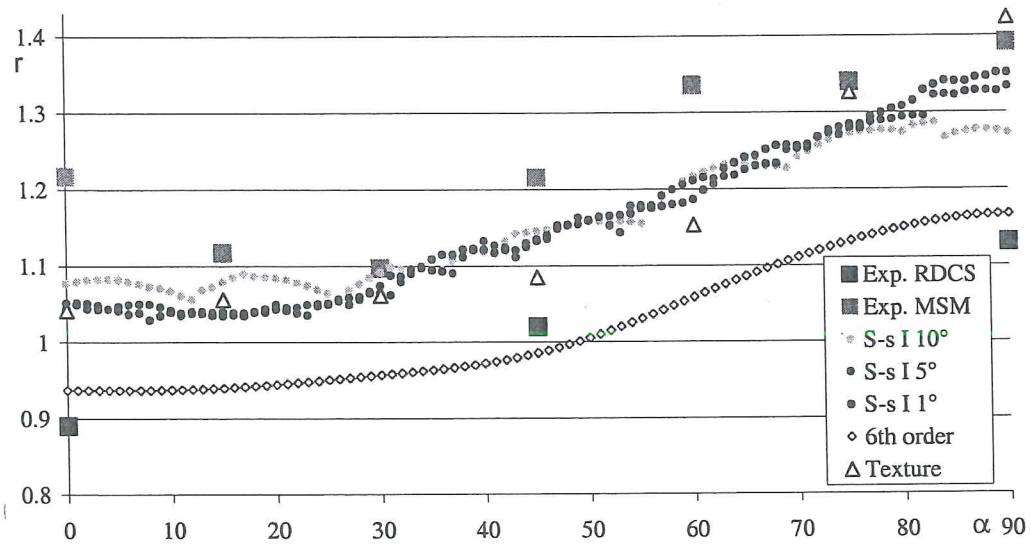

Figure 6-49 Measured and predicted Lankford's as a coefficient function of the angle with the Rolling Direction for SPXI steel (from Duchêne *et al.*1999c).

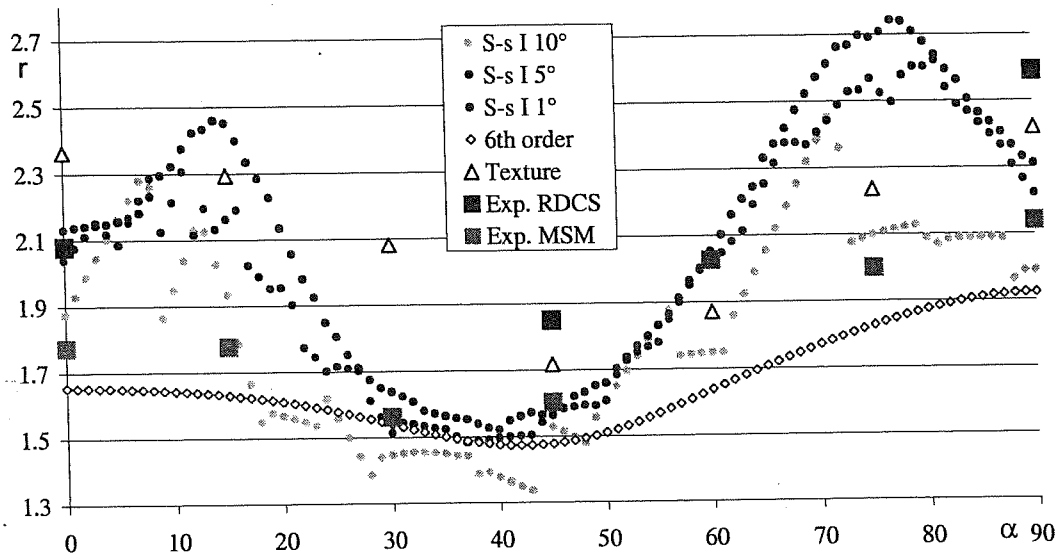

Figure 6-50 Measured and predicted Lankford's coefficient as a function of the angle with the Rolling Direction for IF ULC Ti steel (from Duchêne *et al.*1999c).

The general shapes of the experimental and computed curves are rather similar; however, the levels differ.

The SPXI sheet is characterized by a relatively weak texture with a maximum ODF-value of 5.9 (van Houtte & van Bael 1997). This leads to a quite smooth yield locus. This fact is confirmed by continuous and close curves predicted by the S-s approach with different domain sizes (1°, 5°, 10°). The agreement between Texture and S-s method is good, recovering that both methods finally rely on identical Taylor's model. The results computed by the 6^{th} order series yield locus are clearly underestimated by comparison to other predictions relying on crystal plasticity. This means that even a 6^{th} order series is too poor to represent the actual anisotropic yield locus and that this analytical function smoothes the reality.

The IF ULC Ti sheet consists in a strong γ-fiber (maximum ODF-value of 11.4), which broadens towards α-fiber. The associated yield locus presents a high anisotropy and one can verify that the S-s results clearly show jumps corresponding to the updating of the local yield locus zone. These jumps are of course higher for domain size of 10°. The S-s results do not coincide with texture results, this could perhaps be explained by the fact that working in the stress space introduces some inaccuracy compared on direct use of Taylor's model. The global 6^{th} order yield function is still not rich enough to catch the variation in Lankford's coefficient: the predicted curve seems too smooth as compared with other predicted curves and experimental values.

In conclusion, the prediction of Lankford's coefficient is very sensitive. It requires domain size smaller than 10° for the interpolation method. It has also been checked that small texture evolutions can induce large evolution in Lankford's values (Duchêne *et al.* 2001). So, the tensile test should be simulated until a strain of 18% and the predicted Lankford's coefficients should result from the average of instantaneous Lankford's values associated with the computed texture associated to each strain level. These simulations are planned but not yet achieved.

Such investigation show that, while the trends are well predicted, the absolute values are still not reached. Different simplified assumptions can explain these differences, for instance:

-the use of Taylor's model that does not allow to take into account grain size and morphology and forgets grain equilibrium at the microscopic level;
-the results are based on initial yield locus shape, both material and geometric hardening (see definition in section 3.3) are neglected. At the present state, geometrical hardening could be introduced, however the simple isotropic Swift's hardening model is too poor to represent the reality with accuracy (see Chapter 3).

The measurement accuracy is far from perfect, so in short, it is not possible to use Lankford's coefficient as unique validation.

Remark: Another validation of the same type as the prediction of Lankford's coefficient could be the prediction of Forming Limit Diagrams (FLD). MSM team has already worked in this direction (Habraken *et al.* 1998). The Ph.D. theses by Duchêne and Wauters (to appear later on) will present some new results. However two remarks can already be done:

- If the goal is really to spare the experiments required to determine an FLD, then, **for classical steels,** the Cayssials' approach (Cayssials 1998) mixing mechanics, damage, metallurgy and statistic provides an interesting solution.
- If the goal is to validate a constitutive law using a Marciniak & Kuczynski 1967 type approach, then predictions are very sensitive. The results depend not only on the constitutive law under consideration but also on the localization criterion and on the initial defect used in the computations. Large modifications of FLD predictions can be obtained from very small variations of yield locus shape (see for instance Figure 2-20 and Figure 2-21 where Vegter modifies slightly the yield locus corner of biaxial stretching to achieve good FLD prediction). Hence, because of the many possible numerical adjustments, such kind of validation is of limited interest.

6.5.4. Academic rolling validation with texture updating

The rolling process is simply represented by one three-dimensional finite element in plane strain state as shown on Figure 6-51. The compressive force applied on direction z produces an expansion in the rolling direction x as the displacements in y direction are fixed.

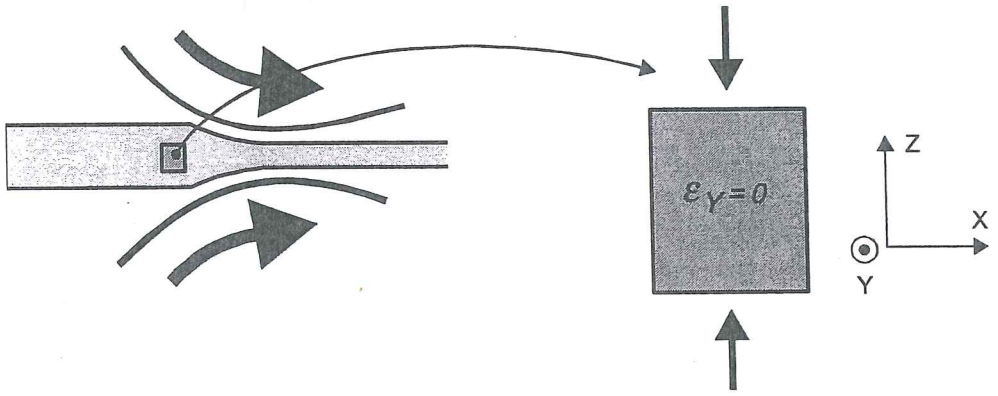

Figure 6-51 Rolling process represented by one finite element (from slides used for Duchêne *et al.* 1999c's presentation).

The initial texture, represented by a discrete set of 2000 crystal orientations, is isotropic. The finite element height is compressed until a reduction factor of two, which represents a 69% rolling reduction. Both cases of b.c.c and f.c.c materials are simulated with an arbitrary but identical hardening law. For each material, two simulations are performed, one with texture updating at each time step and one with the initial texture.

The final texture computed by the simulations with texture updating exhibits a typical rolling texture. For the b.c.c. material (Figure 6-52), the ODF maximum is 11.9 times the random texture level and is located at $\varphi_1 = 25°, \Phi = 50°, \varphi_2 = 55°$. For f.c.c. material (Figure 6-53), the ODF maximum is 14.7 at $\varphi_1 = 40°$, $\Phi = 70°$, $\varphi_2 = 20°$.

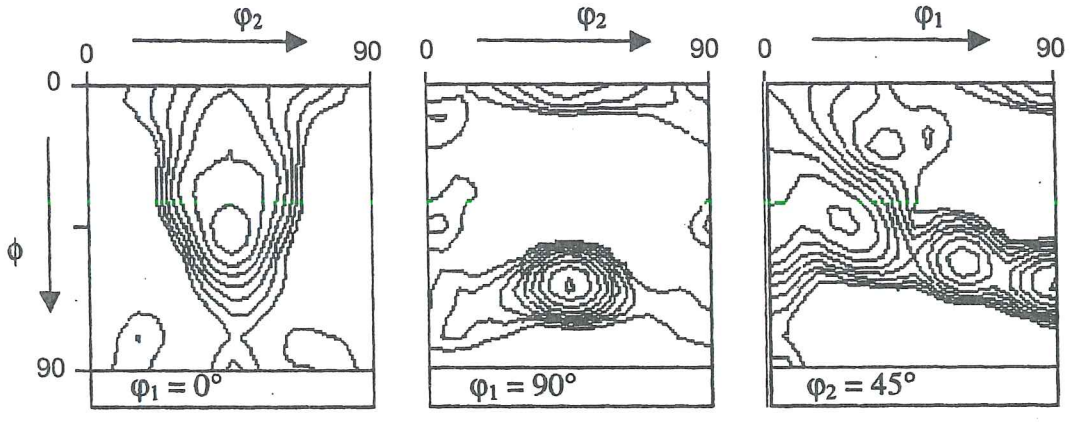

Figure 6-52 Sections $\varphi_1 = 0°$, 90° and $\varphi_2 = 45°$ in the final ODF of the b.c.c. material; curves levels = 0.7, 1.0, 1.4, 2.0, 2.8, 4.0, 5.6, 8.0, 11.0 and 16.0 (from Duchêne *et al.* 1999b).

In spite of an assumed common hardening behavior, a non-negligible influence of the crystal lattice is observed on the computed rolling forces (Figure 6-54). The larger stiffness observed for f.c.c. metals can be related to a lower number of slip systems to accommodate the imposed deformation. Even if the texture evolution is important, as shown on Figure 6-52 and Figure 6-53, no effect appears on the rolling force. As checked by Figure 6-55 which presents π-sections of the yield loci associated with random or rolling texture, it does not mean that these texture evolutions have no effect on the yield locus shape. It just happens that the point associated with the stress state in rolling is not affected by the shape evolution of the yield locus.

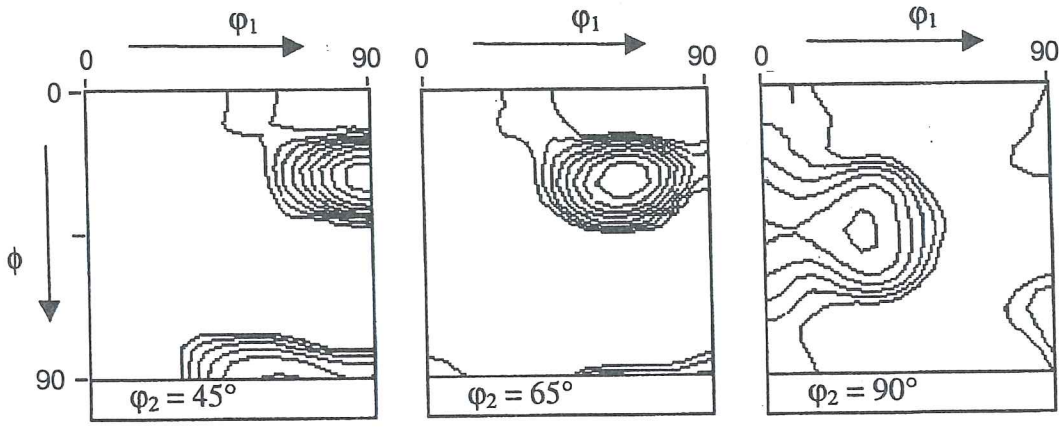

Figure 6-53 Sections $\varphi_2 = 45°$, 65°, and 90° in the final ODF of the f.c.c. material; curves levels = 0.7, 1.0, 1.4, 2.0, 2.8, 4.0, 5.6, 8.0, 11.0 and 16.0 (from Duchêne *et al.* 1999b).

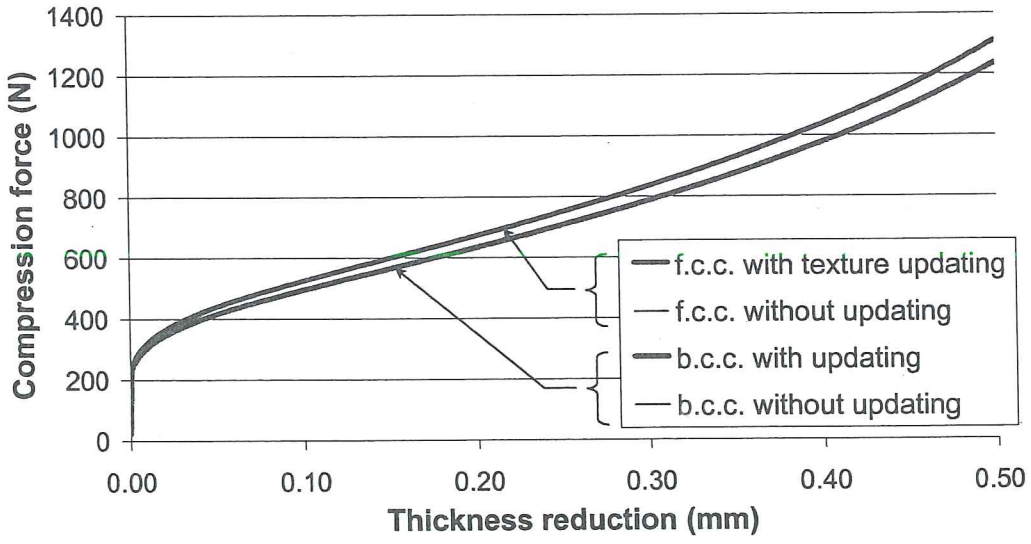

Figure 6-54 Rolling forces resulting of rolling simulations with or without texture updating for b.c.c. or f.c.c. materials (from Duchêne *et al.* 1999b.).

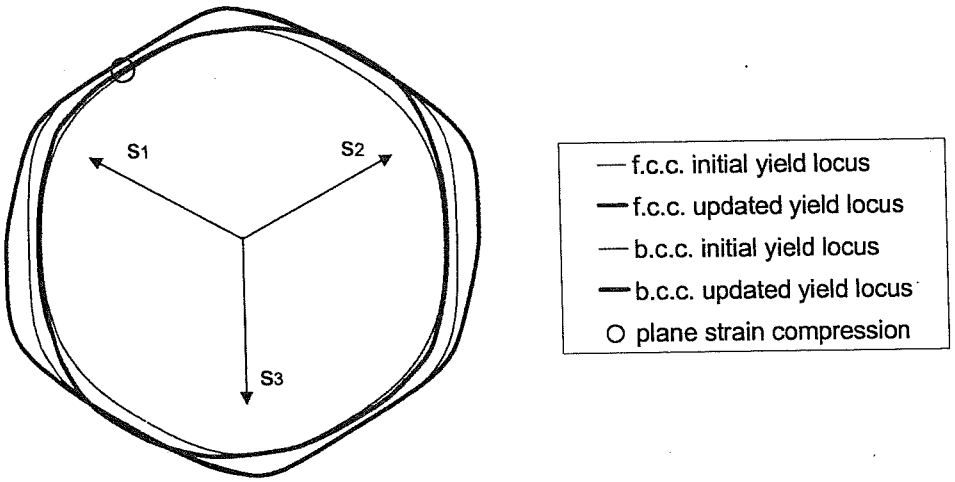

Figure 6-55 Initial and final π-sections of the yield locus computed from a random or a rolling texture for b.c.c. or f.c.c. materials (from Duchêne *et al.* 1999b).

The yield locus associated with a random texture in f.c.c. material is larger than the one corresponding to b.c.c. material. This explains the larger rolling force required to perform rolling from a mechanical point of view. The texture evolution creates, in both materials, a strongly anisotropic yield locus.

6.5.5. Conclusions of validation step

The interpolation model developed by MSM team stands between the models without yield locus (see Chapter 5), where a set of representative crystals is called upon to determine the macroscopic constitutive laws, and the models relying on a yield locus, computed thanks to texture information (see section 6.3). Its advantage is to keep an accurate description of plastic behavior by using a local description of the yield locus that allows the updating of its shape due to texture evolution. The CPU time reduction of such an approach has not yet been accurately estimated but does exist.

Applications to actual deep-drawing processes are in progress as well as the investigation of important parameters such as the size of the yield locus zone and the number of crystals necessary to represent the material behavior. Duchêne's thesis (to appear later on) will present comparisons between deep drawing experiments and simulations performed with classical Hill 1948 yield locus, the van Houtte's yield locus (6^{th} order series in stress space) and the interpolation method with or without texture updating. Initial and final texture measurements will allow checking the prediction of texture evolution.

Another thesis begins this year in MSM department to implement an improved kinematic hardening law coupled with the interpolation method. As numerical

developments are quite useless without experimental data, half of the thesis will be dedicated to the development of a tensile experiment coupled with shear deformation.

6.6. Conclusion

Clearly all the models described in this chapter are not straightforward for implementation into a FEM code. However their identification require less macroscopic mechanical experiments than accurate phenomenological models such as Karafillis's law, since the yield locus shape is deduced from texture measurements. In this case, experiments must "only" be used to define the hardening behavior. This chapter shows that constitutive laws with yield locus are available if one is interested in modelling sheet metal forming without forgetting all the microscopic events happening during deep drawing processes. The models presented here are more complex than those of Chapter 5. Their analytical formulation attempts to recover the micro-macro transfer performed by simple averaging of the behavior of sets of representative crystals in Chapter 5.

As long as texture updating during the sheet forming process can be neglected, it is clear that the models described in section 6.3 are interesting. They rely on accurate yield loci, which are computed once, outside the FEM code. This thesis proposes a summary of the methods used to estimate such yield loci according to texture description, crystal plasticity and the Taylor's assumptions.

This state of the art helps to understand the context of our proposals, which the originality of which lies in the concept of a local part of the yield locus instead of global one. This choice is motivated by our final goal of taking into account texture updating.

6.7. References

Aifantis, E.C., (1987) The physics of Plastic Deformations, *Int J Plasticity*, **3**, 211-247.

Arminjon, M. (1988) Lois de comportement homogénéisées pour la plasticité des polycristaux, Mém. d'habilitation, Univ. Paris-Nord, Villetaneuse.

Arminjon, M., Bacroix, B. (1991) On plastic potentials for anisotropic metals and their derivation from the texture function, *Acta Mechanica*, **88**, 219-243.

Arminjon, M., Bacroix, B., Imbault, D. and Raphanel, J.K. (1994) A fourth-order plastic potential for anisotropic metals and its analytical calculation from texture function, *Acta Mechanica*, **107**, 33-51.

Aukrust, T., Tjotta, S., Skauvik, I.,Vatne, H.E., Van Houtte, P. (1994) Modelling of texture development in aluminium extrusion, Proceedings of the 15th Riso Int. Symposium on Material Science, Anderson *et al.* editors, Denmark.

Aukrust, T., Tjotta, S., Vatne, H.E., Van Houtte, P. (1997) Coupled FEM and texture modelling of plane strain extrusion of an Aluminium alloy, *Int. J. of Plasticity*, **13, 1/2.**

Bergström, Y. (1969) A dislocation model for the stress strain behaviour of polycrystalline α-Fe with special emphasis on the variation of the densities of mobile and immobile dislocations, *Mat. Sci. Eng.*, **5**, 179-192.

Canova, G.R., Kocks, U.F., Tomé, C.N., (1985), The yield surface of textured polycrystals, *Mech. Phys. Solids,* vol. 33, **4**, 371-397.

Cayssials, F. (1998) A new method for predicting FLC, *IDDRG*, Conference Genval.

Cescotto, S. Grober, H. (1985) Calibration and application of an elastic-visco-plastic constitutive equation for steels in hot-rolling conditions, Eng. Comp. **2**, June, 101-106.

Charles, J-F, Habraken, A.M. (1996), Dépouillement des essais de traction necessaires à la calibration de la loi anisotrope élastoplastique avec endommagement de Y.Y. Zhu, rapport intermédiaire n° 9, Convention 2748, Micro-Macro, Université de Liège, Département MSM, Région Wallonne.

Charlier, R., Habraken, A.M. (1990), Numerical model of contact with friction phenomena by the finite element method, *Computers and Geotechnics*, **9**, 59-72.

Darrieulat, M., Piot, D. (1996), A method of generating analytical yield surfaces of crystalline materials, *Int. J. Plasticity,* **12/10**, 1221-1240.

Degueldre, A., Habraken, A.M., Munhoven, S., Aukrust, T., Van Bael, A., Karhausen, K. (1996) Texture prediction and aluminium extrusion.General Workshop COST 512, *MMSP 96 Davos : Modelling in Materials Science and Processing*, COST 512, Action Management Committee, Rappaz, M., Kadro M., editors, European Commission Directorate General XII Science Research Development, 260-265.

Duchêne, L., (1998a) Modifications et améliorations apportées à la loi MIPAY 3, rapport intermédiaire n° 26, Convention 2748, Micro-Macro, Université de Liège, Département MSM, Région Wallonne.

Duchêne, L., (1998b) Description de la programmation de la méthode d'interpolation de la relation de Taylor, rapport intermédiaire n° 30, Convention 2748, Micro-Macro, Université de Liège, Département MSM, Région Wallonne.

Duchêne, L., (1998c) Etude de la précision, de la convergence et de la stabilité de la méthode des hyperplans et de la méthode d'interpolation, rapport intermédiaire n° 31, Convention 2748, Micro-Macro, Université de Liège, Département MSM, Région Wallonne.

Duchêne, L., Habraken A.M., Cescotto S.,(1999a) Elastoplastic Anisotropic Model Based on Texture Analysis to Simulate Steel Sheet Behaviour. *7th Int. Symp. on Plasticity*, Cancun, Mexico, January 5-13, 1999, Akthar S. Khan Ed., Neat Press, 325-328.

Duchêne, L., Godinas, A., Habraken, A.M. (1999b) Texture effects on steel sheet behaviour under large strain simulations, *12th Int. Conf. on Textures of Materials (ICOTOM-12)*, Montreal, Canada, 9-13 August 1999, J.A. Szpunar, Ed. NRC Research Press Ottawa, pp. 286-291.

Duchêne L., Godinas A., Habraken, A.M.(1999c) Metal Plastic Behaviour linked to Texture Analysis and FEM Method, *NUMISHEET '99, 4th Int. Conf. and Workshop on Numerical Simulation of 3D Sheet Forming Processes*, Besançon, France, 13-17 September 1999, Edité par J.C. Gélin, P. Picart, Université de Franche-Comté et ENSMM, 97-102.

Duchêne, L. (2000), Implementation of a Yield Locus Interpolation Method in the Finite Element Code Lagamine, DEA Graduation Work, Université de Liège MSM Departement, Belgium.

Duchêne, L., Habraken, A.M., Godinas, A. (2000), Validation of a FEM model coupled with texture applied to deep drawing process. *ESAFORM*, Stuttgart, Fritz Editor, Inst. Für Kunststofftechnologie, IV-3, IV-6.

Duchêne, L., Habraken, A.M., Godinas, A. (2001), Influence of steel sheet anisotropy during deep-drawing processes, *Proceedings of the 4th ESAFORM Conference*, Habraken, A.M. Ed.

Dyduch, M., Cescotto, S., Habraken, A.M., (1995) Efficient error estimates for adaptive remeshing in 2D metal forming modelling, *Numiform'95, Simulation of Materials Processing: Theory, Methods and Applications,* Shen, S.-F., Dawson, P.,.editors,Belkema, Rotterdam,419-424.

Godinas, A., (1998) Définition locale de la surface de plasticité. Partie 1 : théorie, rapport intermédiaire n° 22, Convention 2748, Micro-Macro, Université de Liège, Département MSM, Région Wallonne.

Habraken, A.M. (1996) Description du module d'évolution de texture, rapport intermédiaire n° 4, Convention 2748, Micro-Macro, Université de Liège, Département MSM, Région Wallonne.

Habraken, A.M. Munhoven, S., (1996) Schéma d'implantation d'une version simplifiée du couplage micro-macro, texture éléments finis., rapport intermédiaire n° 10, Convention 2748, Micro-Macro, Université de Liège, Département MSM, Région Wallonne.

Habraken, A.M., Radu, J.P., (1997) Tests de la loi MIPAY, implantation des surfaces de plasticité série du 6ème ordre et du modèle de Taylor, rapport intermédiaire n° 21, Convention 2748, Micro-Macro, Université de Liège, Département MSM, Région Wallonne.

Habraken, A.M. (1998a) Taylor Ulg A : rapport de programmation, tests, rapport intermédiaire n° 19, Convention 2748, Micro-Macro, Université de Liège, Département MSM, Région Wallonne.

Habraken, A.M. (1998b) Taylor Ulg B : rapport de programmation, tests, rapport intermédiaire n° 20, Convention 2748, Micro-Macro, Université de Liège, Département MSM, Région Wallonne.

Habraken, A.M., Radu, J.P., Duchêne, L., Wauters, M., Munhoven, S. (1998) Comparison of Anisotropic Elastoplastic Laws Applied to Steel Sheet. *NUMIFORM 98, Simulation of Materials Processing : Theory, Methods and Applications*, Huetink, Baaijens Ed., Balkema, Enschede, The Netherlands, 769-774.

Hage Chehade, I. (1990) Simulation de l'emboutissage des tôles anisotropes par éléments finis avec prédiction des risques de striction, Thèse de doctorat, Institut National des Sciences Appliquées de Lyon.

Hill, R. (1948) A theory of the yielding and plastic flow of anisotropic materials. Proc. Royal Soc. London, **A193**, 281-297.

Hill, R. (1987) Constitutive dual potentials in classical plasticity, *J Mech. Phys. Solids*, **35**, 23-33.

Hiwatashi, S., Van Bael, A., Van Houtte, P., Teodosiu, C. (1997) Modelling of plastic anisotropy based on texture and dislocation structure, *Computational materials science*, **9**, 274-284.

Hoferlin, E., Van Bael A., Van Houtte P., (1999a) Comparison between stress-based and strain-rate based elasto-plastic finite element models for anisotropic metals, *Plasticity'99, Constitutive and damage modelling of inelastic deformation and phase transformation,* Khan, A.S. editor, Neat Press Fulton, Maryland.

Hoferlin, E., Van Bael A., Van Houtte P., Teodosiu C. (1999b) An accurate model of texture and strain-path induced anisotropy, *Numisheet'99, Numerical Simulation of 3D Sheet Forming Processes,* Gelin, J.C., Picart, P., editors, Université de Franche Comté, Besançon, France.

Hoferlin, E. (2001) Incorporation of an accurate model of texture and strain-path induced anisotropy in simulations of sheet metal forming, Ph. D thesis Katholieke Universiteit Leuven.

Imbault, D., Arminjon, M. (1993) Theoretical and numerical study of the initial and induced plastic anisotropy of steel sheets, using a texture-based methodology, Final report of contract Univ. J. Fourier n° 17191401, Laboratoire 3S, Université Joseph Fourier, France.

Karafillis, A.P., Boyce, M.C. (1993) A general anisotropic yield criterion using bounds and a transformation weighting tensor, *J. Mech. Phys. Solids*, **41/12**, 1859-1886.

Khan, A.S., Cheng, P. (1996) An anisotropic elastic-plastic constitutive model for single and polycrystalline metals. I – theoretical developments, *Int. J. Plasticity*, **12/2**, 147-162.

Lequeu, Ph., Gilormini, P., Montheillet, F., Bacroix, B., Jonas, J.J. (1987a) Yield surfaces for textured polycrystals, I. Crystallographic Approach, *Acta Metall.*, **35/2**, 439-451.

Lequeu, Ph., Gilormini, P., Montheillet, F., Bacroix, B., Jonas, J.J. (1987b) Yield surfaces for textured polycrystals, II. Analytical Approach, *Acta Metall.*, **35/5**, 1159-1174.

Li, K. (1996) Contribution to the finite element simulation of three-dimensional sheet metal forming, Ph. D. thesis, Université de Liège, département MSM.

Marciniak, Z., Kuczynski, K., (1967) Limit strains in the processes of stretch-forming sheet metal. *Int. J. Mech. Sci.*, **9**, 609-620.

Mecking, H., Lücke, K. (1970) A new aspect of the theory of flow stress of metals, *Scripta Metallurgica*, **4**, 427-432.

Miller, M.P., Mc Dowell, D.L. (1996) Modeling large strain multiaxial effects in FCC polycrystals, *Int. J. of Plasticity*, **12/7**, 875-902.

Monfort, G., Adriaens, J. P., Defourny, J., Jodogne, P., Brunet, M., Detraux, J.M. (1991), FEM simulation of non-axisymmetric press formed parts using anisotropic constitutive laws for steel, *IDDRG,* Pisa.

Monfort, G., Defourny, J., (1993) A new orthotropic plasticity model for complex sheet forming, *Centre for Theoretical Physics – External activities. (ICTP-OEA),* Conference on interface between physics and mathematics. Hangzhou, China.

Monfort, G., Defourny, J., (1994) The *3G* plasticity model, Metallurgical bases – Mechanical evaluation - Application to finite element simulation of steel forming, 14 septembre, Centre de recherches métallurgiques, Liège.

Montheillet, F., Gilormini, P., Jonas, J.J.(1985) Relation between axial stresses and texture development during torsion testing : a simplified theory. *Acta Metall.*, **33/4**, 705-717.

Munhoven, S., Habraken, A.M., Winters, J., Schouwenaars, R., Van Houtte, P. (1995a) Application of an anisotropic yield locus based on texture to a deep drawing simulation, *NUMIFORM 95, Simulation of Materials Processing: Theory, Methods and Applications*, Shen&Dawson editors, Balkema, 767-772.

Munhoven, S., Winters J. Habraken, A.M., (1995b) Finitie element applications of an anisotropic yield locus based on crystallographic texture, *Computer simulations in materials science Nano / Meso / Macroscopic Space and teine scales.* Nato Advenced study Institute, Ile d'Oléron France 6-16 juin, Université de Liège, Département MSM.

Munhoven, S., (1996), Deformation history from 2D Lagrangian FEM results, Internal report n°226, MSM department, University of Liège.

Munhoven, S., Habraken, A.M., Van Bael A., Winters J. (1996) Anisotropic finite element analysis based on texture. *Proc. 3rd Int. Conf.: Numerical Simulation of 3-D Sheet Metal Forming Processes. NUMISHEET'96*, Ed. L.K. Lee, G.L. Kinzel, R.H. Wagoner, The Ohio State University, Columbus, 112-119.

Munhoven, S., Habraken, A.M. (1996) Anisotropic finite element analysis based on texture, rapport intermédiaire n° 3, Convention 2748,Micro-Macro, Université de Liège, Département MSM, Région Wallonne.

Munhoven, S. (1997) Taylor ULg A, rapport intermédiaire n° 4, Convention 2748 Micro-Macro, Région Wallonne, Université de Liège, Département MSM.

Munhoven, S., Habraken, A.M., Radu, J.P.(1997), Anisotropic plasticity based on crystallographic texture, 4ème Congrès de Mécanique théorique et appliquée, Leuven.

Ning, J., Aifantis, E.C. (1996) Anisotropic yield and plastic flow of polycrystalline solids, *Int. J. of Plasticity*, **12/10**, 1221-1240.

Ponthot, J.Ph., (1995) Traitement unifié de la mécanique des milieux continus solides en grandes déformations par la méthode des éléments finis, Ph.D. thesis, LTAS, Université de Liège.

Pospiech, J., (1982) Symmetry Analysis in the Space of Euler Angles, *Quantitative Texture Analysis*, Bunge, H.J., Esling, C. editors, Deutsche Gesellschaft fur Metalkunde.

Radu, J.P., Munhoven, S., Habraken, A.M., (1997) Amélioration de la version simplifiée du couplage micro-macro : texture-éléments finis, rapport intermédiaire n° 11, Convention 2748,Micro-Macro, Université de Liège, Département MSM, Région Wallonne.

Schoenfeld, S.E., Asaro, R.J., (1996) Through thickness texture gradients in rolled polycrystalline alloys, *Pergamon, Int. J. Mech. Sci.*, vol 38, **6**, 661-683.

Simo, J.C., Ortiz, M. (1985) A unified approach to finite deformation elastoplastic analysis based on the use of hyperelastic constitutive equations, *Comp. Meth. Appl. Mech. Eng.*, **49**, 221-245.

Teodosiu, C., Hu, Z. (1998) Microstructure in the continuum modelling of plastic anisotropy, *Proceedings of the 19th Riso Int. Symp. on Materials Science : Modelling of Structure and Mechanics of Materials from Microscale to Products*, Carstensen, J.V., Leffers, T. Eds.

Tóth, L.S., Van Houtte, P. (1992) Discretization techniques for orientation distribution functions, *Textures and Microstructures*, 1992, **19**, 229-244.

van Bael, A. (1994) Anisotropic yield loci derived from crystallographic data and their application in finite element simulations of plastic forming processes, proefschrift voorgedragen tot het behalen van het doctoraat in de toegepaste wetenschappen, Katholieke Universiteit Leuven.

van Bael, A., Winters, J., Van Houtte, P. (1996) A semi-analytical approach for incorporating crystallographic data into elasto-plastic finite element formulations, *Textures of Materials,* Proceedings of the 11th Int. Conf. on Textures of Materials, vol. 1, ICOTOM-11, Sept. 16-20, Liang Z., Zuo L., Chu Y. Eds.

van Houtte, P. (1988) A comprehensive mathematical formulation of an extended Taylor-Bishop-Hill model featuring relaxed constraints, the Renouard-Wintenberger theory and a strain rate sensitivity model, *Textures and Microstructures*, **8-9**, 313-350.

van Houtte, P. (1992) Anisotropic Plasticity, *Numerical Modelling of Material Deformation Processes, Research, Development and Applicaitons,* Hartley, P., Pillinger, I., editors, Springer-Verglag.

van Houtte, P. (1994) Application of plastic potentials to strain rate sensitive and insensitive anisotropic materials, *Int. J. Plasticity*, **10**, 719-748.

van Houtte, P. (1995) Micromechanics of polycrystalline materials, Chaire Francqui, Université de Liège.

van Houtte, P., van Bael, A. (1997) Texture measurements, Report EX/97/009/1

Wang, N., Hall, F.R., Pillinger, I., Hartley, P., Sturgess, C.E.N. (1992) Finite-element prediction of texture evolution in material forming, *Numerical Methods in Industrial Forming Processes*, Chenot, Wood&Zienkiewicz Eds, 193.

Wauters, M. (2000), Calibration of an anisotropic elasto-plastic damage model for sheet metal forming, Master thesis, MSM department, University of Liège.

Winters, J. (1996) Implementation of a texture-based yield locus into an elastoplastic finite element code. Application to sheet forming. Ph.D. thesis, Katholieke Universiteit Leuven, MTM department.

Zhu, Y.Y., Cescotto, S. (1996) Unified and mixed formulation of the 8-node hexahedral elements by assumed strain method, *Comput. Methods Appl. Mech. Engrg.*, **129**,177-209.

References

Beaudoin, A.J., Dawson, P.R., Mathur, K.K., Kocks, U.F.(1995), A hybrid finite element formulation for polycrystal plasticity with consideration of macrostructural and microstructural link, Int J. of Plasticity, **11/5**, 501-521.

Garikipati, K., Hughes, J.R.T. (to appear) Embedding a Micromechanical Law in the Continuum Formulation-A Multiscale Approach Applied to Discontinuous Solution, *Int. J. for Computational Civil and Structural Engineering.*

7. CONCLUSIONS

This overview work provides an idea of the main models implemented today in FEM codes to represent macroscopic plastic anisotropic material behavior. Both plastic yield locus and hardening laws are important features for capturing the actual metal response at various loading.

Some examples, such as the microscopic finite element simulations from Teodosiu (section 5.2.1) or Acharya & Beaudoin (section 5.2.2) also show the interest of FEM simulations to check the validity of the microscopic models in representing macroscopic behavior.

Some care has been brought to provide not only the theoretical models, but their identification methods as well. Whenever possible, links between models are presented, such as, for instance, Aifantis's proposal that gives physical basis to von Mises and Karafillis' laws.

In the future, hardware development and parallel computation will reduce problems of CPU time. However, each time that this happens, engineers increase the sizes of the problems that they want to solve by finite elements... So, simple phenomenological laws described in chapter 2 or yield loci presented in chapter 6 that allow escaping to microscopic computations in the macroscopic FEM simulations, retain their interest. This also forces researchers to identify the important features necessary to capture material behavior. For instance, it is clear that texture evolution effects on yield locus are not necessary in all deep-drawing simulations.

The actual question is: what is really useful to take into account? The answer is not the same according to the goal of the simulations: shape prediction after spring back, texture prediction, residual stress field, wrinkling and necking prediction. It is clear that criteria exist to predict necking and wrinkling, but they rely on accurate stress and strain field computations. The spring back prediction is quite hard if your model neglects elasticity. The final shape and size of the yield locus after forming processes is important if your goal is to apply accurate fatigue models to predict the life of the pieces. The model descriptions provided in this thesis should help to choose the adapted model to fit one's requirements.

One direction not investigated in this overview is the formulation of the Finite Element itself. Going from a simple displacement formulation to a mixed or hybrid formulation can already provide a better convergence and a smoother stress answer, even if a low number of crystals is used per integration point (Beaudoin *et al.* 1995). Another possibility is to apply a simple macroscopic analysis coupled with a micro-macro analysis only where some event, such as strain localization, appears and requires a finer scale. For instance, Garikipati & Hughes (to appear) propose such a so-called variational multiscale approach.